OPTICAL PROPAGATION METHODS FOR SYSTEM-LEVEL MODELING OF OPTICAL MEM SYSTEMS

by

Timothy P. Kurzweg

B.S. in E. E., The Pennsylvania State University, 1994

M.S. in E. E., University of Pittsburgh, 1997

Submitted to the Graduate Faculty

of the School of Engineering

in partial fulfillment of

the requirements for the degree of

Doctor of Philosophy

in

Electrical Engineering

University of Pittsburgh

2002

UNIVERSITY OF PITTSBURGH

SCHOOL OF ENGINEERING

DEPARTMENT OF ELECTRICAL ENGINEERING

This dissertation was presented

by

Timothy P. Kurzweg

It was defended on

August 1, 2002

and approved by

Dr. J. Thomas Cain, Professor, Department of Electrical Engineering

Dr. Ronald G. Hoelzeman, Associate Professor, Department of Electrical Engineering

Dr. Hong Koo Kim, Professor, Department of Electrical Engineering

Dr. Donald M. Chiarulli, Professor, Department of Computer Science

Dissertation Director: Dr. Steven P. Levitan, Professor, Department of Electrical Engineering

OPTICAL PROPAGATION METHODS FOR SYSTEM-LEVEL MODELING OF OPTICAL MEM SYSTEMS

Timothy P. Kurzweg, Ph.D.

University of Pittsburgh, 2002

ABSTRACT

In this thesis, we determine and implement an optical propagation technique suitable for system-level simulation of optical micro-systems. The Rayleigh-Sommerfeld formulation is selected as the optical propagation modeling technique because it satisfies the requirements of a system-level CAD tool and supports accurate modeling at propagation distances on the order of the wavelength of light. We present an efficient solution to the Rayleigh-Sommerfeld formulation using the angular spectrum technique which uses the fast Fourier transform to decompose the complex optical wavefront into plane waves propagating from the aperture to the observation plane. This technique reduces the computational order of solving the Rayleigh-Sommerfeld formulation from a brute force direct integration technique of $O(N^4)$ to a computational order of $O(N^2 \log N)$.

For use in a design environment, we present an error analysis of our technique. Errors are caused by the discrete sampling of the optical wavefront over a finite range to approximate the infinite continuous Fourier transform. Methods for reducing both aliasing and truncation errors are presented, along with techniques to estimate the remaining errors of the angular spectrum technique.

We perform a rigorous error estimate on several common optical wavefronts and provide techniques to perform an error analysis on a general wavefront. The utility of this method is shown by implementing the work into a mixed-signal, multi-domain CAD tool, in which we perform system-level simulations and analyses of several optical MEM systems.

DESCRIPTORS

Optical Propagation Modeling

Efficient Optical Propagation

Optical CAD

System-Level Simulation

Angular Spectrum

Optical Micro-Systems

FOREWORD

I would first like to thank Dr. Steven Levitan for his guidance and support throughout this research. Steve has not only taught me so much about the commitment to research and science, but has also taught me about the ways of success in an academic environment. I value our professional relationship as well as his friendship.

I would also like to thank Dr. Don Chiarulli, as an advisor and a friend. His comments and suggestions have helped me greatly along the way. I am already looking forward to our next golf game. I would also like to thank the rest of my committee, Dr. Tom Cain, Dr. Ron Hoelzeman, and Dr. Kim. I have known these professors throughout my time at the University of Pittsburgh and am honored that they were part of my defense.

I am very fortunate to have such a wonderful family, and owe a lot of my success to them. My parents and brothers (and sister-in-law and nephew) have given me unwavering love and support throughout my entire graduate school career. You can predict the success of a man by looking at the family that he came from. I am very fortunate.

I would also like to thank my friends and supporters that had confidence in me. Their extra encouragement made the tough times better. I look forward to our next night out on Doc's deck to discuss life, love, and the pursuit of happiness (and of course the Steelers!). And special thanks to my colleagues and friends here at the University of Pittsburgh. Jose, Majd, Yee-Wing, Sandy, and the others who have come and gone, thank you for all of the help, discussions, encouragement, and support.

Lastly, I would like to thank Jennifer for her love and support especially through this final summer of dissertation writing. You kept me together mentally and emotionally. Your presence in my life has made everyday happier and more fulfilling. I look forward to celebrating all our accomplishments together.

Thank you all.

This dissertation is dedicated in loving memory of my Opa, Dr. Hermann H. Kurzweg. Being the 3rd generation Ph.D. in my family, I must recognize the first.

TABLE OF CONTENTS

Page

LIST OF TABLES

LIST OF FIGURES

1.0 INTRODUCTION

1.1 Optical Modeling for Optical Micro-Systems

As micro-optical system applications transition from abstract ideas to marketable products, the commercialization process is slowed by the cost of designing, prototyping, and testing these systems. Instead of physically prototyping these optical micro-systems, computer aided design (CAD) tools can greatly reduce the cost and time-to-market of an optical micro-system product, as evident in the VLSI CAD revolution of the past 30 years. Using CAD tools, integrated circuits are designed, fabricated, and the time-to-market is decreased significantly, with the increase of successful first physical prototypes.

However, as with many new technologies, design methods and tools for optical micro-systems are ad-hoc. Currently, multi-domain micro-systems are simulated with point-tools using component level models performed at the physical level. These tools are typically domain specific (optical, electrical, or mechanical) and computationally complex. As a result, simulation of the entire system is computationally intensive, uses mixed tools and frameworks, and does not support interactions between the different domains.

In contrast, system-level tools are designed to include multiple domains and allow efficient system simulation, by modeling components with their functionality rather than their physical construction. Established MEM (micro-electrical-mechanical) system-level modeling tools exist, in which physical device models are extracted to the system-level [(1)(2)]. However, optical models are not easily integrated into these tools.

When light interacts with the small feature sizes of micro-systems, many of the common optical propagation modeling techniques are invalid, and full vector or scalar solutions to Maxwell's equations are required [3]. However, these optical modeling techniques are computationally and memory intensive, therefore, interactive design between system designer and CAD tool is almost impossible. As the number of optical components increases in micro-system design, the demand for computationally efficient simulation tools rises. Therefore, the optical modeling technique that supports system-level simulation of MOEM (micro-electro-opto-mechanical) systems must be a rigorous model, accurately modelling optical propagation through micro-systems, yet, the technique must also be computationally efficient, supporting interactive design between the designer and the simulation tool.

In this thesis, we describe an optical propagation technique that is suitable for implementation into system-level, multi-domain micro-system CAD tools. The technique is determined by examining typical optical micro-systems, along with the goals and requirements of the CAD simulation tool. One of the main contributions of this thesis is a detailed error analysis of using this efficient technique. This work has been integrated with our free-space, mixed-signal, system-level CAD tool Chatoyant, extending its ability to accurately model micro-optical systems.

In this introductory chapter, we present motivation for our work and define the goals of a mixed-signal, multi-domain CAD tool. We define system-level simulation and present a problem statement listing the contributions in the dissertation. We conclude this chapter with a outline for the remainder of this dissertation.

1.2 Motivation

The thesis is motivated by the advancement of mixed-signal, multi-domain optical microsystems and the need for a system-level modeling approach for these systems. In this section, we use two specific micro-optical systems to motivate the necessity for an accurate system-level micro-optical modeling tool: we examine an optical MEM switch and a display application using a Grating Light Valve MEMS component. We follow by stating our definition of system-level analysis and the advantages of using this simulation methodology for optical micro-systems.

1.2.1 Optical MEM Switches

High-speed optical switching systems based on free-space optical MEM systems are a critical backbone technology for next generation computer networks and systems [4]. These devices are capable of switching multiple optical channels using fiber ribbon cable as the input and output medium, and free space optics in the switching component. OMEM devices are used to implement the switch function, using techniques such as physically deflecting each beam based on the electrostatic displacement of a microscopic mirror. Systems built with these switches have numerous advantages over typical waveguide or fiber switching systems, including the reduction of coupling loss and crosstalk, and independence from wavelength, polarization, and data format [5]. The switches have been reported as 10 times smaller and faster than typical fiber-based switches, while requiring only $1/100^{th}$ of the operating power [6]. Systems built with these switches also have shown potential of increased system reliability and reduced system costs.

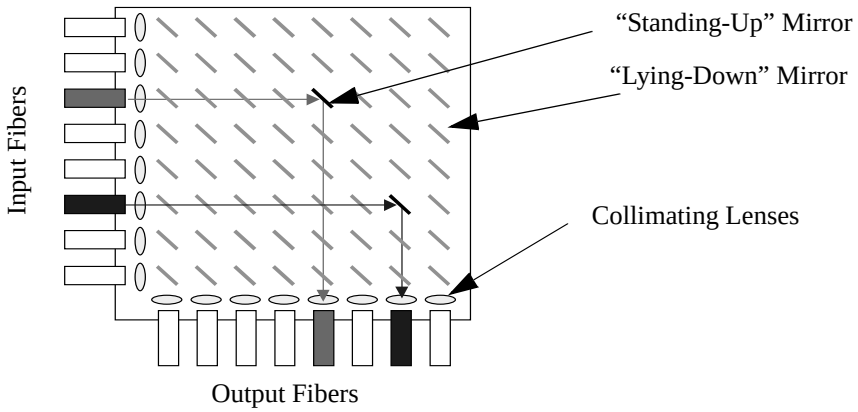

Figure 1 Free-Space Micromachined Optical Switch

We examine typical optical MEM switching systems, such as Lin et al.'s (AT&T) micromachined switch presented in reference [4]. A drawing of their proposed 8x8 optical cross-connect is seen in Figure 1. In this figure, eight input fibers are placed onto the switching chip from the left side. This system implements a true crossbar switch, where each input can be routed to any of the output fibers, lined across the bottom of the chip. In order to establish every connection available, there are 64 hinged mirrors lying on the surface of the chip. Fiber switching is achieved by the specified interconnect mirror "self assembling" off of the substrate surface, using conventional scratch drive actuators (SDA)[7] MEM components, into a standing position with a 45 degree angle relative to the incoming light. In Figure 1, two example interconnects are achieved, with the black mirrors representing assembled standing mirrors and the grey mirrors representing mirrors that remain lying down on the substrate. The mirrors in this switch have dimensions of 150x140 μm. This system has a switching speed of less than 700 μsec with negligible crosstalk and is polarization independent.

The challenges of modeling a system like the one described are numerous. The most obvious challenge is that we are modeling three distinct domains: the electrical, the optical, and the

mechanical. Each domain needs to be accurately modeled. Additionally, the simulation framework must also support the modeling of the interactions between the domains. For example, in the optical MEM switch presented here, electronic drivers actuate the mechanical mirrors, which assemble and deflect the optical beam, completing the switching operation. Another modeling challenge is that the design of the switch calls for the support of optical data to be modeled. Therefore, system-level performance measures such as bit error rate, insertion loss, and crosstalk are important to the system designer and must be modeled.

1.2.2 Grating Light Valve

To provide further motivation for our work, we next examine one of the more promising MOEM components, the Grating Light Valve (GLV) [8]. This device has many display applications, including digital projection, HDTV, and vehicle displays. The GLV is simply a MEM phase grating made from parallel rows of reflective ribbons. When all the ribbons are in the same plane, incident light that strikes normal to the surface reflects 180 degrees from the GLV. However, if alternating ribbons are moved down a distance equal to a quarter of a wavelength of the incident light, a “square-well” diffraction pattern is created, and the light is reflected at an angle from that of the incident light. The angle of reflection depends on the width of the ribbons and the wavelength of the incident light. Figure 2 shows the ribbons, from both a top and side view, and also the reflection patterns for both positions of the ribbons.

The GLV component is fabricated using standard silicon VLSI technology, with ribbon dimensions approximately 3-5μm wide and 20-100 μm long [8]. Each ribbon moves through electro-static attraction between the ribbon and an electrode fabricated underneath the ribbon. This

electro-static attraction moves the ribbons only a few hundred nanometers, resulting in an approximate switching time of 20 nsec.

Again, there are challenges in modeling and simulating a system using the GLV. Besides the multi-domain modeling challenges seen in the optical MEM switch, the GLV depends on a diffractive phenomenon to direct the light beam. Therefore, a rigorous modeling technique is required for both the modeling of the GLV device and the optical propagation technique as light diffracts off the surface of the ribbons.

Both of the above motivating examples, the optical MEM switch and the GLV based systems, have been simulated with our system-level simulation tool. These examples and their simulation results and analyses will be presented later, in Chapter 5 of the thesis.

1.2.3 System-Level Simulation

Typical modeling techniques for optical micro-systems can be seen in Figure 3. Most tools that model micro-optical systems are based on device level physical models. This is seen as the lowest level in the figure. These component models are typically solved using full 3D vector solutions of Maxwell's equations. This leads to a "bottom-up" design flow, where the components are very accurately modeled, however the computation complexity of these algorithms

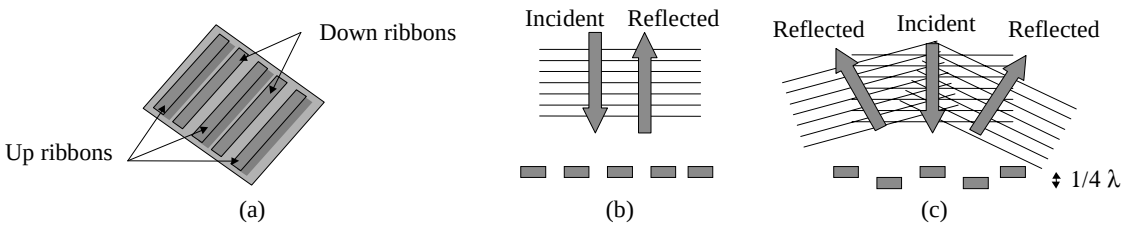

Figure 2 GLV Device (a) Top View and Side View Operation for (b) Up Ribbons and (c) Down Ribbons

make system simulation prohibitive.

The second level of modeling abstraction is behavioral modeling, where component details are extracted from the physical model to the behavioral model. These models are commonly solved using reduced ordered models, typically ordinary differential equations. Common circuit simulators such as SPICE and Saber use this level of modeling, along with AHDL [9] simulators, such as VHDL-AMS. The simulation time is greatly reduced from the physical models, however, as the number of components increase or additional domains (that is, optical or mechanical) are added to the system, this technique can become computationally inefficient and cannot support the desired system-level performance measures.

The highest abstract modeling level is the system level, highlighed in Figure 3. This is the modeling technique that is performed throughout this thesis. The system level is composed of an ensemble of component behavioral models, and uses fast solvers at the component/behavioral level. Using this modeling technique, we support domain specific signal propagation models, along with modeling the interactions between the optical, electrical, and mechanical domains.

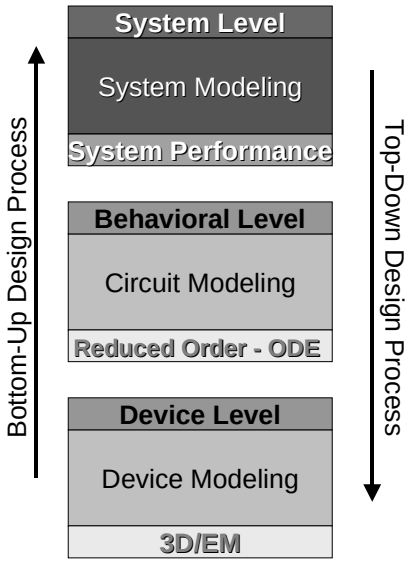

Figure 3 Modeling Levels for Optical Micro-System Simulation

Using this top-down modeling technique, ensemble performance measures, such as bit-error-rate (BER), optical and electrical crosstalk, insertion loss, and packaging/alignment tolerances are simulated and reported to the system designer.

1.3 Problem Statement

As seen in the previous examples, there are many challenges to enabling system-level simulation and analysis for micro-optical systems. In this section, we describe the problems which are addressed in this thesis:

- *Determine an optical propagation technique that is valid for the system-level simulation of optical micro-systems.* Many of the typical optical propagation simulation techniques used for modeling macro-systems are not valid for micro-system simulation.

- *Determine a computationally efficient algorithm for the optical propagation method.* This is motivated by our desire to model and simulate complete systems in an interactive design environment.

- *Determine the error in implementing the efficient optical propagation technique in a system-level CAD tool and show how it can be reduced.* A major contribution of this thesis is in determining the error of using an optical propagation model, and how this error can be reduced.

- *Implement this work in a system-level CAD tool.* We show how the optical propagation modeling technique interfaces into a mixed-signal, multi-domain CAD tool, and perform system-level simulations on selected optical MEM systems.

In this thesis, we dedicate a separate chapter to each of these stated problems and challenges.

1.4 Organization of Thesis

In Chapter 2, the thesis presents the requirements for determining an appropriate optical propagation technique that is valid for micro-optical system modeling and simulation. In this section, we present typical optical MEM components and systems, and determine the physical sizes, geometries, and optical nature (refractive, diffractive, scattering, etc.) of the optical components. We introduce the requirements of supporting system-level CAD and take these into consideration when determining an optical propagation model appropriate for simulating optical micro-systems. This chapter continues with a presentation of various levels of optical propagation techniques, from simple ray tracing to full vector solutions. Advantages and disadvantages of each of the techniques are presented, along with a comparison of their computational resources, until a conclusion is drawn determining the most appropriate system-level optical modeling technique for optical micro-systems.

In Chapter 3, we present an efficient optical propagation technique suitable for system-level simulations of micro-optical systems. The method is based on the angular spectrum technique, which simplifies a propagating complex optical wavefront by propagating plane waves, each with a different weight and direction. These plane waves are determined by the Fourier transform of the complex optical wavefront and are based on their associated spatial frequencies. The angular spectrum is an exact solution to the scalar Rayleigh-Sommerfeld formulation.

In Chapter 4, detailed error analysis of using the angular spectrum technique is presented. This section begins with a explanation of using the discrete Fourier transform to perform the forward and inverse Fourier transform. The analysis continues by relating the spatial and frequency domains, and determining the error when computing the complex optical values in these domains.

Besides a specific error analysis of some common optical wavefronts, a general error estimation technique is provided.

In Chapter 5, the implementation of the optical propagation techniques into our mixed-signal, multi-domain framework, *Chatoyant*, is presented. Our modeling methodology is discussed, along with a brief introduction to the modeling of the electrical and mechanical domains. We provide system-level simulations of an optical MEM switch and a display projection systems based on the grating light valve technology.

Chapter 6 presents a summary and draws conclusions of the work presented in this dissertation. In this section, we also present research areas in which this work can be expanded.

2.0 OPTICAL REQUIREMENTS AND MODELS

In this chapter, we examine the requirements for the development of an optical propagation modeling technique for a system-level CAD tool for the simulation of optical micro-systems. In the first section, we define the goals and requirements of a mixed-signal CAD tool through a presentation of a few common optical MEM systems. We next examine the classical optical propagation methods and state the advantages and disadvantages of using these techniques. This chapter is concluded with the determination of the optical propagation technique most suitable for system-level simulation of optical micro-systems.

2.1 Optical Propagation Requirements

The requirements of a free-space optical propagation technique for optical micro-systems are defined by the goals of the CAD tool, the physical sizes of the components, the propagation distances between optical components, and the surface properties of the components from which the light reflects, refracts, and/or diffracts. We introduce these requirements in the following section.

2.1.1 System-level CAD Requirements

As stated previously, our goal is to create a system-level CAD tool for the interactive design of optical MEM systems. Therefore, we are not only striving for accuracy, but we also require computationally efficient device and propagation algorithms, enabling fast system-level simulations. Additionally, a system-level tool needs to evaluate such system performance measures as

BER (bit error rate), tolerancing, insertion loss, and crosstalk. From these requirements, the model for light propagation must support optical power information, such as intensity, phase, and frequency (wavelength) dependence. To further identify the appropriate optical modeling technique, we examine typical optical MEM systems and evaluate the available optical propagation techniques which satisfy the requirements imposed by these systems.

2.1.2 Optical Micro-Systems Requirements

We now examine typical optical micro-systems to determine the optical propagation requirements that are established from typical components that comprise these systems. We first examine the optical MEM switch, described earlier in Figure 1. By using this system as a representative OMEM switch, we can determine the type of optical modeling that is required for modeling mixed-signal micro-systems.

The collimating lenses seen in Figure 1 could be either refractive or diffractive elements, establishing the first requirement of the optical propagation method: the support of optical diffraction. In these optical MEM switches, the lenses are typically diffractive micro-Fresnel lenses due to their ease of fabrication using standard CMOS facilities. However, Fresnel lenses are inefficient (theoretical 10% efficiency [5]) and greatly increase the optical insertion loss. Therefore, in some systems, refractive lenses or fiber collimators are being considered [4].

The sizes of the components and the propagation distances between the components also constrain the optical propagation model to support diffraction. For example, the mirrors in this switch have dimensions of 150x140 μm. Sizes of other optical MEM components are smaller, as

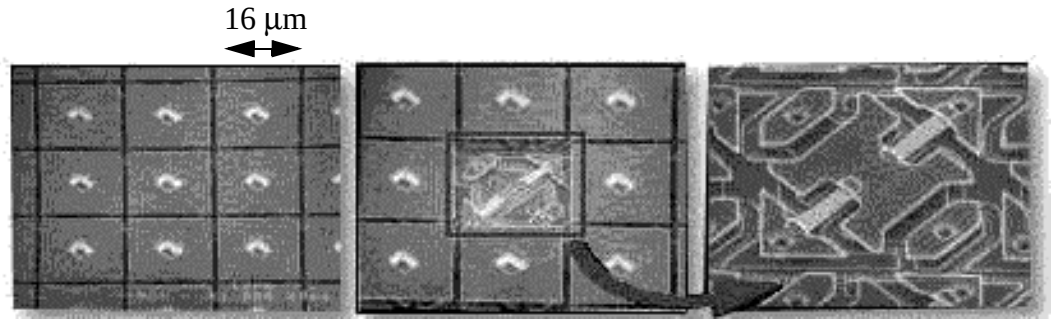

Figure 4 Texas Instruments's Digital Micro-mirror Device (DMD) [10]

in Texas Instruments's digital micro-mirror device (DMD), seen in Figure 4, where over 1,000,000 projection mirrors on the chip surface each have a square side length of only 16 μm [10]. When these and other micro-mirrors are fabricated, the mirrors can be inherently curved, with a small amount of surface roughness, adding to our list of requirements for the optical propagation technique.

Since optical MEMS are fabricated with the same techniques as electronic VLSI design, the size of an OMEMS chip does not usually exceed a couple of millimeters, therefore, typical distances between components (i.e., propagation distances) are approximately 10-1000 μm. For example, the pitch between the switching mirrors in Figure 1 is 500 μm. With the sizes and distances on the order of only ten to a thousand times the wavelength of light, optical diffractive models are required even for applications composed of purely refractive components.

An additional requirement, illustrated by examining the optical MEM switch, is that the optical models must easily interface with fiber-based CAD tools. This is seen by the light being brought "on-" and "off-" chip through fibers or waveguides. We interface our free-space optical propagation technique with existing fiber propagation software packages, such as RSoft's BeamPROP [11] and Optiwave's BPMCAD [12]. These tools model light through the beam propagation method (BPM) and/or finite difference (FD) modeling for optical propagation.

We summarize the requirements of the optical propagation technique in the following table.

Table 1 Summary of Requirements of Optical Propagation Technique

CAD Tool Requirements	Support for Optical Components	Support for Propagation Distance	Support for Surface Types
Accurate	Refractive	Near-Near Field	Free-Space
Efficient Computation	Diffractive	Near Field	Fiber
System-Level Performance Measurements		Far Field	Surface Roughness and Curvature

After determining the requirements of the optical propagation model, we next examine the classical modeling techniques and approximations to determine which is appropriate for optical MEM simulation.

2.2 Optical Propagation Models

This section discusses many of the typical optical propagation techniques. As will be seen, the common techniques for modeling optics for macro scale applications often cannot be used in the micro-scale case. In Figure 5, we present an illustration of different optical propagation techniques that we will present in this thesis [13]. The complexity of the techniques range from the bottom inner-circle to the top outer-circle in which the techniques solve the complete vectorial Maxwell equations. We have determined for system-level results it is important to have accurate results, yet still be computationally efficient. In this section, we evaluate the common techniques,

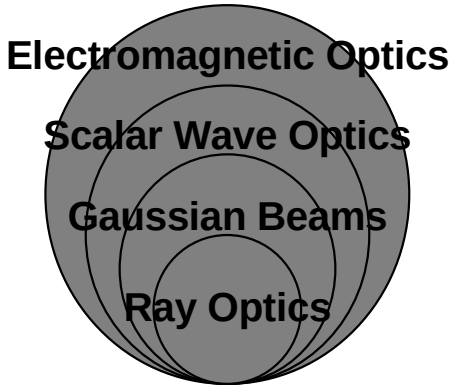

Figure 5 Optical Propagation Modeling Techniques

ray tracing, Gaussian propagation, scalar propagation and its corresponding approximations, and vector propagation. At the end of each section, we summarize the propagation technique in a table, stating the advantages and disadvantages of each technique, along with the computational order of using the specified technique.

2.2.1 Ray Tracing Technique

Ray, or geometric, optics is the simplest of the optical propagation methods. This method traces ideal rays of light through refractive elements. It has no inherent support for the optical characteristics of light, such as intensity, phase, and power or for diffractive components. However, ray propagation does give a fast calculation of the direction of the beam as it propagates through a system, therefore, many existing software packages, such as Code V [(14)], ZEMAX [(15)], and OSLO [(16)], use this technique for directional propagation. These software packages, however, propagate thousands of rays through the systems in order to calculate a wavefront at the desired observation point in the system. The computational complexity of ray propagation models is on the order of the number of beams that are being propagated, O(B). Although there is no

inherent support for diffraction in the ray optical models, limited diffraction modeling in the far-field can be calculated by performing a Fourier transform on a wavefront created with the trace of many rays [17].

The advantages and disadvantages of the ray propagation method are summarized in the following table:

Table 2 Advantages and Disadvantages of Ray Propagation

Advantages	Disadvantages	Computation Speed
Computationally Efficient	No optical signal characterization in single beam	O(B)
	Limited diffractive far-field support	

2.2.2 Gaussian Techniques

Ray propagation can be improved by modeling an optical signal with a Gaussian beam. Using Gaussian optics, the paraxial Helmholtz equation is satisfied. In this propagation technique, a Gaussian beam is superimposed over the propagating geometric rays supporting optical parameters such as waist size, depth of focus, intensity, and phase, meeting many of the criteria required to model optical MEM systems. Using nine scalar parameters to define a Gaussian beam and the ABCD matrix equations for optical interfaces of specific components, no explicit integration is needed to calculate the resulting Gaussian beam at each component [13]. Therefore, each optical component can be seen as a “black box” in which the input and output are Gaussian beams, with the component transferring the input beam to the output beam by altering the Gaussian parameters

according to the functionality of the component. An additional benefit of using Gaussian analysis is that we can approximate the optical behavior and shape of lasers typically used as input sources in optical micro-systems. Similar to the ray propagation technique, one of the largest advantages of the Gaussian method is the fast computational speed of the simulation. Again, the computational complexity for the Gaussian propagation models is on the order of the number of beams that are being propagated, O(B).

One of the biggest disadvantage of Gaussian propagation for optical micro-systems is the lack of diffraction support. However, limited diffraction modeling for symmetrically circularly clipped Gaussian beams can be supported in Gaussian optical methods at large propagation distances[18][19]. Further diffractive extensions could be performed with Hermite-Gaussian modeling for multi-mode Gaussian beams, and Laguerre-Gaussian modeling, which uses the Bessel function in cylindrical coordinates [13]. An additional disadvantage of using the Gaussian technique is that it is limited to paraxial systems, where the angle of the intersection of the optical beam and a component is considered small enough to satisfy the approximation: $\sin(\theta)=\theta$.

Even though Gaussian methods are ideal for interactive CAD design, the limited diffraction support reduces the effectiveness of these optical techniques for modeling optical micro-systems. However, for refractive macro-sized systems, both the Gaussian and Ray techniques are valid and simulate efficiently.

The advantages and disadvantages of the Gaussian beam propagation method are summarized in the following table:

Table 3 Advantages and Disadvantages of Gaussian Propagation

Advantages	Disadvantages	Computation Speed
Computationally Efficient	Limited diffractive support	O(B)
Optical signal characterization	Limited to paraxial beam	
Model with 9 scalar parameters	Far field support	
No integration required for propagation		

2.2.3 Scalar Methods

Acknowledging that diffractive optical propagation models are required for optical micro-systems, we continue our search for the appropriate optical propagation method with scalar diffraction models.

Scalar approximations are developed by recasting Maxwell's equations into a scalar form, where all components in the electric and magnetic field can be summarized by a single scalar wave equation. The Maxwell equations with the absence of free charge, are [20]:

$$\nabla\times\vec{E} = -\mu\frac{\partial\vec{H}}{\partial t} \qquad \nabla\times\vec{H} = \varepsilon\frac{\partial\vec{E}}{\partial t} \qquad \nabla\cdot\varepsilon\vec{E} = 0 \qquad \nabla\cdot\mu\vec{H} = 0$$

where, $\vec{E}$ is the electric field vector and $\vec{H}$ is the magnetic field vector, each with three rectilinear components. Both vectors are functions of position and time. μ and ε are the permeability and the permittivity of the medium in which the optical wavefront is propagating.

These equations can be recast into the following form:

$$\nabla^2 \vec{E} - \frac{n^2}{c^2}\frac{\partial^2 \vec{E}}{\partial t} = 0 \qquad \nabla^2 \vec{H} - \frac{n^2}{c^2}\frac{\partial^2 \vec{H}}{\partial t} = 0$$

where, *n* is the refractive index of the medium and *c* is the velocity of the light propagating in a vacuum, and is defined by:

$$c = \frac{1}{\sqrt{\mu_0 \varepsilon_0}}$$

The subscript "$_0$" denotes propagation in a vacuum.

If we assume that the dielectric medium is linear, isotropic, homogeneous, and nondispersive, (satisfied by the propagation through free-space) all components in the electric and magnetic field can be summarized by the 2D scalar wave equation:

$$\nabla^2 \vec{U} - \frac{n^2}{c^2}\frac{\partial^2 \vec{U}}{\partial t} = 0$$

For monochromatic light, *U(P,t)* is the positional complex wave function, where *P* is the position of a point in space:

$$U(P, t) = a(P)e^{j\varphi(P)}e^{j2\pi\nu t}$$

where, *v* is the optical frequency.

Similar to the vector solution, this complex scalar must also satisfy the wave equation, known as the time-independent Helmholtz equation: $(\nabla^2 + k^2)U = 0$, where, the wave number, $k = \frac{2\pi}{\lambda}$.

It should be noted that scalar diffraction neglects the fundamental vector nature of the electric field, therefore polarization effects are not characterized [(20)]. However, through such techniques

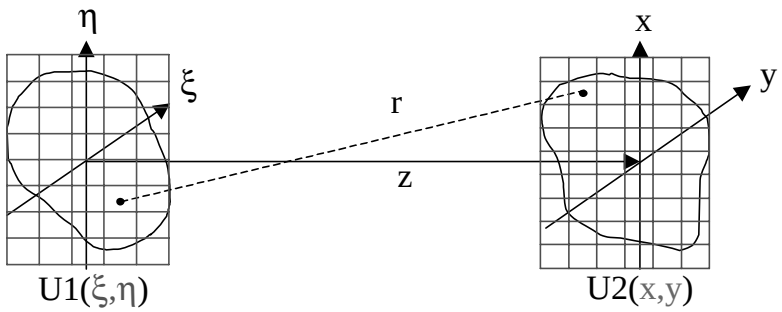

Figure 6 Scalar Meshing of Surfaces

as propagating two orthogonal polarized electric fields the polarization of light can be modeled, even when performing scalar diffraction propagation [21].

With use of Green's theorem, the Rayleigh-Sommerfeld formulation can be derived from the wave equation for the propagation of light in free-space [20]:

$$U2(x,y) = \frac{z}{j\lambda}\iint_{\Sigma} U1(\xi,\eta)\frac{e^{jkr}}{r}d\xi d\eta$$

where, $k = \frac{2\pi}{\lambda}$, Σ is the area of the aperture, z is the distance that the light is propagated from an aperture plane ($z = 0$) to an observation plane (at distance z), and r can be calculated as:

$$r = \sqrt{z^2 + (x-\xi)^2 + (y-\eta)^2}$$

It is assumed that the two planes are parallel, with a coordinate system (ξ,η,0) in the aperture plane and a coordinate system (x,y,z) in the observation plane, as seen in Figure 6. The formulation is valid as long as both the propagation distance and the aperture size are greater than the wavelength of light. These restrictions are based on the boundary conditions of the Rayleigh-Sommerfeld formulation, and the fact that the electric and magnetic fields cannot be treated independently at the boundaries of the aperture [20].

This Rayleigh-Sommerfeld formulation mathematically describes the Huygens-Fresnel principal, which states that each point on a complex wavefront acts as a source of spherical wavefronts propagating to the observation plane. These wavefronts inherit the intensity and phase values of their source point in the original complex wavefront [23].

From these scalar equations, different approximations can be used to solve the resulting complex wave function as light propagates through free-space to an observation plane. Figure 7 is a tree that begins at the top with Maxwell's equations and branches downward through the different abstraction levels of scalar modeling techniques. Along the arrows, notes are added stating the limitations and approximations that are made to get to the next, less accurate model.

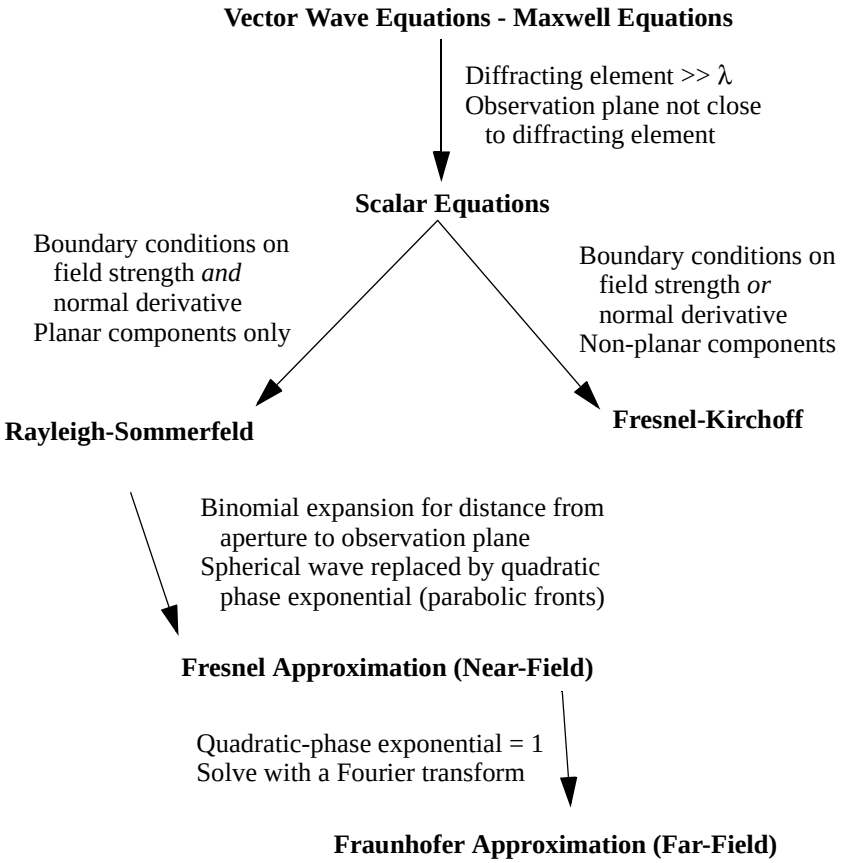

Figure 7 Diffractive Modeling Techniques

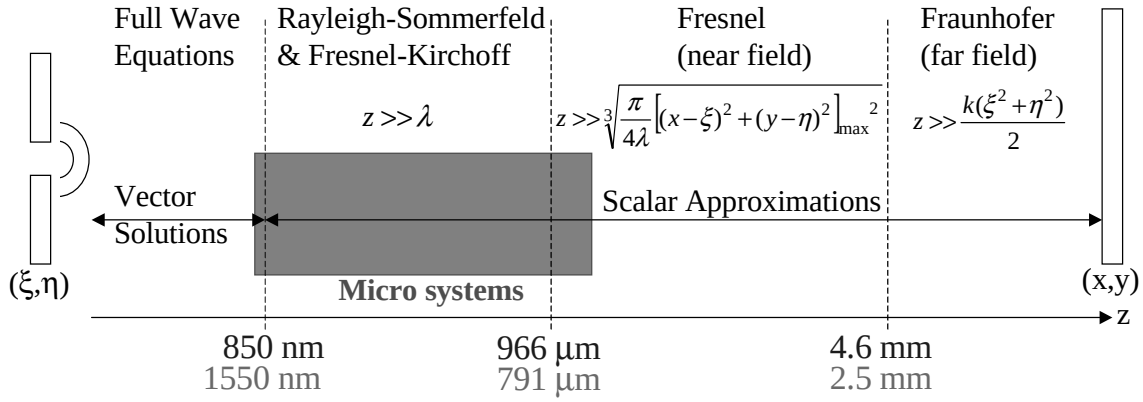

Examples: 50 μm Aperture, 200 μm Observation, λ=850 nm, λ=1550 nm

Figure 8 Optical Propagation Distance, *z*, and Model Validity

Figure 8 shows light passing through an aperture plane *(ξ,η)*, propagating a distance *z* past the aperture, and striking an observation plane *(x,y)*. The figure also presents equations calculating the validity of the diffractive models and approximations, in terms of the distance propagated past the aperture, *z*, the limits of the aperture and observation planes, the wavelength of light, λ, and the wave number, $k=2\pi/\lambda$. Using these two figures as guides, we now examine the common scalar approximations.

2.2.3.1 Fraunhofer (Far-Field) Approximation Working from the bottom to top of Figure 7 and from right to left of Figure 8, we first investigate the least accurate of the scalar approximations, the Fraunhofer approximation. The advantage of this technique is the ability to implement a Fourier transform to solve the complex wave function. The Fraunhofer technique is valid when the light striking the aperture plane can be assumed to be a plane wave [22]. Most diffractive software tools perform Fraunhofer propagation, using a common Fast Fourier Transform (FFT) routine for efficient evaluation. The FFT has a computational complexity of $O[N^2\log(N)]$, where *N* is

the number of samples along one side of the input plane [21]. As shown in Figure 8, the Fraunhofer approximation is valid in the "far-field", where the light has propagated to a distance far from the aperture, and the diffraction pattern is essentially the same as that at infinity. However, for most optical MEM systems, the optical wavefront does not propagate far enough to reach the far-field. To illustrate the problem of this method with respect to traditional micro-optical systems, we consider a system with an aperture plane (ξ,η) of 50x50 μm and an observation plane (x,y) of 200x200 μm, using a 850 nm light source. Using these parameters and the equation of minimum propagation distance for valid Fraunhofer approximation results[20] found in Figure 8, the minimum propagation distance for the Fraunhofer approximation to be valid is 4.6 mm, approximately 10 times the propagation pitch found in the switch example of Figure 1. With a wavelength of 1550 nm, a typical wavelength for fiber applications, the propagation distance needs to be approximately 2.5 mm for the Fraunhofer technique to be valid.

The advantages and disadvantages of the Fraunhofer (far field) approximation method for optical propagation is summarized in the following table:

Table 4 Advantages and Disadvantages of the Fraunhofer Approximation

Advantages	Disadvantages	Computation Speed
Solve with a FFT	Limited to far field support	$O(N^2 \log N)$
Supports diffraction		

2.2.3.2 Fresnel (Near-Field) Approximation To remove the plane-wave limitation of the far-field, our study moves up the tree found in Figure 7 towards more rigorous optical models. We next examine the Fresnel approximation, valid in both the far and near field, where the wavefront

is assumed to be parabolic as it strikes the observation plane. The “near field” is defined as the region closer to an aperture where the diffraction pattern differs from that observed at an infinite distance. No longer can a straight-forward fast Fourier transform be used for this calculation, as the light striking the aperture plane is no longer a plane wave and an explicit integration of the wavefront must be calculated. It is to be noted, however, that with some extra pre-computation, there are methods to perform an FFT algorithm for the Fresnel approximation [20]. Without the use of the Fourier transform, the complexity of the Fresnel approximation is on the order of $O(N^2M^2)$, where *N* is the number of samples along one side of a square input plane, and *M* is the number of samples along one side of the square observation plane [21]. Using the same example as before, with 850 nm light propagating through an aperture of 50 μm to an observation plane of 200μm, we can solve for the minimum propagation distance for the Fresnel approximation, as found in Figure 8. We find the propagated distance must be larger than 966 μm, approximately twice the propagation distances found in the switch example of Figure 1, making this method invalid for some optical MEM systems. Therefore, our search for an appropriate optical propagation method returns to the original scalar models to support the propagation region shorter than the near field.

The advantages and disadvantages of the Fresnel (near field) approximation method for optical propagation are summarized in the following table:

Table 5 Advantages and Disadvantages of the Fresnel Approximation

Advantages	Disadvantages	Computation Speed
Supports diffraction	Computationally slow	$O(N^2M^2)$

Table 5 Advantages and Disadvantages of the Fresnel Approximation

Advantages	Disadvantages	Computation Speed
Supports near-field propagation	No near-near field support	

2.2.3.3 Rayleigh-Sommerfeld/Fresnel Kirchoff Formulations We return our examination of optical propagation modeling techniques to the more rigorous scalar diffraction models, the Fresnel-Kirchoff and Rayleigh-Sommerfeld scalar formulations. Both of these methods produce similar, accurate results, again with the use of an explicit integration of the complex wavefront. The difference between the two methods lie in their handling of the boundary conditions. Fresnel-Kirchoff has boundary conditions on both the field strength and the normal derivative. These boundary conditions state that for a complex wavefront striking a component with an aperture surrounded by a screen, the field distribution and its derivative are the same as if the screen did not exist. The second condition states that the screen can be neglected and only the field distribution over the aperture is a concern. However, both of these boundary conditions can not be true, as the screen will perturb the fields on the aperture plane. The Rayleigh-Sommerfeld formulation removes this inconsistency and imposes boundary conditions on either the field strength or the normal derivative, since they are related. Unlike the Fresnel-Kirchoff formulation, the Rayleigh-Sommerfeld is limited to planar components. Both formulations are limited by the restriction that the propagation distance and the aperture size must be greater than the wavelength of light.

By satisfying the system requirements of accurately modeling diffraction, small propagation distances, and refractive and diffractive components, we believe that these formulations are the appropriate optical propagation methods to use for the modeling and simulation of current optical

MEM systems.

The advantages and disadvantages of the Rayleigh-Sommerfeld and Fresnel-Kirchoff formulations for optical propagation are summarized in the following table:

Table 6 Advantages and Disadvantages of the Rayleigh-Sommerfeld and Fresnel-Kirchoff Formulations

Advantages	Disadvantages	Computation Speed
Supports diffraction	Computationally slow	$O(N^2M^2)$
Supports propagation larger than λ	Normal surfaces only	

2.2.4 Vector Solutions

For completeness in our optical propagation survey, we include propagation modeling by solving for both the electric field vector, $\vec{E}$, and the magnetic field vector, $\vec{H}$ through solutions to Maxwell's equations[20]. Although the most accurate, solving Maxwell's equations is exceedingly slow since complex vector operations are required [13][20][24]. This computation is performed in 3D, as each vector is composed of *x*, *y,* and *z* values. This method is valid for all micro-systems, however, the computation time and memory requirements are extremely demanding. This technique is rarely used in free-space propagation, however, it is commonly used for optical simulations confined by a boundary such as a waveguide or fiber. Solutions for these fields are typically done with a Beam Propagation Method (BPM) using a Fourier Transform, or a finite-difference time-domain (FDTD) algorithm [25][26]. As mentioned, the major drawback of the vector meth-

ods is the simulation time of large systems and propagation distances, as is illustrated next.

The computation order for the vector solution depends on the numerical technique implemented, typically based on direct integration or a Fourier transform. However, it is key to realize that in using the vector methods, the algorithm solves for a 3D computation window (in terms of time or propagation distance), instead of the static 2D complex wavefront at a particular propagation distance as implemented with the scalar methods. Beyond the meshing of the *xy* plane, these vector algorithms require the meshing of the third dimension, in the case of optics, propagation distance into *Z* sections. Vector solutions are required to be calculated every 1/20th of the optical wavelength to minimize numerical dispersion and guarantee accurate results [27]. Recall, that we also have to solve for each of the 3 electric and magnetic component fields (E_x, E_y, E_z and H_x, H_y, H_z) for each dynamic step in the solution. Therefore, the computational resources are intense, resulting in a direct integration computational order of $O(N^2M^2Z)$.

The advantages and disadvantages of the vector solutions to Maxwell's equations for optical propagation are summarized in the following table:

Table 7 Advantages and Disadvantages of the Full Vector Solutions to Maxwell's Equations

Advantages	Disadvantages	Computation Speed
Supports diffraction	Computationally very slow	$O(N^2M^2Z)$
Supports all propagation		
Supports all aperture sizes		

2.2.5 Optical Propagation Summary

Concluding our survey of the common optical propagation techniques, we present Table 8 which provides a quick reference of the classical propagation techniques and the different optical characteristics that can be modeled with each. Checks are placed in the boxes under the propagation method if they can support each feature. Some optical propagation methods can be extended to model optical characteristics that they do not inherently support. These are filled in with the word “Extend”. The last row of the table presents the computational order of the optical propagation algorithm, so the reader can compare the complexity of the algorithm. We will use this reference table when selecting an optical propagation technique suitable for system-level modeling of micro-systems.

Table 8 Free-Space Optical Propagation Techniques

Optical Characteristic	Ray	Gaussian	Fraunhofer	Fresnel	Rayleigh-Sommerfeld	Fresnel-Kirchoff	Vector
Direction	✓	✓					
Intensity		✓	✓	✓	✓	✓	✓
Diffraction	Extend	Limited	✓	✓	✓	✓	✓
Propagation Field		Far	Far	Near	$> \lambda$	$> \lambda$	Anywhere
Phase		✓	✓	✓	✓	✓	✓
Scattering			Extend	Extend	Extend	Extend	✓
Polarization			Extend	Extend	Extend	Extend	✓
Non-Paraxial beams			✓	✓	✓	✓	✓
Curvature of Surface	Flat	Flat	Flat	Flat	Flat	Curved	Curved
Computation Order	O(B)	O(B)	$O[N^2\log(N)]$	$O(N^2M^2)$	$O(N^2M^2)$	$O(N^2M^2)$	$O(N^2M^2Z)$

where:
B: number of beam propagated
N: number of samples on the side of aperture plane
M: number of samples on the side of the observation plane
Z: number of samples in third dimension

2.3 Optical Components

While determining the optical propagation technique suitable for optical microsystems, it is important to take into account the types of optical components that the different optical propagation techniques support. Therefore, as an additional way of comparing the optical propagation techniques, the following table presents a list of common optical micro-system components. On the top of the table are the optical propagation techniques that we have discussed in this chapter, and a check is placed in the box for the optical propagation techniques that support these components. It is important to note that this table is composed with the understanding that the optical propagation techniques are used without extensions which might increase the optical component which they can support. For example, with thousands of rays propagating through a system and post processing of the rays, Ray tracing analysis has increase to support many optical characteristics, which a single ray can not support. The optical propagation technique in the last column, titled the angular spectrum technique, is an efficient calculation of the Rayleigh-Sommerfeld technique, which is the subject of Chapter 3.

Table 9 Support for Optical Components with Non-Extended Optical Propagation Techniques

Optical Characteristic or Component	Ray	Gaussian	Fraunhofer	Fresnel	Rayleigh-Sommerfeld	Fresnel-Kirchoff	Vector	Angular Spectrum
Non-Paraxial			✓	✓	✓	✓	✓	✓
Surface Roughness					✓		✓	
Spherical Surface		✓			Slightly	✓	✓	
Tilted					✓		✓	✓
Plane Mirror	✓	✓	✓	✓	✓	✓	✓	✓
Spherical Mirror		✓			Slightly	✓	✓	
Refractive Lens		✓	✓	✓	✓	✓	✓	✓
Diffractive Lens			✓	✓	✓	✓	✓	✓
DOEs			✓	✓	✓	✓	✓	✓
Phase Mask/ Holograms			✓	✓	✓	✓	✓	✓

2.4 Choosing an Appropriate Technique: Rayleigh-Sommerfeld Formulation

From our evaluation, we have determined that the required accuracy for optical micro-system modeling requires the use of full scalar formulations or complete vector solutions. As seen above, the vector solutions are computationally demanding, therefore, we choose to use the scalar method. As we have determined, the far and near field approximations are not valid for typical micro-system propagation distances or aperture sizes. Therefore, we must use the full scalar Rayleigh-Sommerfeld formulation. We now re-evaluate the computation efficiency of this scalar

method to ensure our system-level CAD requirements are also satisfied.

Examining the Rayleigh-Sommerfeld equation[28], which we have chosen over the Fresnel-Kirchoff due to consistencies in the boundary conditions [20], we recall that an explicit integration is required:

$$U2(x, y) = \frac{z}{j\lambda}\iint_{\Sigma} U1(\xi, \eta)\frac{e^{jkr}}{r}d\xi d\eta$$

Since the scalar approximations mesh the aperture and observation planes to calculate the complex wave function (seen previously in Figure 6), we further examine the 2D meshing. Using a brute-force integration technique, the Rayleigh-Sommerfeld formulation is on the computational order of $O(N^2M^2)$ when calculating the new complex wavefront. If the aperture and observation plane are the meshed with the same granularity, the order is $O(N^4)$. A computationally intensive portion of this algorithm is in the calculation of the distance between the a point on the aperture plane and a point on the observation plane, denoted as the distance *r*. Determining the exponential of *r* requires a large number of operations, slowing the algorithm. Many of the variables in the Rayleigh-Sommerfeld equation can be precomputed and reused, saving computation time, however, *r* is calculated between every mesh point on the aperture and observation planes, resulting in the computational order of $O(N^2M^2)$. In our coding of this integration, *r* is calculated by determining the coordinates of each of the mesh points in both planes and then performing the square root of the summed squares.

The computation time of this scalar technique is therefore based on the resolution of the mesh imposed on both the aperture and observation plane. For each mesh point in the observation plane, *U(x,y)*, a double integration is performed over every mesh point in the aperture plane, *U(*ξ,η*)*. This is costly in computation time, however, reductions can be made. First, computation

time can be saved by decreasing the number of mesh points used to represent the complex wave function, however, this usually results in a cost in accuracy. Second, in systems with radial symmetry, polar coordinates can be used which reduces the integration to a single integral. Finally, the specific numerical algorithm performing the integration factors largely in the computation time.

We see that with a brute force integration technique, this technique is computationally demanding. This integration can limit the interactive nature of a system-level CAD tool. Therefore, in the next chapter, we introduce a solution to the Rayleigh-Sommerfeld formulation that uses the Fourier transform to achieve the computational efficiency of the Fraunhofer technique, $O(N^2 \log N)$, but maintains the accuracy of the full Rayleigh-Sommerfeld Formulation.

However, first we investigate the current research and commercial CAD tools available for optical propagation and the CAD tools that are available for system-level simulation of mixed-domain systems.

2.5 Related CAD Tools and Research

In this section, we survey a variety of commercial and academic optical free-space CAD tools and system-level mixed-signal CAD tools. From this discussion, we can see the current state of multi-domain tools and see how our research differs and supports efficient system-level simulation of optical micro-systems.

We first examine some free-space propagation tools. Code V, from Optical Research Associates (ORA), is a standard in the field of optical CAD modeling and simulation [12]. They specialize in the design and optimization of lenses. Code V is based on Ray propagation, where systems

are simulated by the propagation of many rays through the system. An energy field is calculated at the observation plane, and from this field, information and analysis about the optical light (insertion loss, crosstalk, etc.) can be determined. ORA has recently added the capability for diffraction effects and elements within Code V, however it does not model the light emitters, such as LED or VCSELs.

ASAP, Advanced Systems Analysis Program, from Breault Research Organization (BRO) is another standard in optical software [29]. Again, this system uses Ray tracing as its optical propagation method. ASAP uses unconstrained 3-D component models, and analyzes the ray tracing of multiple beams. BRO also incorporates a "source builder", supporting user models of emitters such as lasers and LEDs. With this feature, designers can implement and use realistic sources.

Researchers at the University of California, San Diego have looked into the needs for a free-space opto-electronic CAD system [30]. They presented an integrated CAD system for free-space optical interconnects based on existing CAD technologies. Guidelines for developing compatible tools were described, and two in-house OE CAD tools, one for developing computer-generated holograms (CGH) and the other a VHDL simulator for FS-O/E systems, have been designed.

LightPipes, from the Electronic Instrumentation laboratory of TU Delft, is designed to model diffractive effects in coherent optical devices [31]. LightPipes consists of a number of filters that represent optical elements for free-space light propagation. The filters include apertures, intensity filters, beam-splitters, lenses, and models of free space diffraction. These filters are placed together to display the diffractive effects found in a free space system. The propagation is based on the Fresnel-Kirchoff scalar propagation.

iSmile and iFrost, developed by the University of Illinois, are two opto-electronic CAD tools. The tools, techniques, and methodologies have been published in [32]. With these tools, users can

simulate gate level device modeling in iSmile, and simulate systems in iFrost [33]. The system-level fiber work is now available commercially within RSoft's LinkSim CAD tool [11].

To simulate system-level mixed-domain behavior, two common techniques are to use Spice and HDL languages. In Spice tools, electro-static gaps and mechanics can be simulated with a combination of RCL components. However, for optical components, there is no real translation from the electrical models to the optical domain, although work has been done in the modeling of opto-electronic components, such as VCSELs and MSM photodetectors [34][35]. Even in this modeling work, the optical model is usually based only on emitted optical power.

The University of Toronto is developing OE^{UT}-Spice [36]. This CAD tool is used to design and optimize opto-electronic integrated circuits (OEICs), based on fiber interconnects. This low-level tool models devices with parameters such as temperature, materials, biases, duty cycles, and inter-device spacings.

Since all photonic signals are described in terms of electrical signals, the physical shape of the optical output, diffractive effects, and propagation of the beam are not modeled or simulated. Therefore, this is not a successful transition from electrical modeling to a mixed-domain simulator. Hardware description languages have had more success, as seen next.

Analog hardware description models (AHDL) have successfully been used for system-level modeling of mixed-signal systems [9][35][37]. As a successful example of some optical modeling using an HDL, Kazi et al. has shown results from modeling a wavelength division multiplexing (WDM) communication system in VHDL [38]. Optical fiber applications are more suitable for an HDL language, as the shape of the optical beam constrained in the fiber is not as critical as it is in free-space. Therefore, the optical signals are represented only by the amplitude, frequency, time, and phase parameters.

During an internship at Microcosm Technologies during the summer of 1999, the author implemented optical propagation, based on the free-space Gaussian optical propagation techniques found in Chatoyant, into Coventor CAD framework [39]. Coventor's system-level tool, *MEMSys*, is based on Avant!'s Saber and has been successfully used to model mixed-signals of mechanical, electrical, and fluidic nature. Saber is coded in MAST, Analogy's AHDL language. Mechanical parameters into *MEMSys* are extracted from *MEMCAD*, Coventor's finite element device-level tool, and used in this system-level tool. *MEMSys* was expanded to support optical models, since two of the three desired domains (electrical and mechanical) are already modeled, and the research was concentrated on only the inclusion of the optical domain. An additional advantage of using *MEMSys* is that the model parameters for the electrical and mechanical domains can be automatically extracted from physical MEMS models in MEMCAD and used in these mixed-domain simulations.

However, there are disadvantages associated with system-level, mixed-domain modeling in an AHDL. The first problem is in the accurate modeling of the optical domain. There are no inherent through and across variables for the optical domain. Currently, optics are modeled using scalar parameters, defining a Ray or Gaussian beam with parameters such as position, direction, intensity, and phase. This leads towards a "data flow" analysis, within the "continuous" domain of the electrical and mechanical simulations. When the data gets to the scheduled component, the component will activate and pass its result to the next scheduled component. Within this domain, the light propagation between components is considered instantaneous. Another disadvantage when using Gaussian optical propagation is that the diffractive effects, commonly seen in optical MEM systems, are not supported.

We now proceed by presenting an efficient solution to the Rayleigh-Sommerfeld optical propagation formulation, which can be used in a system-level CAD tool supporting optical micro-systems.

3.0 EFFICIENT SCALAR PROPAGATION

In this chapter, we introduce the angular spectrum optical propagation technique, a method that reduces the Rayleigh-Sommerfeld formulation from an brute force integration order of $O(N^4)$ to order $O(N^2 \log N)$ with the use of a Fast Fourier Transform. As will be seen, in theory, the accuracy of the Rayleigh-Sommerfeld formulation is not compromised using this angular spectrum technique.

3.1 Optical Propagation using the Angular Spectrum

As an alternative to direct integration over the surface of the wavefront, the Rayleigh-Sommerfeld formulation can also be solved using a technique that is similar to solving linear, space invariant systems. In this case, the complex wavefront is analyzed across its spatial surface with a Fourier transform. As expected, the Fourier transform identifies the frequency components of the spatial input, however, these frequency components can also be realized in the angular spectrum domain, where the spatial frequencies represent plane waves traveling in different directions away from the origin of the transform [20]. Therefore, by using the Fourier transform a complex optical wavefront is reduced into a set of simple exponential functions (i.e., plane waves). This is illustrated in Figure 9.

As with the Rayleigh-Sommerfeld formulation, the angular spectrum optical propagation technique models light propagating from an aperture plane at z=0 to a parallel observation plane at a distance z from the aperture plane. The input complex wave function U(x,y,0) has a 2D Fou-

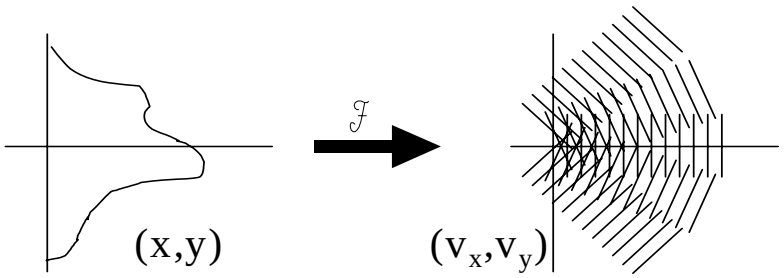

Figure 9 Angular Spectrum Decomposition of a Complex Optical Wavefront

rier transform in terms of spatial frequencies, v_x and v_y:

$$F\{U(x, y, 0)\} = A(v_x, v_y, 0)$$

$$A(v_x, v_y, 0) = \iint U(x, y, 0)\exp[-j2\pi(v_x x + v_y y)]\partial x \partial y$$

where, $v_x = \frac{\sin\theta_x}{\lambda} = \frac{\alpha}{\lambda}$ $\quad v_y = \frac{\sin\theta_y}{\lambda} = \frac{\beta}{\lambda}$.

where, $\sin(\theta_x)=\alpha$ and $\sin(\theta_y)=\beta$ are the directional cosines of the plane wave propagating from the origin of the coordinate system, as seen in Figure 10. These directional cosines and the spatial frequencies define the angular frequencies of the plane waves propagating from the aperture plane to the observation plane, as seen above. Using the angular frequencies, the above equation can be rewritten as:

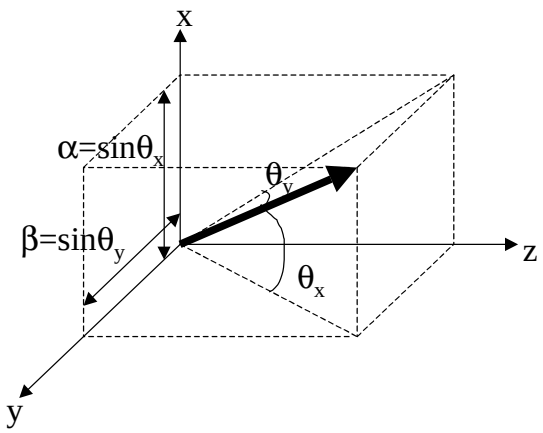

Figure 10 Graphical Definition of Angular Frequencies

$$A\left(\frac{\alpha}{\lambda}, \frac{\beta}{\lambda}, 0\right) = \iint U(x, y, 0) \exp\left[-j2\pi\left(\frac{\alpha}{\lambda}x + \frac{\beta}{\lambda}y\right)\right] \partial x \partial y .$$

The above function is called the angular spectrum of the function U(x,y,0).

Throughout this thesis, we use the terms spatial frequencies and angular frequencies almost interchangeably, as they are simply related by the wavelength of optical wavefront. We continue our discussion with the notation of the spatial frequencies, v_x and v_y, since this is more failure to the user of the Fourier transform, and is simpler in notation.

The inverse 2D Fourier transform is defined as:

$$U(x, y, 0) = \iint A(v_x, v_y, 0) \exp[j2\pi(v_x x + v_y y)] \partial v_x \partial v_y$$

In the above equations, *A* is the complex amplitude of the plane wave decomposition defined by the specific spatial frequencies.

As previously mentioned, the forward Fourier transform maps the complex optical wavefront into elementary plane waves. From examining the forward Fourier transform, the plane waves are represented by:

$$\exp[-j2\pi(v_x x + v_y y)]$$

This same term, without the negative sign, can be seen in the inverse Fourier transform equation, as all the plane waves are summed together through the integration, creating the output complex wavefunction.

The relationship of free-space propagation between two parallel planes, describing the transformation between $A(v_x,v_y,0)$ and $A(v_x,v_y,z)$ has been computed by satisfying the Helmhotz equation with the propagated complex wave function, U(x,y,z) [20]. The Fourier transform of this propagated wave is:

$$A(v_x, v_y, z) = A(v_x, v_y, 0)\exp\left(jz2\pi\sqrt{\frac{1}{\lambda^2} - v_x^2 - v_y^2}\right)$$

This describes the phase difference that each of the plane waves, distinguished by the spatial frequencies, experiences due to the propagation between the parallel aperture and observation planes. Therefore, the wave function after propagation can be solved with the following inverse Fourier transform:

$$U(x, y, z) = \iint A(v_x, v_y, 0)\exp\left(jz2\pi\sqrt{\frac{1}{\lambda^2} - v_x^2 - v_y^2}\right)\exp[j2\pi(v_x x + v_y y)]\partial v_x \partial v_y$$

It is interesting and important to note that the above equation is simply the convolution of two functions. The first function is the input complex wave function, and the second represents the propagation effect. In fact, with careful examination of the following equivalent form of the Rayleigh-Sommerfeld equation, it can be seen that it is in the mathematical form of a two-function convolution.

$$U(x, y, z) = -\frac{1}{2\pi}\iint_{\Sigma} U(\xi, \eta, 0)\frac{\partial}{\partial z}\frac{\exp(-jkr)}{r}\partial\xi\partial\eta = \frac{1}{2\pi}\iint_{\Sigma} U(\xi, \eta, 0)\frac{\exp(-jkr)}{r}\frac{z}{r}\left(jk + \frac{1}{r}\right)\partial\xi\partial\eta$$

We now verify the complete angular spectrum equation by approaching the Rayleigh-Sommerfeld formulation as a convolution of two terms. It is well known that a convolution in the spatial domain is a multiplication in the frequency domain. This is mathematically seen for the Rayleigh-Sommerfeld method by:

$$U(x, y, z) = U(\xi, \eta, 0) \otimes \frac{\partial}{\partial z}\frac{\exp(-jkr)}{r} = F^{-1}\left[F\{U(\xi, \eta, 0)\} \times F\left\{\frac{\partial}{\partial z}\frac{\exp(-jkr)}{r}\right\}\right]$$

The term $F\left\{\frac{\partial}{\partial z}\frac{\exp(-jkr)}{r}\right\}$, is known as the free space transfer function, *H*. We can see by taking the Fourier transform of this propagation term, that we achieve the same result as seen above for the phase propagation term [17]:

$$H = F\left\{\frac{\partial}{\partial z}\frac{\exp(-jkr)}{r}\right\} = \exp\left(-jz2\pi\sqrt{\frac{1}{\lambda^2}-v_x^2-v_y^2}\right).$$

From the above equation, it is seen that using the angular spectrum method, there is no longer a need to explicitly calculate *r*, as there was in the direct integration technique. *r* is now encapsulated by the spatial frequencies, representing plane waves propagating from the aperture to the observation plane.

It is appropriate to discuss the physical effect when:

$$\frac{1}{\lambda^2}-v_x^2-v_y^2>0\,.$$

When this occurs, these plane waves are defined as evanescent waves, which carry very little power and die out within a propagation distance of a couple of wavelengths of the optical wavefront[40]. In terms of the angular frequencies, the evanescent waves are defined below, which simplify to an equation involving only the direction of propagation of the plane waves.

$$\frac{1}{\lambda^2}-\left(\frac{\alpha}{\lambda}\right)^2-\left(\frac{\beta}{\lambda}\right)^2>0 \Rightarrow 1-\alpha-\beta>0$$

In our simulations, we ignore these evanescent waves to reduce the simulation time. However, these waves can be modeled with the following free-space optical propagation transfer function:

$$H = \exp\left(-jz2\pi\delta\sqrt{\frac{1}{\lambda^2} - v_x^2 - v_y^2}\right),$$

where $\delta = 1$ for $v_x^2 + v_y^2 \leq \left(\frac{1}{\lambda}\right)^2$ or $\delta = -j$ for $v_x^2 + v_y^2 > \left(\frac{1}{\lambda}\right)^2$.

The angular spectrum method is restricted to propagation between parallel planes that share a common center. Removing these restrictions has been the goal of recent research. Tommoasi and Bianco have determined how to propagate to a plane that is tilted with respect to initial plane [41]. Delen and Hooker have determined a way to allow offsets in the observation plane [17]. We summarize these two methods next.

For arbitrary angles between the aperture plane, U(ξ,η,ζ) and the observation plane, U(x,y,z), a mapping of the spatial frequencies in each plane's coordinates system must occur. This mapping is possible due to the fact that the phase accumulation term does not change when the waves propagate to an observation plane that is not normal to the aperture plane. It can be found that the rotational matrix M, relating rectilinear coordinates (ξ,η,ζ) to (x,y,z), can be used to relate spatial frequencies in tilted systems by [41]:

$$(x, y, z)^T = M(\xi, \eta, \zeta)^T \qquad (v_\xi, v_\eta, v_\zeta) = M(v_x, v_y, v_z)^T$$

For rotation around the specific axes, M is defined as:

$$M_{\text{x-axis}} = \begin{bmatrix} 1 & 0 & 0 \\ 0 & \cos\theta & \sin\theta \\ 0 & -\sin\theta & \cos\theta \end{bmatrix}, \; M_{y\text{-axis}} = \begin{bmatrix} \cos\phi & 0 & -\sin\phi \\ 0 & 1 & 0 \\ \sin\phi & 0 & \cos\phi \end{bmatrix}, \; M_{z\text{-axis}} = \begin{bmatrix} \cos\rho & \sin\rho & 0 \\ -\sin\rho & \cos\rho & 0 \\ 0 & 0 & 1 \end{bmatrix}$$

In the new tilted coordinate system, the incoming spatial frequencies are perceived as having spatial frequencies corresponding to the observation's coordinate system. For example the incoming aperture plane wave has spatial frequencies (v_ξ,v_η = 0,0) corresponding to angle (v_x,v_y =

Figure 11 Mapping of Spatial Frequencies

-ϕ,0) in the observation plane with only a tilt of ϕ around the y-axis. This is graphically seen through the diagram in Figure 11. In all cases, even if the spatial frequencies are re-mapped, the amplitude stays the same.

For an observation plane whose center is offset from the propagation axis of the aperture plane, the Fourier shifting theorem can be used to solve for the complex wave function [17]. The coordinate systems of the aperture and observation plane need to be related through the following:

$$x = \xi - x_0 \qquad y = \eta - y_0$$

This relationship is graphically defined in Figure 12.

With this relation between the offset of the coordinate systems, the function for free-space propagation between offset planes is:

$$U(x, y, 0) = \iint A'(v_x, v_y, z)\beta \exp[j2\pi(v_x x + v_y y)]\partial v_x \partial v_y$$

where, $A'(v_x, v_y, z) = A(v_x, v_y, 0)\exp[j2\pi(v_x x_0 - v_y y_0)]$

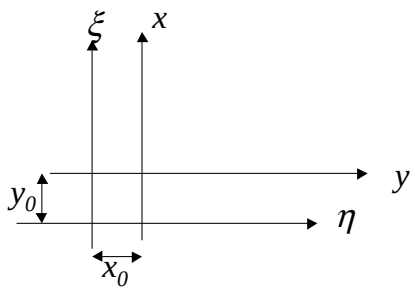

Figure 12 Relation of Offset Coordinate System

The angular spectrum technique for modeling propagation between the aperture and observation plane is summarized graphically in Figure 13. First, the forward Fourier transform is applied to the aperture surface, as seen in Figure 13(A). In stage B, each plane wave is multiplied by the propagation phase term. If tilts are present, the remapping of spatial frequencies occurs, as denoted by C. If offsets between the planes occur, then the shifting theorem is applied, as shown in step D. Finally, stage E shows the inverse Fourier transform being applied, and the complex wavefront on the surface of the observation plane is obtained.

The advantage of using the angular spectrum to model light propagation is that the method is based on Fourier transforms. In CAD tools, the Fourier transform can be implemented by one of the numerous Fast Fourier Transform (FFT) techniques [42]. The computational order of a 2D FFT is $O(N^2 \log_2 N)$, which is obviously more computationally efficient than $O(N^4)$, the computational order of the brute force direct integration method of solving the Rayleigh-Sommerfeld formulation. We show this speed increase later through example.

Like the direct integration technique, the FFT technique requires the aperture and observation planes to be discretized into NxN meshes, where N is the number of mesh points on the side of the plane. Equal spacing meshing is required, and for ease of the FFT algorithm, a power of 2 is sug-

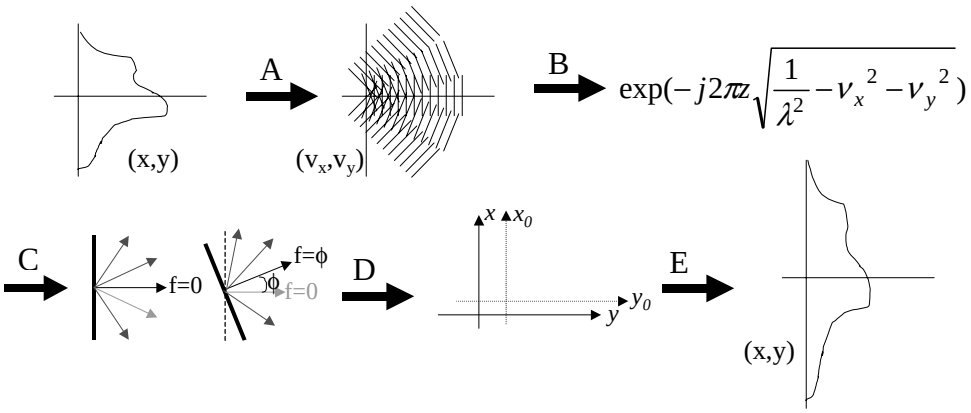

Figure 13 Angular Spectrum Algorithm Summary

gested for the number of mesh points. In this thesis, we assume that the aperture and observation planes are meshed with the same N, however, this is not a requirement.

Choosing the size and resolution of the mesh is critical for accuracy and validity of the angular spectrum method. An error discussion of using the angular spectrum method to solve the Rayleigh-Sommerfeld formulation is the emphasis of the next chapter.

3.2 Angular Spectrum and Direct Integration Comparison

To examine the computational speed-up of using the angular spectrum method, compared to direct integration of the Rayleigh-Sommerfeld formulation, we simulate a Gaussian beam propagating in free-space using both techniques. In these simulations, a 5 μm (diameter) Gaussian shaped beam with a wavelength of 1550 nm propagates 20 μm to a 10 μm square detector, as seen in Figure 14. Note that at 20 μm this system is in the "near-near" field, requiring the calculation of the complete Rayleigh-Sommerfeld formulation for accurate modeling. For the direct integration technique, a Gaussian Quadrature technique is used to solve the integration. In these simulation, the aperture and observation planes are both meshed with NxN grid points, where N is equal to 32, 64, 128, 256, and 512. Simulation results, in terms of total computation time and percent difference of power detected on the detector compared with a "base case", are reported in the following table. In lieu of a real "ground truth", we use a simulation with a large mesh number of

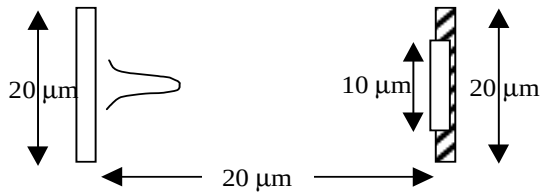

Figure 14 Gaussian Propagation Example System

N=512 to compare with as the “correct” result. This meshing will be verified as a acceptable ground truth in the following chapter detailing the error bounds of using the angular spectrum technique for a solution to the Rayleigh-Sommerfeld formulation. By examining the following table, it can be seen how the designer can trade-off simulation speed versus accuracy.

Table 10 Gaussian Beam Propagation using Angular Spectrum and Direct Integration

N (mesh side)	32	64	128	256	512
	Angular Spectrum (FFT)				
Computation (sec)	0.04	0.11	0.27	1.89	4.97
% Power Error	0.13%	0.03%	0.01%	0.00%	0.00%
	Direct Integration (Gaussian Quadrature)				
Computation (sec)	1.81	29.40	455.84	7080	116480
% Power Error	4.62%	0.97%	1.19%	0.14%	0.00%

Examining the results of the N=256 case, a simulation that uses the brute force direct integration technique takes approximately two hours to simulate. Using the angular spectrum technique using a 2D FFT, the same simulation takes approximately 2 seconds. The intensity contours of this propagated beam in this simulation are seen in Figure 15. As can be seen, the results match very well. The graph shown in Figure 16 is a plot of the computation times seen in Table 10. The slope of the line indicates the advantage of using the angular spectrum technique.

With careful examination of the direct integration intensity contours in Figure 15(a), it is seen that the Δ value between mesh points is not equal throughout the observation plane. This is due to the numerical integration technique that is implemented to solve the Rayleigh-Sommerfeld integration. We use a N-point Gaussian Quadrature technique to solve for the integration in the direct

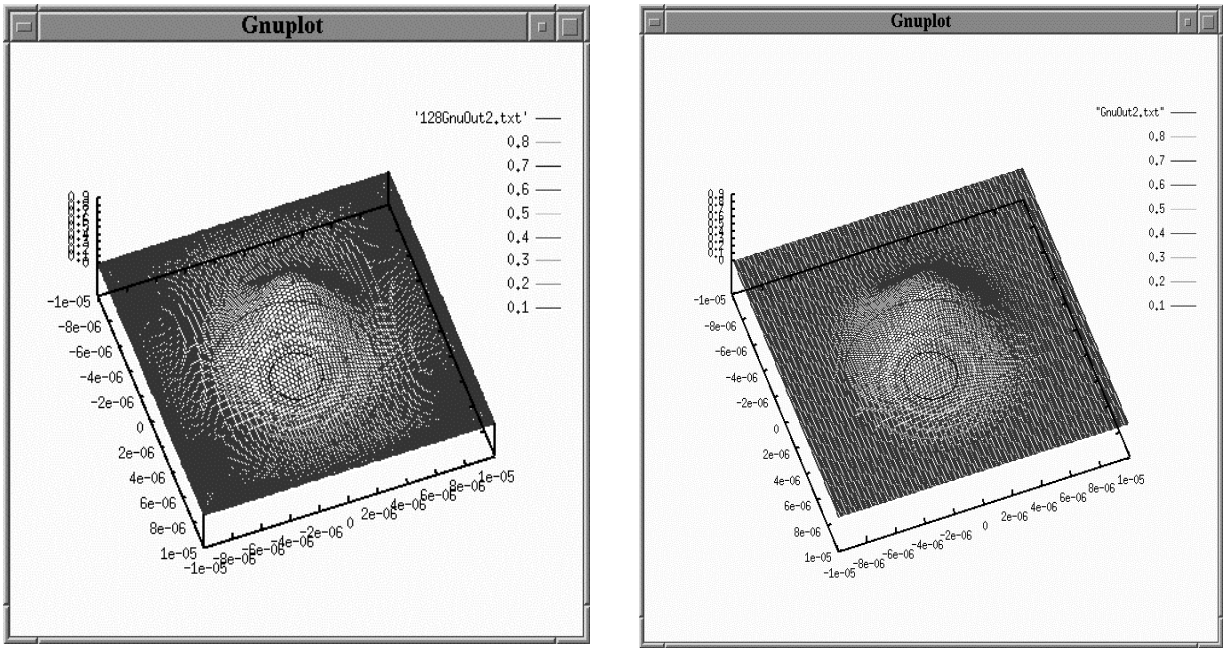

(a) Direct Integration (256x256) (b) FFT (256x256)

Figure 15 Intensity Contours of Gaussian Propagation Example System

integration method, since it is one of the most accurate approximations for integration of smooth functions. In this integration method, the distances between the mesh points are not equal, since each mesh point has a weight associated with it. This technique has fine meshing at the edges of the computational window and more course meshing in the center. Since the optical wavefront is

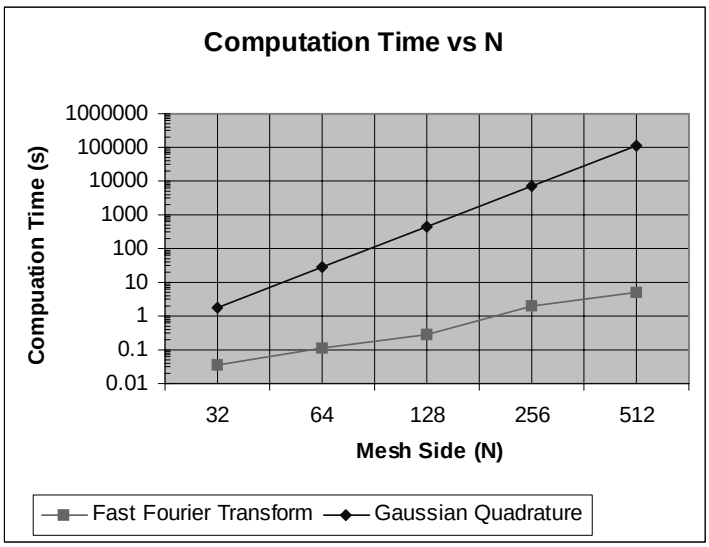

Figure 16 Computation Time vs. N for the Angular Spectrum and Direct Integration

typically in the center of the computation window, this uneven meshing reduces the accuracy of the direct integration method when compared to the angular spectrum method using the same value of N, as can be seen in Table 10.

3.3 Validation of Angular Spectrum Technique

We now validate our angular spectrum technique by comparing simulation results versus experimental results, full vector solutions, and analytical expressions.

3.3.1 Experimental Validation

We have been able to validate our technique by comparing our scalar simulation results with experimental results and full vector simulations. With assistance from Dr. Dennis Prather at the University of Delaware, we were able to compare our simulations with experimental data from optical propagation through a precision pin-hole [43]. The pin hole has a diameter of 71 μm. The light striking the pin hole has a wavelength of 632.8 nm, and is propagated past the aperture 1.5 mm. The experimental results and our scalar simulations are shown in Figure 17. Included in the figure is a FDTD vector simulation, also performed by Dr. Prather. As can be seen, the scalar simulation results match very well with the experimental data and the vector solutions.

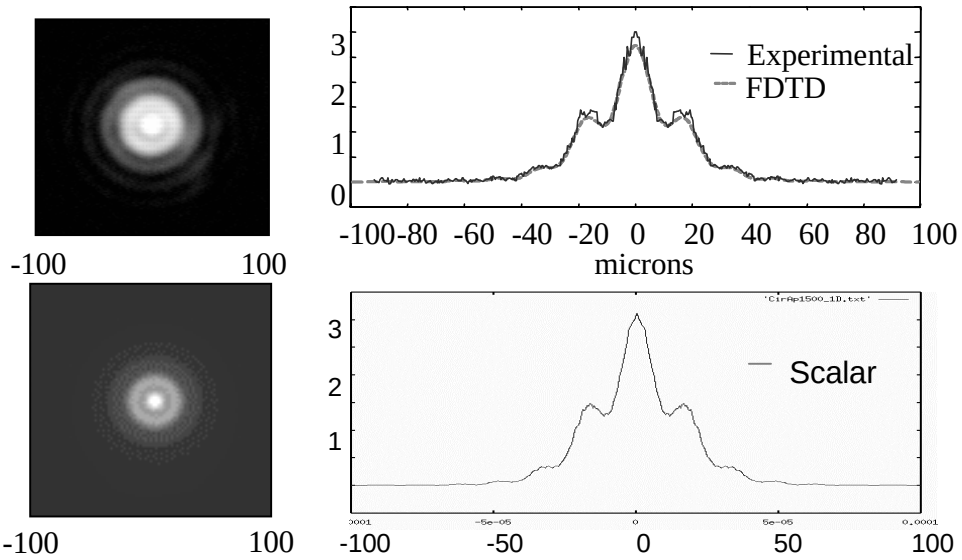

Figure 17 Scalar Simulation results vs. Experimental Data and Vector Solutions

3.3.2 Theoretical Validation

Due to the lack of experimental data to compare against our simulated results, we have also used several classical theoretical examples to verify our work.

3.3.2.1 Fresnel Diffraction by a Square Aperture In this example, we compare our simulation results using the angular spectrum method against theoretical results of a plane wave propagating through a square aperture. The square aperture has a side length of $2w$ = 50 μm. The Fresnel number is defined as $N_f = w^2/\lambda z$, and relates the size of the aperture ($2w$) and the distance that the light propagates past the aperture (z). Using the Fresnel integrals, C() and S(), the complex wave field distribution of the plane wave propagating past the aperture is [20]:

$$U(x,y) = \frac{e^{jkz}}{2j}\{[C(\alpha_2)-C(\alpha_1)] + j[S(\alpha_2)-S(\alpha_1)]\} \times \{[C(\beta_2)-C(\beta_1)] + j[S(\beta_2)-S(\beta_1)]\}$$

where,

$$\alpha_1 = -\sqrt{2}\left(\sqrt{N_f} + \frac{x}{\sqrt{\lambda z}}\right) \qquad \alpha_2 = \sqrt{2}\left(\sqrt{N_f} - \frac{x}{\sqrt{\lambda z}}\right)$$

$$\beta_1 = -\sqrt{2}\left(\sqrt{N_f} + \frac{y}{\sqrt{\lambda z}}\right) \qquad \beta_2 = \sqrt{2}\left(\sqrt{N_f} - \frac{y}{\sqrt{\lambda z}}\right)$$

Knowing that the intensity of the complex wavefront is simply related to the complex field by $I(x,y) = |U(x,y)|^2$, an analytical expression of the intensity of the wavefront as the light passes through the square aperture for a specific Fresnel number is [20]:

$$I(x,y) = \frac{1}{4}\{[C(\alpha_2) - C(\alpha_1)]^2 + [S(\alpha_2) - S(\alpha_1)]^2\} \times \{[C(\beta_2) - C(\beta_1)]^2 + [S(\beta_2) - S(\beta_1)]^2\}$$

For three different Fresnel numbers, N_f = 1, 4, and 10, corresponding to propagation distances z = 625 μm, 156.25 μm, and 62.5 μm, respectively, we simulate the intensity profile of a plane wave propagating through the square aperture using our angular spectrum method and compare these results with the analytical results. These results are shown in Figure 18, with the analytical results in the left column and the simulated results on the right. For the angular spectrum method, the mesh gridding is 512x512 for N_f=1 and 4, and 4096x4096 for N_f=10. When examining the results, we find that our technique matches the expected values well with the lower order Fresnel numbers, 1 and 4. In the simulation with a Fresnel number of 10, the results do not match exactly, however, the shape of the waveform, with 10 peaks and 9 valleys, is the same in the analytical and the simulated results.

In Figure 19, we present a point-by-point absolute difference for the N_f=4 case between the analytical results and the simulated results. It can be seen that the difference, plotted on the log scale, is less that 0.1. There are a couple of reasons for the difference. The first is that the slight

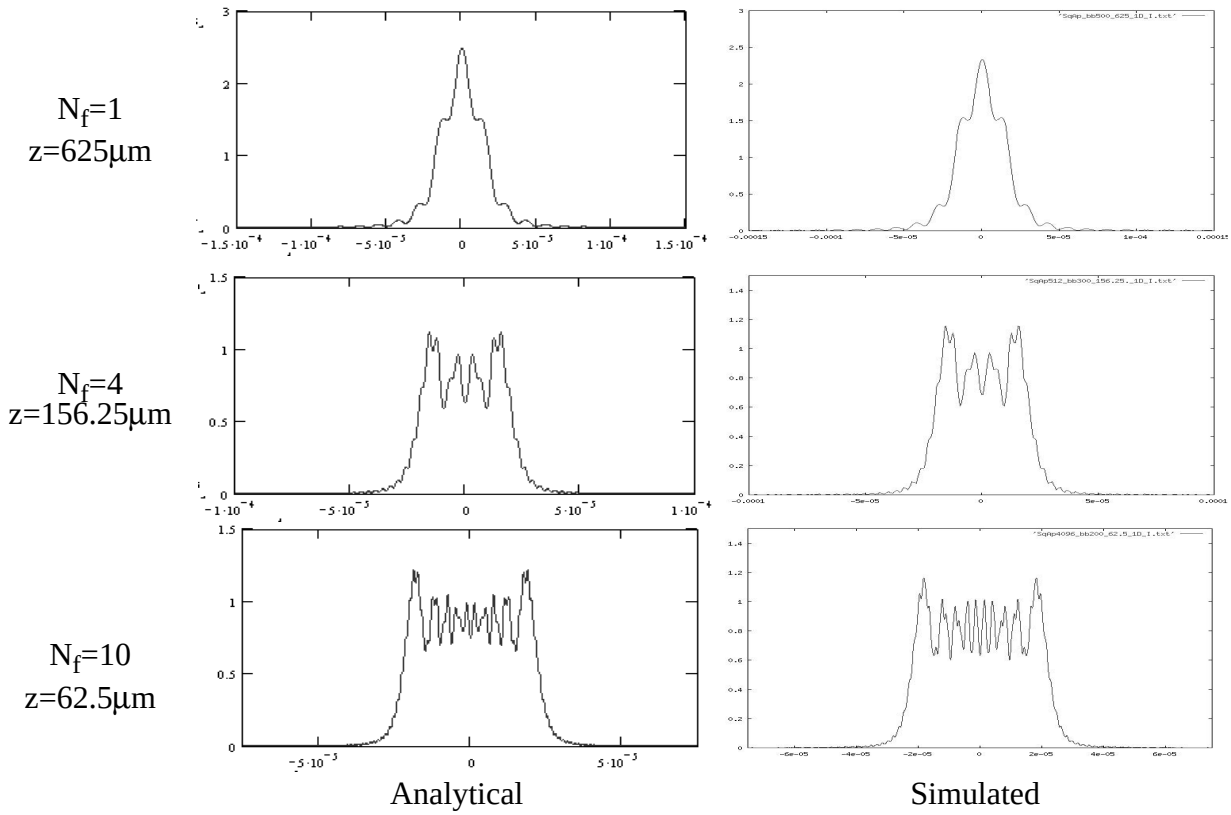

Figure 18 Simulation Results vs. Analytical Data for Propagation Past a Square Aperture

differences are caused by the number of samples and the computational window size used in the simulation. This leads to errors called aliasing and truncation, which are discussed in the next chapter. Another reason for the difference between the analytical curve and the simulated curve is

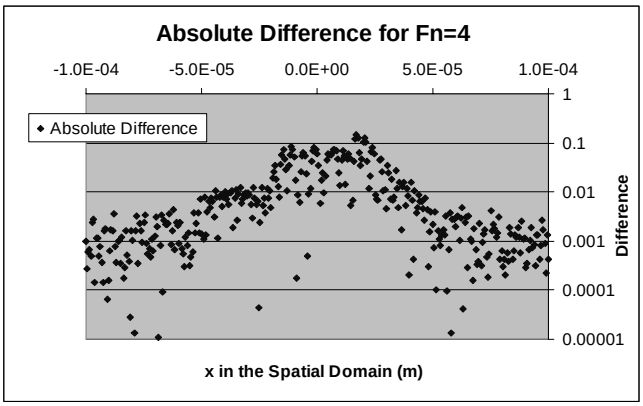

Figure 19 Point-Wise Difference Between Simulated and Theoretical Results

the calculation of the Fresnel integrals used in the analytical results, which were calculated in MathCAD. Therefore, MathCAD's integration technique, resulting in the analytical results, compared with the integration technique in the FFT, resulting in the angular spectrum results, are responsible for the differences in the data.

3.3.2.2 Diffraction by a Double Slit In this example, we compare our simulated results against theoretical results of a plane wave propagating through a double slit into the far field. The theoretical results are again provided through analytical equations for the intensity of the wavefront. A full explanation of the double thin slit experiments can be found in many texts, such as [23], and is not included here.

The double slits are defined by the width of the slits, *b*, the length, *l*, and the center-to-center distance between the slits, *a*. Light propagates a distance of *z* past the double slits. The intensity envelope of the light propagating though a double slit into the far-field is the same intensity profile of a plane wave propagating through a single slit, which has the same dimensions of one of the double slits. The theoretical far-field intensity envelope is given by the function [23]:

$$\frac{I(\theta)}{I_0} = \left(\frac{\sin\beta}{\beta}\right)^2, \text{ where } \beta = \left(k\frac{b}{2}\right)\sin\theta \text{ and } \theta = \operatorname{atan}\frac{x}{z}$$

The far-field intensity profile for the double-slit adds an interference term, as seen in:

$$\frac{I(\theta)}{I_0} = \left(\frac{\sin\beta}{\beta}\right)^2(\cos a)^2, \text{ where } \alpha = \left(k\frac{a}{2}\right)\sin\theta \text{ and } \theta = \operatorname{atan}\frac{x}{z}$$

In our simulations, a plane wave (λ=1000 nm) propagates through two thin slits, each with a length of 100 μm and a width of 10 μm. The slits are separated center-to-center by 30 μm. We present our simulation results as light passes through the two slits, and propagates 5 mm to an observation plane in the far-field. We simulate into the far field so that we can compare our simu-

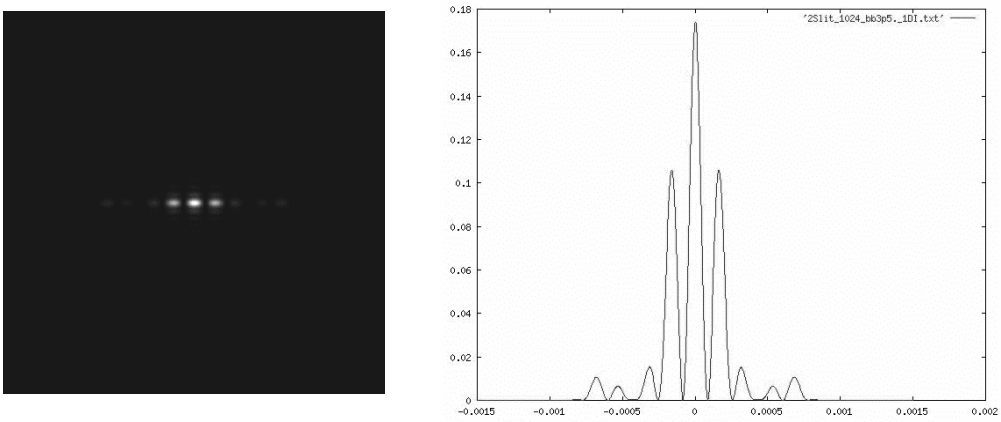

Figure 20 Double Slit Diffraction Simulation Output (z = 5 mm)

lated results with the analytical results described above. The simulation results, in both a 1D cross-section and in 2D, are shown in Figure 20.

We verify our simulation results by comparing our intensity profile with the intensity envelope of the single slit and the expected intensity distribution of the double slit. Our results match well, as can be seen in Figure 21. The differences can be attributed to the number of sampling points and size of the computation window. These can lead to aliasing and truncation in the resulting function, especially at large propagation distances when a large observation plane is

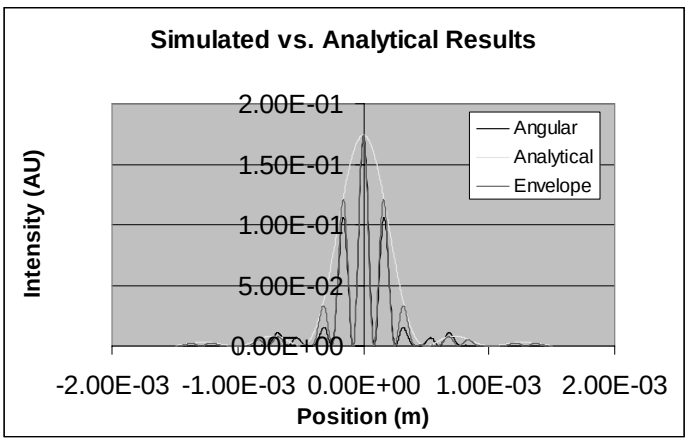

Figure 21 Intensity Envelope of Analytical and Simulate Results

required. This will be explained more in the next chapter.

We also verify the position of the ±1 diffractive mode, that is the diffraction effects that result in the intensity maximums ±1 mode from the center. Far-field diffraction theory predicts a position of:

$$x_{\pm 1\text{st mode}} = \frac{\lambda z}{a},$$

which, for our system, is 166 μm. Our simulations show the first diffraction mode at a position of approximately 161 μm. Again, this slight difference is an artifact of the sampling rate and window size chosen for the simulation.

We now move towards an understanding of the errors that can arise in using the angular spectrum method. We present common errors in using a discrete Fourier transform and discuss how to minimize errors, when using a Fourier transform to perform the angular spectrum technique.

4.0 ACCURACY AND ERROR MEASUREMENTS OF THE ANGULAR SPECTRUM METHOD

Using continuous Fourier transform theory, the angular spectrum method is an exact solution of the Rayleigh-Sommerfeld scalar formulation. However, when solving the algorithm on a digital computer, the continuous function must be discretized, which can lead to errors in both the forward and inverse Fourier transform. In this chapter, we discuss the common errors that arise from implementing a discrete Fourier transform (DFT) to approximate the Fourier transform of a continuous function. We examine the appropriate sampling of complex optical wavefronts to minimize the error bounds. For those functions in which a stronger error bound is required, we introduce a calculation of the order of error bounds when using a discrete Fourier transform for the solution of the Rayleigh-Sommerfeld formulation with the angular spectrum technique.

4.1 Discrete Fourier Transform

In the study of error estimation of the DFT, it is important to have a good understanding of the Fourier transform in both continuous and discrete theory. In this section, we first present the continuous and discrete transforms. We then introduce the spatial and frequency domains, and show how these two domains are related.

4.1.1 Discrete vs. Continuous Fourier Transform

In 1D, the continuous Fourier transform is:

$$f(x) = \int_{-\infty}^{\infty} \hat{f}(\omega) e^{j2\pi\omega x} d\omega \Leftrightarrow \hat{f}(\omega) = \int_{-\infty}^{\infty} f(x) e^{-j2\pi\omega x} dx \text{, where, } -\infty < x, \omega < \infty .$$

As the function is discretized for digital computation, the integrations become summations, and the Discrete Fourier transform is:

$$f(x) = \sum_{-\infty}^{\infty} F_k e^{j\frac{2\pi nk}{N}} \Leftrightarrow F_k = \frac{1}{N} \sum_{-\frac{N}{2}+1}^{\frac{N}{2}} f_n e^{j\frac{2\pi nk}{N}} \text{, where, } -\frac{N}{2} + 1 < n, k < \frac{N}{2} .$$

As these equations are shown in 1D, they also hold true in 2D. The forward and inverse transforms in 2D are:

$$F_{jk} = \frac{1}{NM} \sum_{m=-\frac{M}{2}+1}^{\frac{M}{2}} \sum_{n=-\frac{N}{2}+1}^{\frac{N}{2}} f_{mn} \omega_M^{-mj} \omega_N^{-nk}$$

$$f_{mn} = \sum_{m=-\frac{M}{2}+1}^{\frac{M}{2}} \sum_{n=-\frac{N}{2}+1}^{\frac{N}{2}} F_{jk} \omega_M^{mj} \omega_N^{nk}$$

We use these definitions to determine the error from using the DFT instead of the continuous Fourier transform for the solution of the Rayleigh-Sommerfeld formulation using the angular spectrum technique. Before the discussion of this error, we define the discrete nature of the spatial and frequency domains and the relationship between these two domains.

4.1.2 Relationship Between Spatial and Frequency Domains

In our use of the Fourier transform to decompose an 2D optical signal into spatial frequencies, the forward Fourier transforms converts the computational domain between the spatial and the frequency domains, and the inverse Fourier transform converts between the frequency and the spatial domain. To prepare our discussion of the error analysis in using the DFT in solve the angular spectrum method, a clear understanding of the discrete nature of the 2D spatial and frequency domains, and how they relate, is required. We start with an introduction to the spatial domain.

The spatial domain is defined with side lengths A and B, and the number of discretization (or mesh points) in each direction, N and M respectively, resulting in sample spacings of $\Delta x = A/N$ and $\Delta y = B/M$. In this discussion, it is assumed the side length A is in the "x" direction and the side length B is in the "y" direction. Therefore, the boundaries of the spatial domain are: $\{-A/2 \leq x \leq A/2, -B/2 \leq y \leq B/2\}$. The 2D spatial domain is shown in Figure 22(a).

In the frequency domain, the corresponding side lengths are defined by Ω and Λ, N and M are the same number of discretization as in the spatial domain, and the spacing between discretization is equal to $\Delta\omega$ and $\Delta\sigma$. While performing the forward and inverse Fourier transforms, N and M do not have to be the same number in both domains, however, in this discussion of the relationship between both domains, we keep them then same (N=M). In the frequency domain, the boundaries are: $\{-\Omega/2 \leq \omega \leq \Omega/2, -\Lambda/2 \leq \sigma \leq \Lambda/2\}$. The frequency domain is shown next to the spatial domain in Figure 22(b).

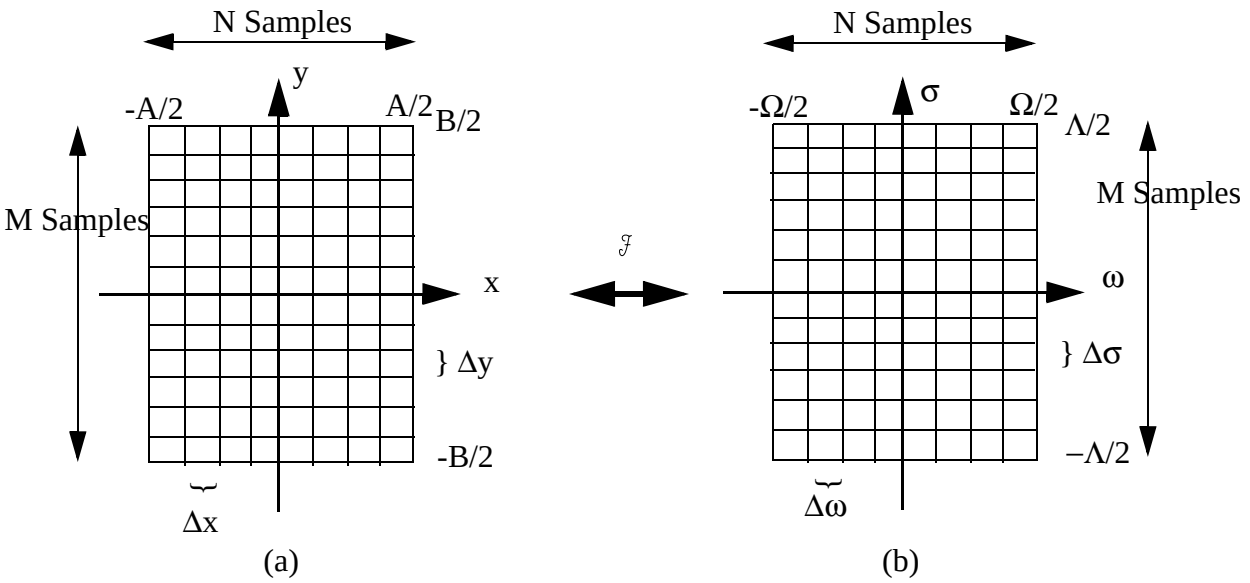

Figure 22 (a) 2D Spatial Domain and (b) 2D Frequency Domain

The spatial and frequency domains are related through the forward and the inverse Fourier transforms. Assuming that the grid length N is the same in both the spatial and frequency domain, the following reciprocity relations hold true [45]:

$$\Omega = \frac{1}{\Delta x} = N\Delta\omega \qquad \Delta x\Delta\omega = \frac{1}{N}$$

and

$$\Lambda = \frac{1}{\Delta y} = N\Delta\sigma \qquad \Delta y\Delta\sigma = \frac{1}{N}$$

This states that the lengths and the grid spacings of the spatial and frequency domains vary inversely with each other. Figure 23 illustrates the relationship between the spacing in the spatial domain and the frequency domain for specific spatial lengths and number of discretization grid points. For simplicity, Figure 23 is presented in 1D, however, the same properties hold true for 2D Fourier transforms. These relationships, possibly counterintuitive to the reader, are important for the understanding of the error estimates made later in this chapter.

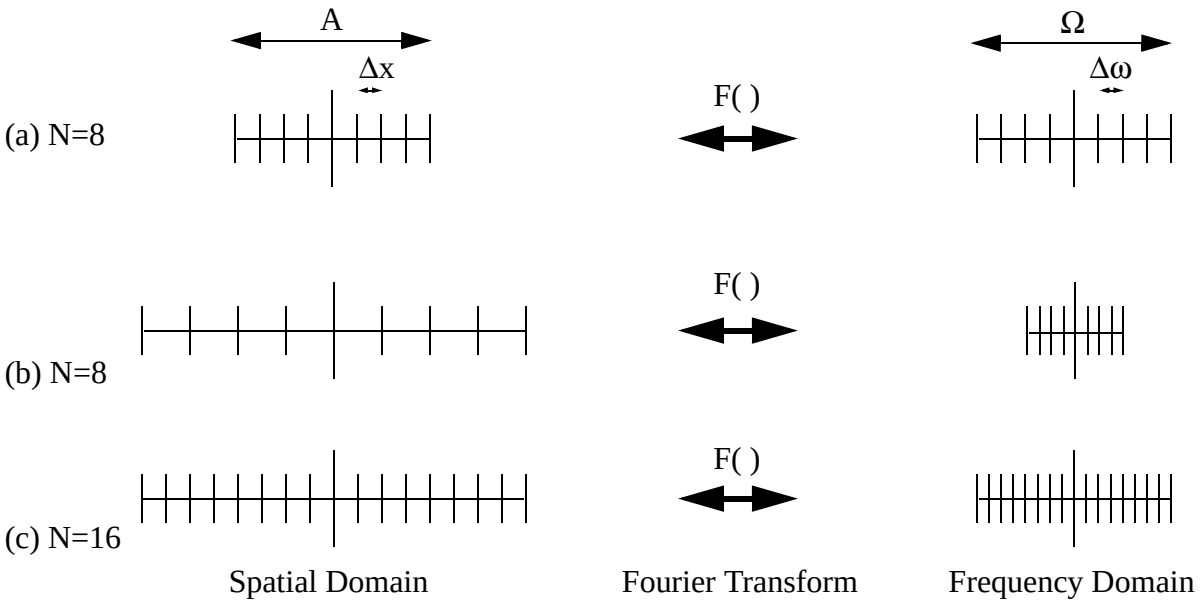

Figure 23 Relationship between Spatial and Frequency Domain

In the first case Figure 23(a), we see that sampling in the spatial domain, with a length of A, N=8, and Δx, results in the sampling in the frequency domain with $\Delta\omega$ and a length of $N\Delta\omega=\Omega$. With N held constant and Δx doubled, as in case (b), $\Delta\omega$ is halved. In other words, as the range of the spatial domain is doubled, the range of the frequency domain is halved. Therefore, by using a larger spatial domain, the frequency domain is decreased, as these domain sizes are inversely proportional.

Using the same reciprocity relations as seen before, we next examine the case when N is doubled, and A remains constant, resulting in Δx being halved. This results in the frequency domain, Ω, being doubled, as is seen in case (c) in Figure 23. In summary, to get double the refinement in the frequency domain, that is halving $\Delta\omega$, while retaining the original size of the frequency domain ($N\Delta\omega$), N and A must be doubled while keeping Δx constant.

This brief introduction gives an important understanding to the relationship between the two different domains. This intuition will help us when we start our discussion of error reduction.

However, we first examine the common errors that occur when performing a DFT.

4.2 Errors using a DFT

During the implementation of a DFT, errors are caused by the sampling of the function (in either or both of the spatial or frequency domains) and the size of the computation window in which the function is sampled. We summarize the common DFT errors in this section: aliasing, truncation, and averaging at end-points. Further details and estimations of these errors, with respect to the angular spectrum method are given later in this chapter. We begin this section with a discussion of the sampling theorem for the Fourier transform. Although, this sampling theorem is for ideal bandlimited signals, it is useful in determining error terms in using the DFT.

4.2.1 Sampling Theorem

For bandlimited signals, the sampling rate to guarantee that a function in the spatial domain f(x,y) can be reconstructed exactly from its frequency samples F_n has been defined by Claude Shannon [46]. A bandlimited signal is defined as one whose Fourier transform is zero outside of a critical frequency, f_c, as seen graphically in Figure 24. This frequency is known as the Nyquist

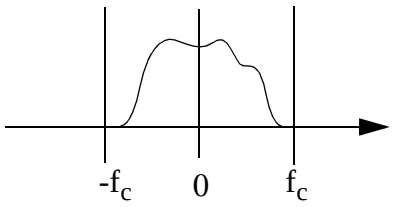

Figure 24 Bandlimited Signal

frequency, and is the highest frequency that can be resolved using the specified number of sample points. The sampling theory states that if two spatial samples are taken per cycle of the highest frequency component present in the frequency domain, the wave can be completely reconstructed. In mathematical terms, the theorem states in 1D:

$$\Delta x \leq \frac{1}{2f_c}$$

where Δx is the sampling in the spatial domain.

Most signals, including most of the complex optical signals that we simulate propagating through free-space, are not bandlimited signals. However, there are still opportunities to use the sampling theorem for our purpose of propagating optical wavefronts. We will examine these cases later in the chapter during our discussion about the characteristics of an optical wavefront.

In practice, or "real world" sampling, there is a standard rule to sample the critical frequency by at least "a few" samples. This accounts for the fact that realistic signals are rarely ideally bandlimited, as described above. Weaver suggests that the highest frequency should be sampled about 10 times/cycle for accurate sampling[47]. Wilhelm states this sampling requirement at approximately 5 samples/cycle [48].

In the remainder of this chapter, we will specifically examine the errors that occur while using an input such as an optical wave. However, first, we continue the introduction of the common errors from using the DFT.

4.2.2 Aliasing in the Frequency Domain

The most common error in using the DFT is aliasing. Aliasing occurs when frequencies exist that are greater than, or outside, the largest sampled frequency, referred to previously as the critical sampling frequency, f_c. These frequencies outside the sampling region are falsely translated (or aliased) into the sampling region by using a discrete transform. Once a signal is aliased, it can not be recovered. In this case, these high frequencies are "folded over" into the sampled frequency range [45].

We graphically show the effects of aliasing in Figure 25. On the left of the figure, case (a), we show the 1D frequency domain of a signal, whose critical frequency (determined by the sampling in the spatial domain), is $\pm\Omega/2$. Since the frequency domain is completely defined in the range $\{-\Omega/2 \leq \omega \leq \Omega/2\}$, aliasing can be avoided, and the samples can be completely transformed from the spatial to the frequency domain (or vise-versa) with no error by satisfying the sampling theorem. However, on the right side of Figure 25(b), aliasing occurs. Again we show a 1D frequency domain of a signal, however, in this case, the signal contains frequencies that are outside of the critical or largest sampled frequency. In this case these frequencies outside the sampled window

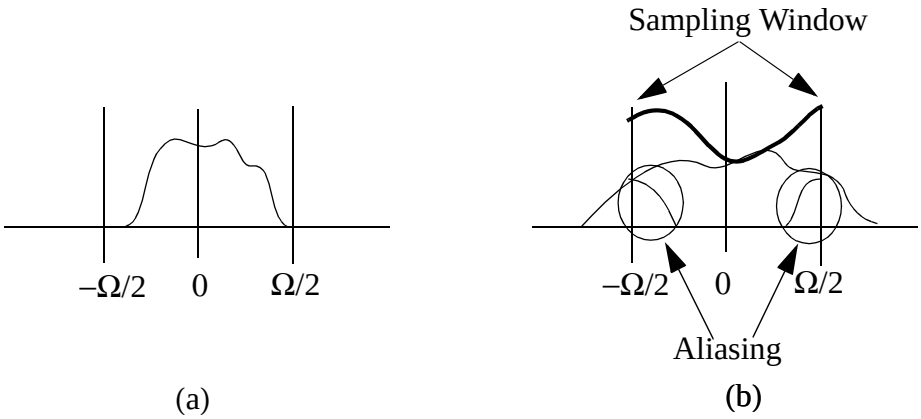

Figure 25 Aliased Frequency Effects

are aliased into the frequency range. Graphically, this is seen as the aliased frequencies being folded back from the edges of the sampled window into the sampled frequency range, as seen in Figure 25(b). The net effect of this aliasing, is the summation of the frequencies in the sampled range and the aliased frequencies. Therefore, the aliased frequency signal is represented by the bold line.

A common technique to avoid aliasing is to ensure that the frequency domains' sampling area or computation window is large enough such that all the frequencies from the Fourier transform are within the sampled range. As can be recalled from Figure 22(c), to double the size of the frequency region, it is required to half the spatial sampling, Δx, by doubling N, while keeping the spatial window *A* constant. We will find throughout this chapter that the technique of doubling N is a common fix to most errors in the discrete Fourier transforms.

4.2.3 Truncation in the Spatial Domain

Truncation is a similar and related error to aliasing that is commonly seen when the signal is transformed back from the frequency domain to the spatial domain. However, in this case, the frequency domain now defines the size of the window in the spatial domain through the inverse Fourier transform. This transforms the spatial frequencies into a spatial wavefront, and, as seen in aliased frequency signals, the corresponding spatial transform can be outside of the defined spatial window. This error is called truncation. In this case, the spatial waveforms are folded into the spatial window, causing errors as the spatial signal is summed with the truncated waveforms.

An example of truncation is seen in Figure 26. Showing the similarity between aliasing and truncation, this graphic is a copy of Figure 25, however, now both waveforms are shown in the

spatial domain. The explanation for both cases, (a) and (b), is analogous to the aliasing discussion. In the first case, Figure 26(a), the spatial window is large enough to support the entire wavefront, therefore no truncation occurs. However, in the second case, Figure 26(b), the spatial wavefront is being “clipped” by the spatial window, and truncation occurs, as the wavefront outside of the window is folded back into the spatial domain. The truncated signal is shown as the bold line. From a graphical example like this, the term “windowing”, an analogous term for truncation, gets it name.

Since the spatial window size is defined at the beginning of the angular spectrum forward-inverse Fourier transfer pair (also referred to as the DFT-IDFT pair), truncation can be avoided by ensuring that the initial spatial window is large enough to support the entire input optical wavefront. This initial spatial domain must also be large enough to support the output spatial domain that is converted from the inverse transform after the optical wavefront has propagated from the aperture plane to the observation plane. If the initial spatial window is not large enough to support the entire propagated beam, truncation will occur.

However, when increasing the spatial window to avoid truncation, it is important to realize the effect this has on the frequency domain. Recalling the reciprocity relations between the spatial and frequency domains, an increase in the spatial window causes the frequency domain to decrease. Therefore, it is common for aliasing errors to arise in the forward Fourier transform

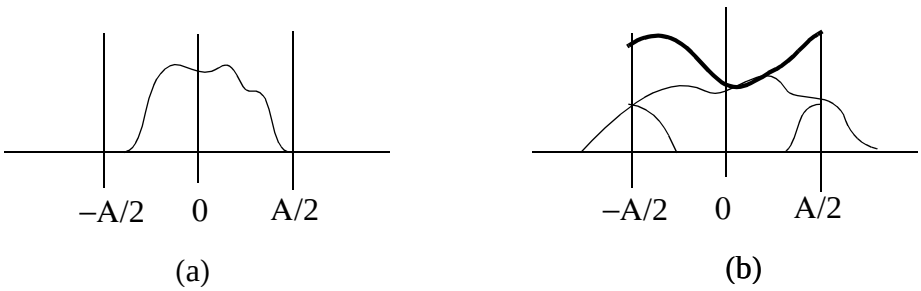

Figure 26 Spatial Truncation Effects

when trying to avoid truncation in the inverse Fourier transform. To avoid this case, when increasing the spatial window size *A*, the value of N should also increase to keep Δx constant at $1/2f_c$.

To minimize both truncation and aliasing errors, it is common to pad the original wavefunction with zeros. From our earlier discussion of increasing *A* with the same number of samples, N, results in the more refined, but smaller, frequency spectrum. As long as the frequency sampling domain is large enough to contain all the frequencies, and the sampling theorem applies, aliasing will not occur. However, if the resulting waveform in the spatial domain after the inverse transform is not spatially limited and there are "ripples" in the waveform, it should be noted that this is a common sign that aliasing and/or truncation has occurred. In this case, the sampling parameters (Δx, A, and N) will have to be rethought and the system re-simulated.

4.2.4 Averaging at Endpoints

Errors also can be caused in the DFT at the endpoints of the function to be transformed. When using the FFT algorithm, one data value contains the value for both spatial frequencies at the endpoints $\pm\frac{1}{2\Delta x}$ (42). If the function has discontinuities at the endpoints, the endpoints must be averaged and these values used for the endpoints, or the DFT is subject to errors. Common optical signals are spatially limited, where their endpoints are essentially zero, as will be described in the next section. In this case, no averaging of the endpoints needs to occur. Therefore, the errors caused by discontinuous end points are not common when using the DFT to propagate a complex optical function through free-space. Since this is the case, we do not go further into the details of

the averaging of end points in this analysis.

4.3 Optical Wavefront and the DFT

To better understand the errors that we expect to have in performing the DFT specifically for the angular spectrum optical propagation method, we analyze the complex optical wavefront which is being propagated from the aperture to the observation plane. The complex optical wavefront is not typically bandlimited, and the period of the function across a 2D surface is not easy to define, if one is even present. Therefore using the Shannon Sampling Theorem is not always applicable for the case of optical propagation. However, further investigations of the characteristics of the optical wavefront lead to a sampling rate which provides good accuracy. We now examine these concepts.

Typically, the optical waveforms propagating in micro-optical systems are compactly supported, which is also known as spatially limited functions. This is an important assumption that we will use throughout this discussion of errors in the angular spectrum method. These functions have the property that

$$f(x) \cong 0 \text{ for } |x| > \frac{A}{2}.$$

If the optical wavefront is not spatially limited in the computation window, a common technique is to increase the window size until the wavefront is spatially limited, with the caveat that N might also need to be increased to minimize aliasing.

Since compactly supported optical wavefronts are important in our error evaluation, we define some characteristics of these functions. Although the function is not periodic, when sampled on the interval of support ($|x| > \frac{A}{2}$), and since it is assumed zero outside of that interval, it is as if a periodic signal has been sampled, and periodic Fourier characteristics apply [45].

On the other hand, if a function is spatially limited, the function is not bandlimited in the frequency domain. Since this is the case for the optical function, aliasing is expected to occur. However, if the modulus, or magnitude, of the spatial frequencies are essentially bandlimited in the frequency domain, the Shannon's sampling theorem can still apply, with only small errors. To the advantage of the angular spectrum technique, this is true for many optical signals. We examine this concept a little further by investigating two optical functions commonly seen in optical micro-systems. The first is the Gaussian beam, and the second is an optical wavefront that is clipped by an aperture.

4.3.1 Example: Gaussian Beam

We first examine a Gaussian beam in the spatial and frequency domains as the Gaussian beam is a common wavefront in optical micro-systems. The Gaussian beam is defined spatially by:

$$U(x, y) = \exp\left(\frac{-(x^2 + y^2)}{w^2}\right),$$

where w is the waist radius measured where the intensity of the beam reaches I_{max}/e^2. Recall that the intensity $I(x,y) = |U(x,y)|^2$.

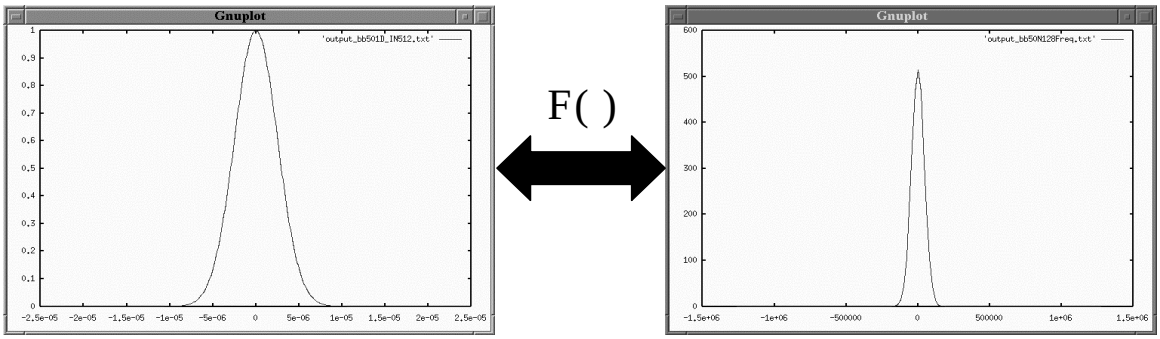

(a) Spatial Domain (in m) (b) Frequency Domain

Figure 27 Gaussian Beam and its Fourier Transform

Mathematically, the 1D Fourier transform of the Gaussian beam is:

$$F\{U(x)\} = (\pi w^2)^{\frac{1}{2}} \exp(-\pi^2 (v_x^2) w^2)$$

Therefore, the Fourier transform of a Gaussian beam in the spatial domain is, in fact, a Gaussian beam in the frequency domain [(49)]. In the special case of the Gaussian beam, we consider both the spatial domain and the frequency domain to be limited, by assuming that the tails of the Gaussian beam die out and approach zero establishing compact limited signals in both domains. With this assumption in the frequency domain, the function appears bandlimited and the sampling theorem can be used to reduce aliasing. Since the function is only "essentially" bandlimited, that is, the spatial frequencies are approximately zero outside the largest sampling frequent, slight aliasing errors are expected to occur.

A 1D cross-section of a Gaussian beam (w=5 μm, λ= 1 μm) and its Fourier transform are shown in Figure 27. In the spatial domain, a spatial bounding box of 50x50 μm, with N=128 is used, as seen in Figure 27(a). This transforms to a frequency bounding box of 2,560,000, seen in Figure 27(b). Notice how the Gaussian function in both domains are compactly limited. Since

the frequency domain is limited by a frequency of approximately $\pm$500000, a required minimum sampling could be established by that sampling theorem of:

$$\Delta x \leq \frac{1}{2f_c} = \frac{1}{2(500{,}000)} = 1.0\mu m$$

Therefore, for accurate sampling of this Gaussian function, a sample size of less than 1.0 μm is required. If the initial guess of the sampling size in the spatial domain did not support an essentially bandlimited function, the Fourier transform would be recalculated with a larger window size in the spatial domain. A full error analysis, including aliasing, truncation, and the calculation of the error is presented later in this chapter.

We now examine another spatially limited function that is common in optical micro-systems, a wavefront that passes through an aperture.

4.3.2 Example: Propagation Through an Aperture

In the case when an optical wavefront passes through an aperture, the function is spatially limited. In this case, the aperture clips the size of the optical wavefront to its physical dimensions. The optical wavefront is now piece-wise continuous and is defined at the aperture by:

$$f(x,y)_{\text{clipped}} = \begin{cases} f(x,y) & \text{for x,y inside of aperture} \\ 0 & \text{for x,y outside of aperture} \end{cases}$$

This clipped function is similar to that of a rectangular function, which is zero outside of some value |x|, and is one inside of |x|. To estimate the Fourier transform of the clipped function, we examine the Fourier transform of the rectangular function. The Fourier transform of the rectangular function is the decaying sinc(x,y). The sinc(x) in 1D is defined by:

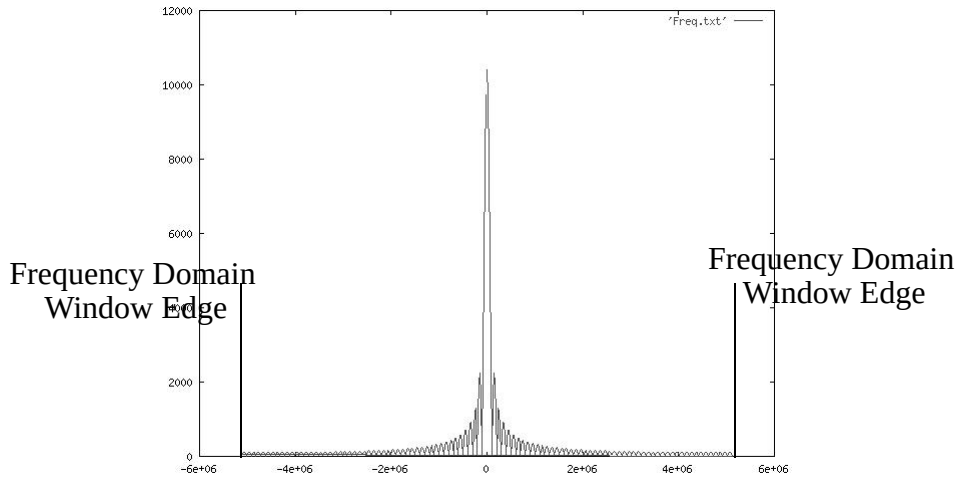

Figure 28 Fourier Transform of Wavefront Propagating Through a Square Aperture

$$\text{sinc}(x) = \frac{\sin(\pi x)}{\pi x}$$

We simulate a incident plane wave (λ=1 μm) propagating through a 10x10 μm square aperture to show the frequency response of performing the Fourier transform. The spatial computation window is 50x50 μm. After the forward Fourier transform is performed, the magnitude of the complex spatial frequencies in the frequency domain are shown in Figure 28. It can be seen, that even though the |sinc(x,y)| function is dying out in the frequency domain, this function is not bandlimited. However, the function is close to zero at the endpoints, therefore, we can assume it is bandlimited, and apply the sampling theorem to give us an idea of the minimum sampling. With this assumption, we expect that the signal will be aliased and slight errors to occur. A common technique to reduce the aliasing errors is to increase the size of the frequency domain, until the tails of the frequency signal are even closer to zero, making our bandlimited assumption stronger.

Now that we have defined typical optical wavefronts in microsystems to be spatially limited and essentially bandlimited, allowing the use of the sampling theorem to reduce aliasing, we dis-

cuss the sampling required for a general optical wavefront.

4.4 General Sampling for the Angular Spectrum Method

In this section, we examine sampling requirements that are specific to the angular spectrum technique to reduce aliasing and truncation errors. As we have throughout this thesis, we discuss the sampling in terms of the spatial frequencies, recalling that the angular frequencies are simply calculated by dividing the spatial frequencies by the wavelength of the optical wavefront. We analyze each of the three portions of the angular spectrum method, the forward DFT, the propagation term, and the inverse DFT, to determine the sampling and window size required for each section to minimize the errors in using the Discrete Fourier transform in the angular spectrum method. For each method, we will determine the minimum sampling, Δx. From these minimum sampling values, the minimum value of Δx will be used to describe the general sampling rule for the complete angular spectrum method.

4.4.1 Sampling of 2D Forward Fourier Transform

As we have already discussed, when taking the forward Fourier transform, the complex wavefront is decomposed into spatial frequencies which can be represented as plane waves, each with a weight, or magnitude, and a direction. In this discussion we analyze the required sampling of the decomposition of the complex wavefront at the aperture plane using the Fourier transform.

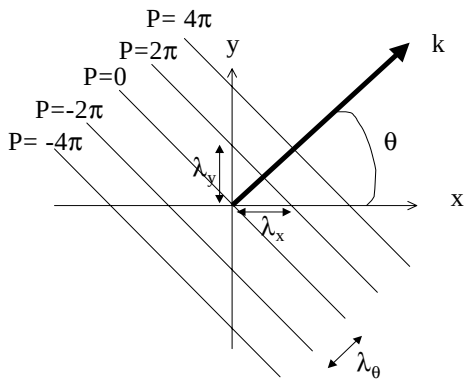

Figure 29 Constant Phase Lines Across Aperture Plane for any Given (v_x=1/λ_x, v_y=1/λ_y) Pair

Recall the Fourier transform on an optical wavefront:

$$U(x, y, 0) = \iint A(v_x, v_y, 0)\exp[-j2\pi(v_x x + v_y y)]\partial v_x \partial v_y$$

From this equation, the plane waves decomposed from the complex 2D optical wavefront U(x,y) are characterized by the function:

$$\exp[-j(v_x x + v_y y)],$$

where v_x and v_y are the spatial frequencies corresponding to the specific plane wave.

Each propagating plane wave, or spatial frequency pair (v_x, v_y), has a zero phase, or a phase with an integer multiple of 2π across the aperture x,y plane. Lines of equal phase (i.e., 2π) can be drawn on the x,y aperture plane, as illustrated in Figure 29. The constant phase lines can be described as:

$v_x x + v_y y = P$, where P is a constant common phase. This equation, in terms of the slope of the lines is rewritten as:

$$y = -\frac{v_x}{v_y}x + \frac{P}{v_y}$$

Therefore, the slope of these lines is $-v_x/v_y$, or as seen in Figure 29, λ_y/λ_x, introducing the relation $v=1/\lambda$. The y intercepts of the constant phase lines equal $A/v_y=A\lambda_y/2\pi$, at constant phase points along the x,y wave front at the aperture plane.

The angle between the normal of the constant phase lines, graphically illustrated as *k* in Figure 29, and the x axis is defined by the perceived wavelengths and the spatial frequencies:

$$\theta_k = \operatorname{atan}\left(\frac{\lambda_x}{\lambda_y}\right) = \operatorname{atan}\left(\frac{v_y}{v_x}\right)$$

The normal *k* has a magnitude of $2\pi/\lambda$.

The spatial period or the spatial wavelength, λ_θ, is defined by:

$$\lambda_\theta = \frac{1}{\sqrt{\frac{1}{\lambda_x^2}+\frac{1}{\lambda_y^2}}} = \frac{1}{\sqrt{v_x^2+v_x^2}}$$

This leads to the spatial frequency of k:

$$k = \sqrt{v_x^2+v_x^2}$$

To ensure that no aliasing occurs during the forward FFT, we use the Shannon sampling theorem, as the optical wavefronts of interest to us are essentially bandlimited signals, as we discussed previously. The spacing in the spatial domain depends on the maximum spatial frequency as seen in:

$$\Delta x, \Delta y \le \frac{1}{2v} = \frac{1}{2v_x\big|_{max}, 2v_y\big|_{max}}.$$

In our angular spectrum method, we are only interested in propagating an optical wavefront in a half sphere toward the observation plane, that is, there is no backward wave propagation. In other words, the maximum spatial frequencies can be determined from the plane waves, which are

decomposed from the Fourier transform. Since we are only concerned with the waves propagating in the half circle, the plane waves propagating in the x and y axes ($\pm$90 degrees, or $\pm\lambda/2$ radians) define the maximum spatial frequencies. Since the wavelength relates the spatial frequencies to the angular frequencies by:

$$v_x = \frac{\sin\theta_x}{\lambda} = \frac{\sin\left(\frac{\lambda}{2}\right)}{\lambda} = \frac{1}{\lambda} \qquad v_y = \frac{\sin\theta_y}{\lambda} = \frac{\sin\left(\frac{\lambda}{2}\right)}{\lambda} = \frac{1}{\lambda},$$

Therefore, with respect to the sampling theorem, the minimum spacing in the spatial domain is:

$$\Delta x = \Delta y \leq \frac{1}{2v_{max}} = \frac{\lambda}{2}$$

In summary, with the assumptions that the optical wavefront is essentially bandlimited and we are only propagating in a half-circle, the following can be followed as a way to ensure that aliasing does not occur: Find two adjacent phase lines, as we presented above. The maximum distance in either the Δx and Δy directions between the phase lines will determine the sampling. In the case that we just presented, this distance was equal to λ. According to the sampling theorem, the complex waveform will have to be sampled at one-half this distance in each direction.

We now move to the propagation of the plane waves, and see what type of sampling constraints there are on this part of the angular spectrum method.

4.4.2 Free-Space Transfer Function: Plane Wave Propagation

To find the sampling requirements of the free-space transfer function, we must carefully examine the plane waves that propagate from the aperture plane to the observation plane. As we

previously discussed in Chapter 3, the direction of the plane waves as they propagate from the origin of the coordinate system is dependant on the spatial frequencies and how these relate to the angular frequencies. We now expand on that discussion.

The plane waves that propagate from aperture to observation plane are characterized by the function:

$\exp[-i(v_x x + v_y y + v_z z)]$, where v_x and v_y are the spatial frequencies in a 2D plane, and v_z is defined as the spatial frequency in the direction of the propagation. The phasor representation of the plane waves can be described as:

$P(x, y, z) = \exp(j(\vec{k} \cdot \vec{r})) = e^{j\frac{2\pi}{\lambda}(\alpha x + \beta y)} e^{j\frac{2\pi}{\lambda}\gamma z}$, where k is the wave function and has a magnitude of $2\pi/\lambda$.

α, β, γ are the directional cosines as seen previously in Chapter 3, and the spatial frequencies are defined from these directional cosines as:

$$\alpha = \lambda v_x \qquad \beta = \lambda v_y \qquad \gamma = \sqrt{1 - \alpha^2 - \beta^2}$$

In Figure 30, a propagating plane wave is shown in the x-z direction. Similar to the waves in the aperture plane, each of the plane wave lines are shown at lines of constant phase. Also seen in Figure 30, is the direction vector, *k*, of the plane wave which has a magnitude of $2\pi/\lambda$, and in the case of the 3D optical propagation of a plane wave,

$$k = 2\pi / \left(\sqrt{\lambda_x^2 + \lambda_y^2 + \lambda_z^2}\right).$$

Recall, the free-space propagation transfer function is simply the phase term:

$$H(v_x, v_y) = \exp\left(-jz2\pi\sqrt{\frac{1}{\lambda^2} - v_x^2 - v_y^2}\right).$$

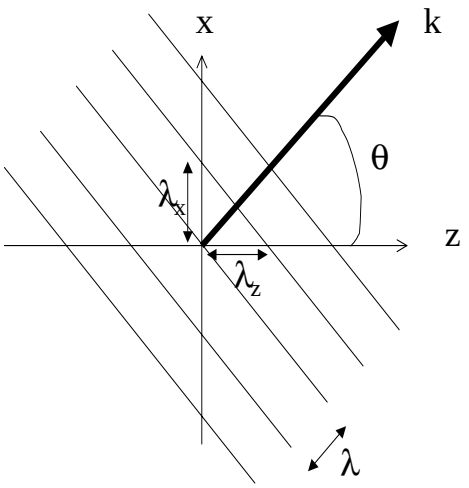

Figure 30 Constant Phase Propagation Lines between Aperture and Observation Planes

This function is a circularly symmetric complex function of the spatial frequencies, with magnitude and phase shown in Figure 31 [13]. By examining the free-space transfer function, for the frequencies lying inside of the circle:

$$v_x^2 + v_y^2 \leq \frac{1}{\lambda^2}$$

the magnitude of $|H(v_x, v_y)|$ =1 and the phase of H is defined by function of the spatial frequencies. For spatial frequencies outside of the circle, the propagating plane wave are evanes-

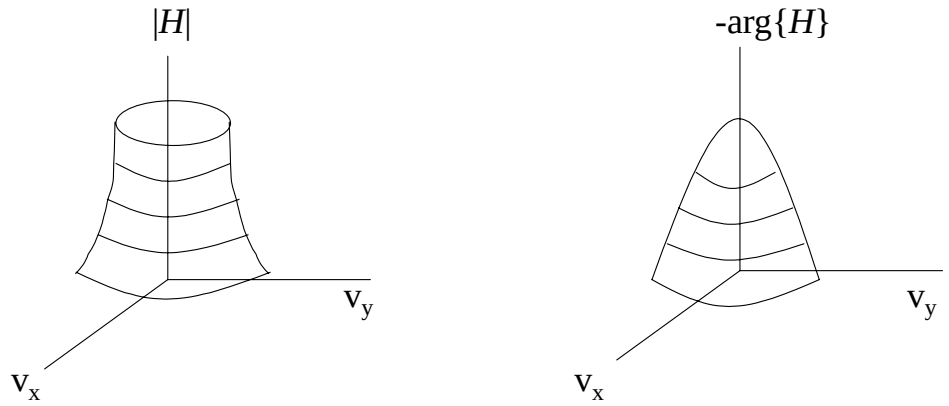

Figure 31 Magnitude and Phase of Free-Space Propagation Transfer Function

cent, and the transfer function represents an attenuation factor. As stated earlier, in this case, we ignore these waves, and set their spatial values to zero, which results in a bandlimited signal in the frequency domain. Therefore, during free-space propagation, $1/\lambda$ is the cutoff (or maximum) spatial frequency of the system making the spatial bandwidth of the propagating wavefront $1/\lambda$ cycles.

Using the sampling theorem, since the complex optical wave is now bandlimited, we can find that the sampling required to remove aliasing is:

$$\Delta x = \Delta y \leq \frac{1}{2f_{max}} = \frac{\lambda}{2}$$

We now evaluate the inverse Fourier transform with regards to the angular spectrum method and the minimization of errors.

4.4.3 2D Inverse Fourier Transform Sampling

During the inverse Fourier transform, a summation of all the propagating plane waves occurs, as the signal in the frequency domain is transformed back into the spatial domain. The sampling requirements of the inverse transform are similar to the sampling requirements of the forward Fourier transform. However, the difference in this case is that the signal is now bandlimited, since the evanescent waves are removed in our algorithm before the inverse Fourier transform is performed, as explained in the last section. Since the signal is bandlimited, the sampling theorem can be used, if the critical frequency can be determined. However, since the angular spectrum use the DFT-IDFT pair, the initial specifications of the forward DFT determine the size of the frequency domain, and this size defines the output of the observation spatial domain. Therefore, as long as

the original complex value is sampled correctly, then the IDFT can reconstruct the bandlimited signal exactly. However, truncation errors are common when propagating optical wavefronts and can still occur even with proper sampling, therefore the transformed signal from the inverse Fourier transform will have to be examined for truncation.

4.4.4 Summary of Sampling the Angular Spectrum Technique

We summarize the required sampling to avoid aliasing in the angular spectrum method in the following table.

Table 11 Sampling for the Angular Spectrum Method to Avoid Aliasing

	Required Δx *Sampling*
Forward DFT	$\frac{\lambda}{2}$
Propagation	$\frac{\lambda}{2}$
Inverse DFT	$\geq \frac{\lambda}{2}$

Since the angular spectrum is a DFT-IDFT pair, the initial sampling size and computation window defines both the spatial and frequency domain for the entire simulation even before the first Fourier transform is performed. Therefore the smallest required sampling size of the entire angular spectrum technique should be chosen to avoid aliasing in the system. Therefore, the sampling of the system is defined to be the same for both the forward DFT and the propagation distance and

we will use this minimum sampling size in our simulations:

$$\Delta x = \Delta y = \frac{\lambda}{2}.$$

There are two important notes regarding sampling in the angular spectrum technique. The first is that these are the minimum values to minimize aliasing with the assumptions that we made that the optical signal can be considered limited in both the spatial and frequency domain. We have found in practice, that these values typically do not have to be this small for accurate results with negligible error. The second, and most important note, is the assumption that the optical wavefront can be considered a compact bandlimited function. This allowed us to use the sampling theorem to make our sampling conditions. Recall, even using the specified sampling, with these assumptions, aliasing will occur, leading to errors in the result. Therefore, in summary, we suggest the designer use the above minimum sampling for a general rule of thumb for the discretization of the optical function. However, since the calculation of the error is also of interest, we next describe a method for determining these errors when using the angular spectrum technique.

4.5 Error Estimates of the DFT

In the previous section, we presented minimum sampling requirements to reduce aliasing in the angular spectrum technique. These were based on the assumptions that the complex optical signal is both bandlimited and spatially limited. With these assumptions, slight errors do occur. In this section, we begin a point-wise error bound analysis of this technique to estimate these errors in the angular spectrum technique. These errors are based on aliasing, truncation, and the fact that we are using a discrete integration technique to approximate a continuous integration.

We break this section into the error analysis of the forward DFT and the inverse DFT.

4.5.1 Forward DFT

We have seen in our previous discussions in this chapter that the complex optical wavefunctions are essentially spatially limited and bandlimited functions, and aliasing will occur. Before we start our mathematical approach to determining the point-wise error bounds found in the angular spectrum method, it is important to examine and understand the *Replication* of a complex signal and also the *Poisson Summation Formula* [45]. These two formula provide a method for determining the errors of using the DFT for the angular spectrum technique for optical propagation.

The replication is the superposition, or summation, of copies of the complex optical function, *f*, each displaced by multiples of a period, A. The replication of period A for the complex optical function, *f*, is shown in the spatial domain, resulting in a new complex function:

$$\Re_A\{f(x)\} = \sum_{j=-\infty}^{\infty} f(x + jA)$$

The replication can also be seen with a discrete sequence, such as the Fourier series coefficients, c_n:

$$\Re_N\{c_n\} = \sum_{k=-\infty}^{\infty} c_n + kN$$

The replication function can also be used in the frequency domain, as a replicated Fourier transform, $\hat{g}$, is calculated by a summation of the Fourier transform of *f*, denoted by $\hat{f}$, each

shifted by a period of $\Omega=1/\Delta x$. This can be seen in the equation:

$$\hat{g}(\omega) \equiv \Re_{\Omega}\{\hat{f}(\omega)\} = \sum_{j=-\infty}^{\infty} \hat{f}\left(\omega - \frac{j}{\Delta x}\right).$$

Since $\hat{g}$ is now a periodic function, it has a discrete Fourier Series of:

$$\hat{g}(\omega) = \sum_{n=-\infty}^{\infty} c_n e^{j2\pi n\Delta x\omega}$$

Determining the Fourier coefficients for c_n is seen through the standard Fourier transform:

$$c_n = \Delta x \int_{\frac{-1}{2\Delta x}}^{\frac{1}{2\Delta x}} \hat{g}(\omega) e^{j2\pi n\Delta x\omega} d\omega = \Delta x \int_{\frac{-1}{2\Delta x}}^{\frac{1}{2\Delta x}} \left(\sum_{j=-\infty}^{\infty} \hat{f}\left(\omega - \frac{j}{\Delta x}\right) \right) e^{j2\pi n\Delta x\omega} d\omega .$$

With the substitution $x_n=n\Delta x$, and the limits of the summation overriding the limits of the integration, the replication equation becomes:

$$c_n = \Delta x \int_{-\infty}^{\infty} \hat{f}(\omega) e^{j2\pi x_n\omega} d\omega = \Delta x f(x_{-n}) .$$

Now, substituting back into previous equations, the Fourier transform of the Replication $\hat{g}$ is verified:

$$\hat{g}(\omega) = \Delta x \sum_{n=-\infty}^{\infty} f(x_{-n}) e^{j2\pi x_n\omega} = \Delta x \sum_{n=-\infty}^{\infty} f(x_n) e^{-j2\pi x_n\omega} = \sum_{j=-\infty}^{\infty} \hat{f}\left(\omega - \frac{j}{\Delta x}\right)$$

We now introduce the Poisson Summation Formulation [45], which states: If function f is defined for $-\infty < x < \infty$, its Fourier transform is defined for $-\infty < \omega < \infty$, and its sample points are given by $x_n = n\Delta x$ for $-\infty < n < \infty$, then

$$\Delta x \sum_{j=-\infty}^{\infty} f(x_n) e^{-j2\pi x_n \omega} = \sum_{j=-\infty}^{\infty} \hat{f}\left(\omega - \frac{j}{\Delta x}\right)$$

With ω set to 0, the above is equal to:

$$\Delta x \sum_{j=-\infty}^{\infty} f(x_n) = \sum_{j=-\infty}^{\infty} \hat{f}\left(\frac{j}{\Delta x}\right)$$

This states that the sum of the samples of *f* is a constant times the sum of the Fourier transform of *f* at multiples of the cut-off frequency.

Putting the Replication, DFT, and the Poisson Summation Formulas together, the following is obtained [45]:

$$AD\{\Re_N\{f_n\}\}_k = \Re_N\{\hat{f}_k\},$$

where *D* is the DFT operator.

This is an important fact, since we have shown that the N point DFT of the sampled replication of *f* is the sampled replication of the Fourier transform of *f*.

In optical signals with compact support, replication of the period N does not change the function f_n. Therefore, the Poisson Summation Formula looks like:

$$AF_k = \Re_N\{\hat{f}_k\} = \hat{g}(\omega_k)$$

To evaluate the error of using the DFT to represent the continuous Fourier transform, we start by examining the difference between the Fourier transform using a DFT (AF_k) and the continuous Fourier transform, as seen in:

$$\left|AF_k - \hat{f}(\omega_k)\right| = \left|AF_k - \hat{g}(\omega_k) + \hat{g}(\omega_k) - \hat{f}(\omega_k)\right|$$

which can be rewritten as:

$$\left|AF_k - \hat{f}(\omega_k)\right| = \left|AF_k - \hat{g}(\omega_k)\right| + \left|\hat{g}(\omega_k) - \hat{f}(\omega_k)\right|$$

This reduction is interesting as the first absolute value term is equal to the Poisson Summation Formula, and is equal to zero. The second term is the error that is due to sampling. This is simply the difference between the Fourier transform of the function *f* and the Fourier transform of the function *f*'s replication, denoted as $\hat{g}$. Therefore the error in the forward Fourier transform is:

$$\left|AF_k - \hat{f}(\omega_k)\right| = \left|\hat{g}(\omega_k) - \hat{f}(\omega_k)\right|$$

If *f(x)* is a spatially limited function and the periodic extension of *f* has (p-1) continuous derivatives for $p \geq 1$ and that f^p is bounded and piece-wise monotone on the sampling range[-A/2,A/2], the error in the DFT is:

$$\left|AF_k - \hat{f}(\omega_k)\right| \leq \frac{C}{N^{p+1}}$$

for $k = -\frac{N}{2} + 1 \ldots \frac{N}{2}$,

where, *C* is a constant that is independent of *k* and N

We state a proof next [45] for the error in the forward Fourier transform. With a spatially limited signal, the Poisson Summation Formulation states:

$$\Delta x \sum_{n=-\frac{N}{2}+1}^{\frac{N}{2}} f(x_n) e^{-j2\pi n x_n \omega_k} = \sum_{j=-\infty}^{\infty} \hat{f}\left(\omega_k - \frac{j}{\Delta x}\right),$$

where ω is evaluated at ω_k=k/A.

Reorganizing,

$$\left|AF_k - \hat{f}(\omega_k)\right| \le \sum_{j=1}^{\infty} \left(\left|\hat{f}\left(\omega_k - \frac{j}{\Delta x}\right)\right| + \left|\hat{f}\left(\omega_k + \frac{j}{\Delta x}\right)\right| \right) = \sum_{j=1}^{\infty} \left(\left|\hat{f}(\omega_{k-jN})\right| + \left|\hat{f}(\omega_{k+jN})\right| \right)$$

With the previous substitutions, we can see that:

$$\left|AF_k - \hat{f}(\omega_k)\right| \le \sum_{j=1}^{\infty} \left(\left|c_{k-jN}\right| + \left|c_{k+jN}\right| \right)$$

Now using the Rate of Decay of Fourier Coefficients [45], which states that if *f* and its first *p*-1 derivatives are periodic and continuous on [-A/2, A/2], then the Fourier coefficients of *f* satisfy

$$\left|c_k\right| \le \frac{C}{|k|^{p+1}}$$

for all *k*, and *C* is constant and independent of *k*. Remember that, the replication of a compactly limited optical signal is periodic, therefore, the Rate of Decay of Fourier Coefficients is valid.

Concluding our proof, we can the state the end result:

$$\left|AF_k - \hat{f}(\omega_k)\right| \le \frac{C}{N^{p+1}} \text{ for } k = -\frac{N}{2} + 1 \ldots \frac{N}{2},$$

To draw a conclusion to this error estimate discussion, we must define the constant *C*. *C* is dependant on the convergence of the Fourier coefficients. Even with the popularity of the FFT, Fourier convergence is still a difficult subject to completely define [45]. For this fact, the constant *C* is not well defined, as the authors of many books seem content with the flexibility of an undefined constant [45][50][51]. However, it is our goal to find the order of magnitude of the error in using a DFT to represent the Fourier transform of a signal. In texts, the constant C has been found to be dependant and bounded by the least upper bound of the magnitude of the function to be

transformed [45][51]. This can be written mathematically as:

$$M = \sup_{[-A/2,\, A/2]} |f(x)| ,$$

where the function "sup" stands for supremum, which is the least upper bound of a set, *S*. It is defined to be the smallest real number that is greater than or equal to every number in *S* [52].

The constant C is simply a scaling factor for the magnitude of the initial function, such that the determined error bounds correspond to the input. In this thesis, we analyze normalized functions, therefore, the least upper bound of a function, *f*(x), in the range [-A/2,A/2] will be 1. Therefore, for the functions that we examine, $0 < C \leq 1$. Since we are interested in the bounds of the maximum error for the normalized functions we consider, the largest error will be defined when C=1. Therefore the error bounds of the difference between the DFT approximation and the continuous Fourier transform is dependant on:

$$\left| AF_k - \hat{f}(\omega_k) \right|_{\max} \leq \frac{1}{N^{p+1}}$$

Therefore, we conclude that for our application, the order of the error bound is only dependant on the number of points that are taken and the smoothness of the function that is being transformed. The smoothness of a function is determined by the number of continuous derivatives the function has on the sampling range[-A/2,A/2]. We will look into the determination of *p* later in this chapter.

4.5.2 Inverse DFT

For the inverse DFT, we begin our error discussion with the assumption that we have a function, $\hat{f}$ (or Fourier coefficients, c_k) in the frequency domain. The frequency domain range is

defined as $\{-\Omega/2 \leq \omega \leq \Omega/2, -\Lambda/2 \leq \sigma \leq \Lambda/2\}$, and transforms to the spatial domain $\{-A/2 \leq x \leq A/2, -B/2 \leq y \leq B/2\}$, through the inverse DFT. If the reconstructed function *f* has a finite number of frequencies, that is, all the frequencies can be included in the IDFT, then *f* can be exactly reconstructed, assuming that no frequencies have been aliased. Recall the IDFT:

$$f_n = \sum_{k=-\frac{N}{2}+1}^{\frac{N}{2}} \hat{f}_k \omega_N^{nk} = \sum_{k=-\frac{N}{2}+1}^{\frac{N}{2}} \hat{f}_k e^{j2\pi n\frac{k}{N}}$$

Similar to the forward DFT, we use the Inverse Poisson Summation Formula to help our error analysis. The Inverse Poisson Summation Formula is stated here [45]:

$$\Delta\omega \sum_{k=-\infty}^{\infty} \hat{f}(\omega_k) e^{i2\pi\omega_k x} = \sum_{j=-\infty}^{\infty} f(x - jA)$$

In the case of the inverse Poisson Summation Formula, samples in the Fourier Domain, $\hat{f}$, are related to the replication of the signal *f*. For a bandlimited, the error in using the IDFT involves the values of *f* transformed outside the interval [-A/2, A/2]. Recall that the spatial window is defined by the sampling of the frequency domain, $\Delta\omega$, therefore this choice of sampling is critical. If the function *f* is reconstructed outside of the range [-A/2, A/2], then those parts outside of the range are folded back into the sampled range, as seen in the truncation error presented earlier. We previously reduced this error by increasing N with Ω fixed (i.e., reducing $\Delta\omega$), which increases the spatial boundary A, therefore, reducing the overlap in the replicated values of *f*(x-jA). From this overlap of replicated values, we approximate the error bound:

$$\left|\Delta\omega\tilde{f}_n - f(x_n)\right| \leq \sum_{|j| \geq 1}^{\infty} f(x_n - jA)$$

The error of the inverse DFT, based on the overlap of the replications of the function is more difficult and not as straight forward to calculate as the error in the forward transform. However, since the initial spatial domain (aperture plane) defines both the frequency domain and the output spatial domain (observation plane), we make the argument that the error in using the discrete Fourier transform to approximate the continuous Fourier transform should be on the same order. The error that remains in the inverse DFT should be based on truncation. With the removal of the evanescent waves in the angular spectrum technique, the frequency function is bandlimited and with proper sampling, the error in the inverse DFT is negligible.

We now summarize the point-by-point errors bounds that were determined in the forward and inverse Fourier transformations in terms of the angular spectrum method.

4.5.3 Summary: Point-Wise Errors of Angular Spectrum Method

For the general case, we can determine how much error is in our simulations, by using the point-wise error equations for the forward and the inverse Fourier transform that we presented in this chapter. It should be noted, that the error calculation will add computation time to the angular spectrum method, possibly eliminating the interactive response between the simulation tool and the designer. Before starting the simulation, the user should first reduce aliasing and truncation, by using the sampling guidelines presented earlier in this chapter. As previously determined, the minimum sampling in both the x and y directions should be initially set at $\lambda/2$. To calculate the error in any wavefront propagating from the aperture to the observation plane, we follow with steps of the angular spectrum technique, determining the error at each point along the path, shown through the flowchart in Figure 32. We explain the details next.

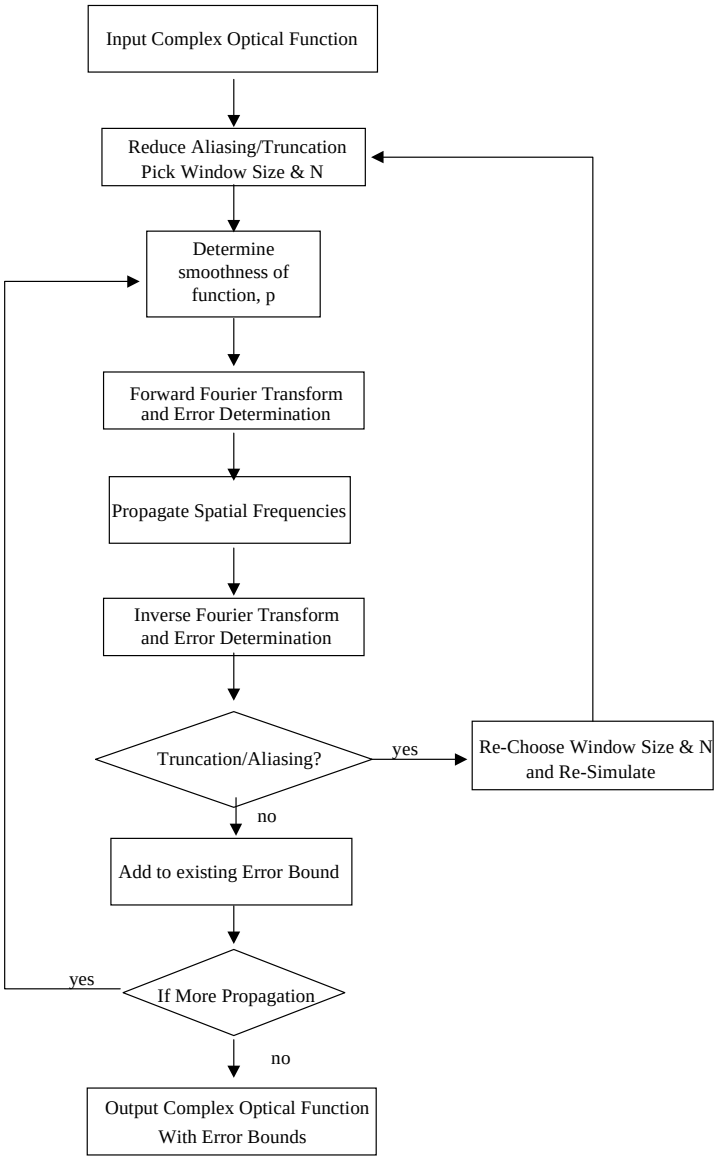

Figure 32 Angular Spectrum Algorithm with Error Determination

After setting the initial sampling to reduce aliasing and truncation, the smoothness (denoted by the variable *p* in the previous error discussion) of the optical wavefront function must be determined, by calculating the number of continuous and non-zero derivatives in the range of the computational window. The derivative of a function can be performed with a standard numerical algorithm, such as a Newton-Raphson algorithm, found in many numerical methods references such as [(42)]. The derivative can easily be checked for discontinuities, and if the derivative is con-

tinuous, the next derivative of the function can be determined. The process continues, until a derivative is found to be discontinuous, and *p* is determined. Another way of determining the smoothness of a function is to determine the gradient, or directional derivative, of the function. Using this, the rate of change in a specified direction is known. From this, it is possible to determine discontinuities in a function, or in this case, its derivative. Knowing the number of continuous derivatives will provide us with the order of the error of approximating the forward Fourier transform with a discrete Fourier transform ($1/N^{p+1}$). After the forward Fourier transform is implemented, the spatial frequencies are multiplied by the propagation phase term. We then perform the inverse Fourier transform, which returns the optical wavefront to the spatial domain. The error of the inverse DFT, based on the overlap of the replications of the function, has been presented earlier, however, since the signal is bandlimited, and if care has been taken in the original choosing of the window size and the number of discretizations, N, this error should be negligible and the error of the overall angular spectrum method should be on the order of the error from the forward Fourier transform.

With the propagation term typically expanding the optical wavefront, a check for truncation must occur at the conclusion of the angular spectrum technique. This is performed by an examination of the wavefront determining that the tail-ends of the function are decreasing towards zero, and that the ends of the function are essentially zero. Recall, if the wavefront has ripples at the ends of the function, similar to Figure 34, this is a common sign that truncation has occurred and re-simulation with a different window size and N should occur. In the future work of this thesis, we describe how this could be done automatically in the software. To remove truncation, the initial spatial domain (*A* and *B*) needs to be increased, however, the initial sampling requirements still need to be satisfied, therefore, N typically needs to be increased as well.

If this is the first and only free-space propagation gap, the calculated error bound from the forward Fourier transform is the error bound of the system. If this is not the only free-space propagation gap, this value is stored, and the algorithm presented in the flow chart begins again. When the error-bound of this pass through the algorithm is calculated, this error is added to the previous error bound, and the algorithm either ends if there are no more propagation gaps or repeats.

We now present a few examples, summarizing our work in this chapter.

4.6 Example Error Analysis

We now perform an error analysis of the angular spectrum technique using optical wavefronts that are used in micro-optical systems. We first examine the Gaussian beam, starting with an analysis of aliasing and truncation. We then perform a point-by-point comparison between simulated results and analytical data, and compare these results to expected error theory presented in the last section. As a second example, we examine a clipped optical wavefront, and present an error analysis of this system. This section is concluded with an algorithm to perform an error analysis on a general optical wavefront propagating from the aperture plane to the observation plane.

4.6.1 Gaussian Beam

We first examine a Gaussian beam, a common optical input into micro-optical systems, and determine how to reduce aliasing and truncation to a minimum. Since we know that these errors can not be completely eliminated, we also provide a point-wise error analysis of propagating this

beam from an aperture to an observation plane using the DFT to approximate the continuous Fourier transform.

Recall from our earlier discussion, the spatial Gaussian beam equation, in 2D is:

$$U(x, y) = \exp\left(\frac{-(x^2 + y^2)}{w^2}\right),$$

where w is the waist radius.

For illustrative purposes, in the first part of this example, we describe how to reduce aliasing and truncation. Recall, from our earlier sampling conditions of the angular spectrum technique, the spacing in the spatial domain should be $\lambda/2$. However, in this first example, we are going to use a even smaller spacing, to show another way of determining the required spacing.

In this example, we examine a Gaussian beam with a spot size (which equals $2w$) of 10 μm and a wavelength of 1000nm, which is a common source for optical micro-systems. We first examine the beam with a bounding spatial box of A=B=50 μm, with N=512. This results in a Δx and Δy of approximately 0.098 μm. The spatial domain in a 1D cross-section is seen at the top of the column in Figure 33(a). These spatial domain parameters correspond to a frequency domain with $\Omega=\Lambda=10{,}240{,}000$ and a $\Delta\omega$ and $\Delta\sigma$ of 20,000. Moving down the column in Figure 33(a), we present 1D cross-sections of the frequency domain after the forward Fourier transform is performed, and again the spatial domain after the inverse Fourier transform is performed. Note that there is no propagation in these optical wavefronts, as this is simply an example to see if we can recover the exact spatial wavefront that we converted into the frequency domain.

Since the Fourier transform of a spatial Gaussian beam has spatial frequencies in the shape of a Gaussian beam in the frequency domain, we assume both the spatial domain and the frequency domain to be limited. With this bandlimited assumption, the sampling theorem can be used to

reduce aliasing. This is graphically seen in the middle row of Figure 33(a), where the Gaussian beam appears to be essentially bandlimited, as the frequencies outside of approximately $\pm 10^6$ cycles/meter are essentially 0.

Using the bandlimited assumption, the sampling theorem states the spacing in the spatial domain must be:

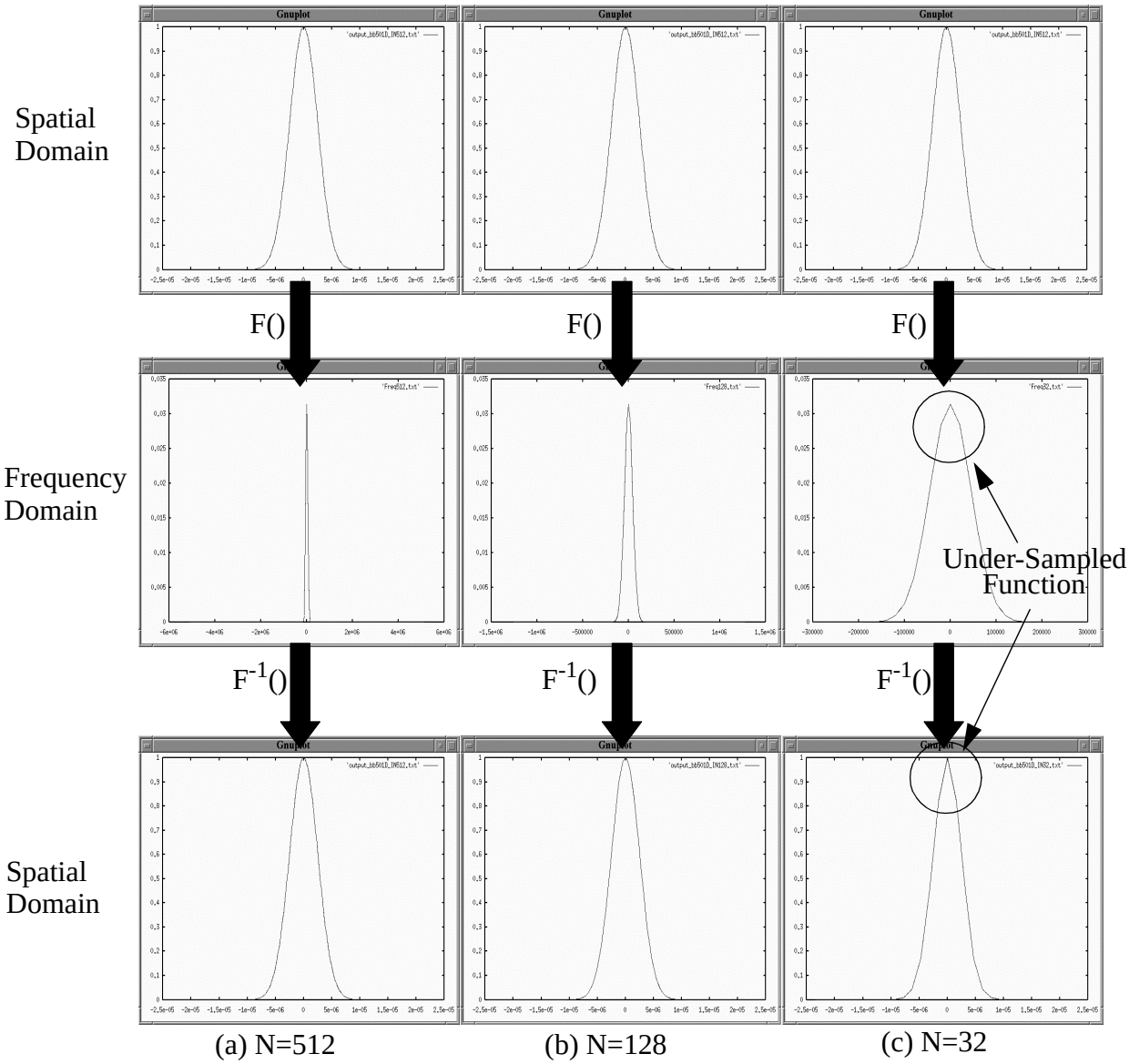

Figure 33 Gaussian Beam Sampling Example

$$\Delta x \leq \frac{1}{2f_c} = \frac{1}{2(1{,}000{,}000)} = 0.5\mu m$$

With our initial guess of N=512 and A=50μm, we have oversampled the complex wave function. Of course, this does not hurt our calculation of the DFT, as we were able to recover the input when the inverse Fourier transform was performed. However, we could achieve the same accuracy without as many sample points, which will decrease the computation time.

Note, that the efficient sampling value that we just calculated ($\Delta x \leq \frac{1}{2f_c} = 0.5\mu m$) equals our anti-aliasing λ/2 rule-of-thumb ($\Delta x \leq \frac{\lambda}{2} = 0.5\mu m$), seen previously in this chapter. Therefore, we should have begun our example with this sampling value, however, we were able to achieve the same results by graphically examining the essentially band-limited signal and determining its critical frequency.

Continuing our example with the same size of A=50μm, we can find the maximum N that is needed to satisfy the Sampling Theorem by using the calculated sampling value and the reciprocity relations that we described earlier:

$$N = \frac{A}{\Delta x} = \frac{50\mu m}{0.5\mu m} = 100$$

Since our DFT algorithm requires N be a factor of 2, we choose to use N=128 points. Therefore we can retain the same accuracy in our simulation, but with increased computation speed of the system simulation by reducing the value of N. In Figure 33(b), we show results from this simulation with the new value of N. By looking at the curves, it can be seen that the input function is recovered in the spatial domain when implementing the inverse Fourier transform.

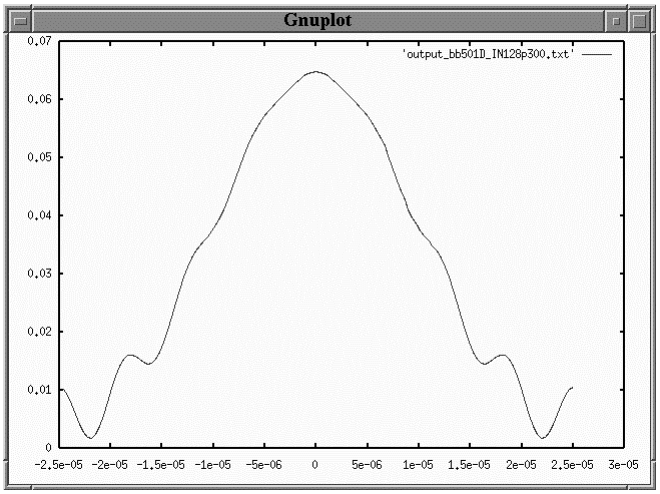

Figure 34 Truncated Gaussian Beam at Observation Plane

For comparison, we show an example of the same Gaussian beam being undersampled, with N=32. This is shown in Figure 33(c). In the example, the input Gaussian function is not reconstructed with the undersampled frequency domain.

Optical propagation with the angular spectrum method is achieved by multiplying a phase function to each set of spatial frequencies, which, as we presented previously, represent plane waves propagating from the aperture to the observation planes. When an optical wavefront propagates, the optical beam can diverge, causing possible truncation at the observation plane. It is common when both the aperture and the observation planes are the same size, that an optical beam that was untruncated in the aperture plane becomes truncated at the observation plane after propagation.

An example of this truncation effect is shown in Figure 34. In this example, the same Gaussian beam that we examined previously in Figure 33(b) has now been propagated 300 μm between the aperture and the observation planes. It can be seen that the observation plane has truncated the spatial output and caused errors, as we know that a propagating Gaussian beam remains Gaussian

in shape. As the spatial domain is being reconstructed from the frequency domain, the complex optical wavefront that is outside the window is folded back into the window, causing the rippling effect of the waveform.

To rectify the truncation problem, the size of the observation spatial window needs to be increased, which can be done by reducing $\Delta\omega$ in the frequency domain. This can be done by reducing the size of the frequency domain (Ω), keeping N constant (or vise versa), and using an interpolation technique to find values for the frequency points that are not determined from the forward Fourier transform. Of course, an interpolation technique would add to the errors found in the angular spectrum technique and add to the system simulation computation time. For these reasons, we do not take this approach.

A simpler way of removing truncation in the observation plane is to make the original aperture plane large enough to capture the propagation divergence in the observation plane. This can be done by increasing the spatial size *A* in the aperture plane, with the caveat that this could introduce an aliasing error, as describe earlier.

Returning to our example, we re-simulate the system with an input spatial window of 100x100 μm, instead of 50x50 μm. With N still equal to 128 mesh points, the input sampling does not cause significant aliasing. We validate this statement by examine the frequency domain, and evaluating the essentially bandlimited function. By calculating the spacing $\Delta x = 100\mu m/128 = 0.78125\ \mu m$, the frequency domain is defined by $\Omega=\Lambda=1{,}280{,}000$ with a $\Delta\omega$ and $\Delta\sigma$ of 10,000. Our rule of thumb rules states that we should have a sampling less than $\lambda/2=0.5\mu m$. In this example, we present a case when our general sampling rule is too conservative.

Examining the frequency response of the propagated beam in Figure 35(a), we find an essentially band limited signal with a critical frequency of approximately 300,000. This leads to a sam-

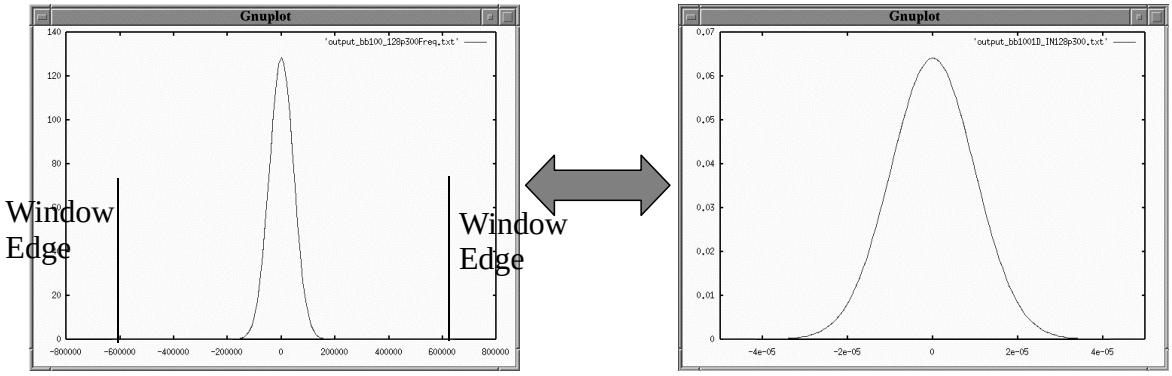

(a) Frequency Domain (b) Spatial Domain

Figure 35 Untruncated Gaussian Beam in Frequency Domain and Observation Plane

pling maximum of

$$\Delta x \leq \frac{1}{2f_c} = \frac{1}{2(300{,}000)} = 1.67\mu m .$$

Our sampling in this example of 0.78125 μm is below this value, therefore we expect the aliasing to be negligible. Therefore, output at the observation plane for the Gaussian beam propagated 300 μm is no longer truncated, and has minimized aliasing. The result is shown in Figure 35(b).

Note that the sampling in this final non-truncation case is greater than our specified anti-aliasing spacing of λ/2 (1.67μm > 0.5μm). This shows how the required sampling of λ/2 is a conservative result and in practice, the sampling can be larger, especially for a smooth function, such as a Gaussian beam.

Using the techniques seen above, we have reduced aliasing and truncation errors. However, we now calculate the order of the remaining error, caused by both aliasing and the fact that we are using a discrete integration technique to approximate a continuous integration with the DFT.

We continue our Gaussian beam example, this time predicting the error at each discretization point. We use the same Gaussian beam as before with a bounding spatial box of A=B=50 μm,

with N=128. This results in a Δx and Δy sampling of approximately 0.5 μm. These spatial inputs correspond to a frequency domain with $\Omega=\Lambda=1{,}000{,}000$ with a $\Delta\omega$ and $\Delta\sigma$ of 7812.5. This is the case that we looked at previously in Figure 33(b).

Recall, the 1D Fourier transform of the Gaussian beam is:

$$F\{U(x,y)\} = (\pi w^2)^{\frac{1}{2}} \exp(-\pi^2(v_x^2)w^2)$$

In our simulations, we are going to use this analytical expression to compare against our simulated results. We can then determine point-wise error measurement of our technique and the analytical results and compare these results with the expected error bounds for this system.

We first review the expected error theory. Since the Gaussian beam is a even exponential function and the first derivative of the function can lead to discontinuities at the end-points in the sampled region, p=1. From this, the point-wise error function is expected [45]:

$$|c_k - F_k| \le \frac{C}{N^{p+1}} = \frac{C}{N^2}.$$

Again, we assume that to find the maximum error, that C is based on the largest bound of the function to be transformed. Since we are transforming a normalized Gaussian beam, with a maximum value of 1, we expect the error to be on the order of $1/N^2$.

We now want to measure the error that is obtained when comparing our simulated results against the analytical solution of the Fourier transform of a Gaussian beam. We compare only in the 1D case, since the Gaussian beam is symmetrical. In Figure 36(a) the 1D normalized frequency domain is presented for the analytical results and our simulated DFT algorithm of performing the forward Fourier transform on the Gaussian beam described above. Notice that this graph is just the positive spatial frequencies. Since the Gaussian function is symmetrical, the neg-

ative frequencies are identical to the positive. From examining the outputs, the results are graphically identical.

We perform a point-by-point difference of the simulation results compared to the analytical results. These are plotted on the log scale, as seen in Figure 36(b). The error analysis states that with N=128, the point-to-point difference should be on the order of $1/N^2 = 10^{-5}$. As can be seen, our results between the simulated and analytical are lower than that, approximately 10^{-8}.

Continuing with the N=128 example, we perform the inverse Fourier transform, and again evaluate the error of the function as it is transformed back from the frequency domain to the spatial domain. In Figure 37(a), we show the normalized the Gaussian beam after a forward and inverse Fourier transform. Figure 37(b) shows the point-wise error difference between the analytical results and our simulation results using the angular spectrum technique. It can seen that again our technique matches well with the analytical results, as we predicted that the error would be on the order of 10^{-5}. Again, our error measurements were less than 10^{-7}. As we mentioned before, and now can be seen graphically, the error difference was not increased by the inverse Fourier

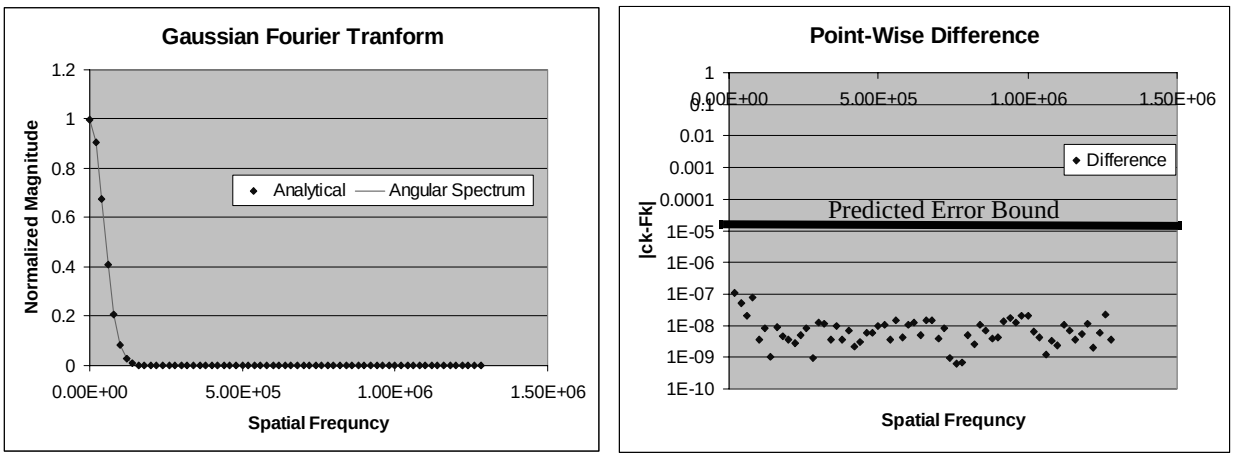

Figure 36 (a) Normalized Intensity Profile After Fourier Transform of Gaussian Beam (b) Point-Wise Error, for N=128

transform.

Our last simulation with this Gaussian beam is the case when it propagates from aperture to observation plane. To avoid the truncation that we presented in Figure 34, we increase the computation window to 100 μm, and we propagate the optical beam 300 μm. Again, we compare this result with analytical results of a propagating Gaussian beam.

We digress just a little to show our analytical determination of a propagating Gaussian beam. A Gaussian beam is defined by its initial waist, w_0, and Rayleigh Range, z_0:

$$z_0 = \frac{\pi w_0^2}{\lambda}$$

As a beam propagates, the Gaussian beam diverges, and a waist can be calculated dependent of the length of propagation. This is described by:

$w(z) = w\sqrt{1 + \left(\frac{z}{z_0}\right)^2}$, where z is the propagation distance.

From this equation, the Gaussian wavefront is defined by:

$$Gauss(x, y, z) = \frac{w_0}{w(z)} \exp\left(-\frac{x^2 + y^2}{w(z)^2}\right).$$

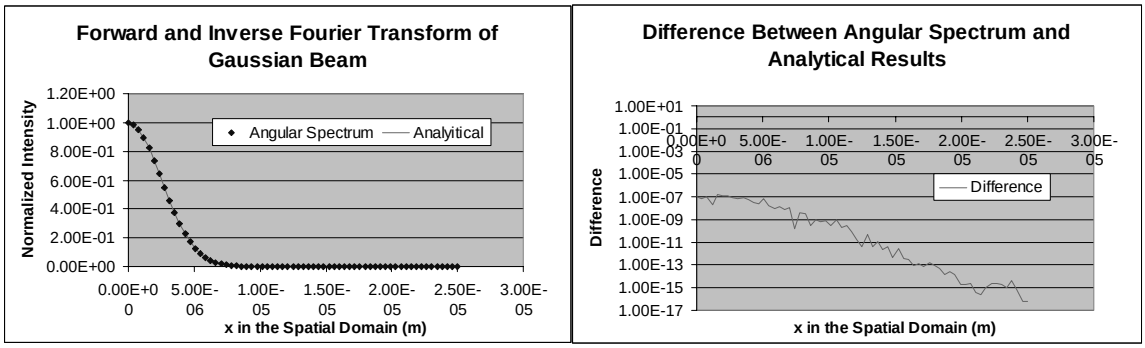

Figure 37 (a) Normalized Intensity Profile After Forward and Inverse Fourier Transform of Gaussian Beam (b) Point-Wise Error, for N=128

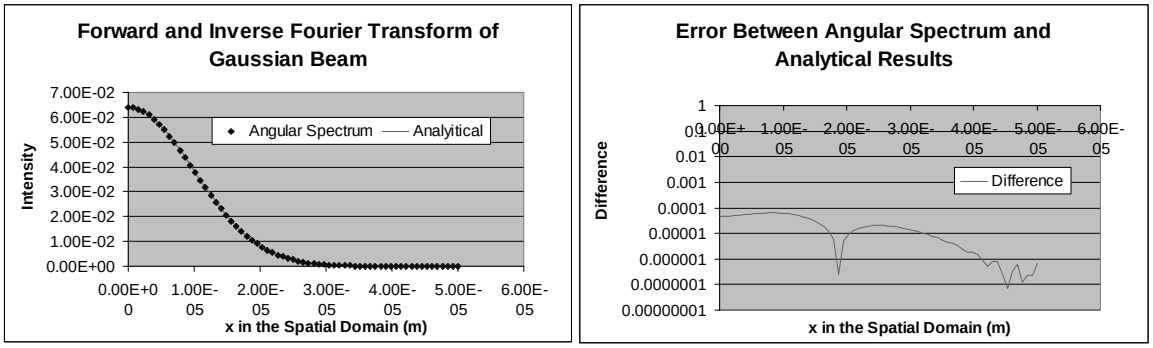

Figure 38 300 μm Propagation of Gaussian Beam (a) Compare with Analytical Results (b) Point-Wise Error, for N=128

The intensity of the Gaussian beam is defined by the square of the magnitude, as seen:

$$I_{Gauss}(x, y, z) = \left| \frac{w_0}{w(z)} \exp\left(-\frac{x^2 + y^2}{w(z)^2} \right) \right|^2 .$$

A graph comparing our simulated results with the analytical results are seen in Figure 38(a), again in 1D. As can be seen, the results match well. A point-by-point error difference is presented in Figure 38(b). We predicted the forward error to be on the order of 10^{-5} and, as seen, our results meet this expectation. However, the errors are larger than we have seen previously, in the cases of only examining the forward and inverse Fourier transforms, presented in Figure 36 and Figure 37. This is due to a couple of reasons. The obvious difference is that there is now propagation in this example. With the addition of propagation comes the possibility of a truncation error. In this example, the output signal is slightly truncated, and this causes the increase of the errors in the simulations. This can be reduced by increasing the spatial window, along with the value of N. A second reason for the difference is that even though the magnitude of the function in the frequency domain does not change with the multiplication of the propagation exponential, the phase term of the function is effected. Therefore, aliasing errors can occur in the frequency's

phase term when only assuming that the magnitude of a frequency signal is bandlimited.

4.6.2 Clipped Gaussian Beam

A common optical wavefront found in micro-systems is the case of when the wavefront is piece-wise continuous. This happens when optical wavefronts are clipped by micro-components, such as mirrors, apertures, or screens. When optical beams are clipped, part of the function continues propagating its optical wave shape. However, the aperture blocks the remaining light, and these values in the optical wavefront are set to zero. This results in discontinuities in the function. In this case, the number of continuous differentials is p=0 [45]. Mathematically, our evaluation of the piece-wise error between continuous and discrete transforms does not directly support the case when p=0, since the Rate of Decay of Fourier Coefficients formulation converges for $p \geq 1$. However, with a little more development of the error bound, it has been shown for piece-wise continuous functions like these, that with extensions to the error approach that we presented, the error is on the order [45]:

$$\left|c_k - F_k\right| \leq \frac{Ck}{N^2}, \text{ where } k = -\frac{N}{2} \ldots \frac{N}{2}$$

again, where C is a constant independent of k and N, with a maximum of 1 for a normalized input functions. For the low frequency coefficients (*k* much smaller than the limit of $\pm N/2$), the error acts as CN^{-2}. For the high frequency coefficients (*k* close to $\pm N/2$), the error approaches CN^{-1}, due to aliasing in the frequency domain. Therefore, the maximum error bound in the case when p=0 is equal to, $\left|c_k - F_k\right| \leq \frac{C}{N}$.

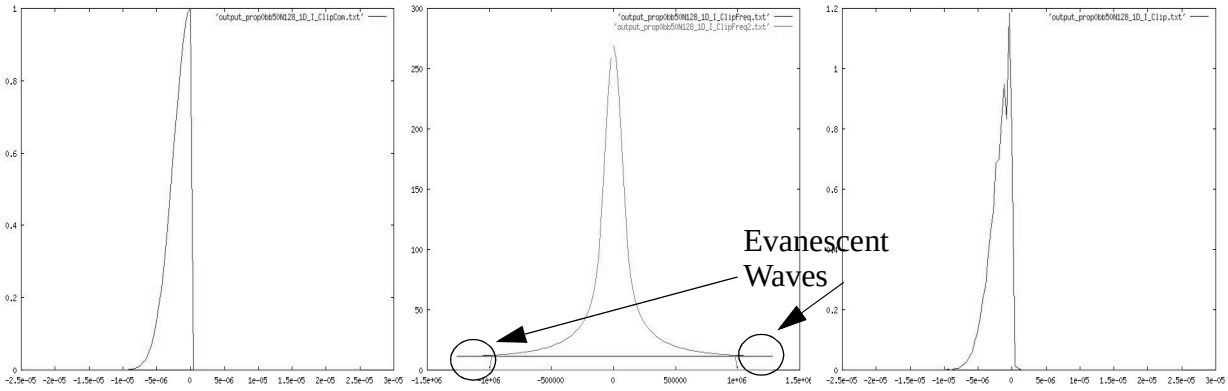

(a) Spatial Domain (b) Frequency Domain (c) Spatial Domain

Figure 39 Forward and Inverse Fourier Transform of a Clipped Gaussian Beam (N=128, window=50 μm)

When attempting to reconstruct the spatial domain from the spatial frequencies using the inverse Fourier transform, we expect to see the largest errors at the points of discontinuities. It is well known that the Fourier transform has a difficult time reconstructing sharp edges of a function. The common Gibbs phenomenon occurs, which is represented by the function "ringing" at the discontinuities [47].

We present an example in which we simulate a Gaussian beam that is clipped in half. In this example, a Gaussian beam with a spot size (which equals 2*w*) of 10 μm and a wavelength of 1 μm is used. We first examine the beam with a bounding spatial box of A=B=50 μm, with N=128. With these values, our sampling is below our general sampling rule of λ/2. We do not propagate the beam past the screen, however, we perform the forward Fourier transform and the inverse Fourier transform to recover the clipped beam. We first examine the spatial domain of the clipped beam, as seen in Figure 39(a). The frequency domain, the result of performing the forward Fourier transform on the spatial domain, is shown in Figure 39(b). Note that the frequency domain does not reach zero at each end. This indicates that aliasing is occurring, and errors in the results

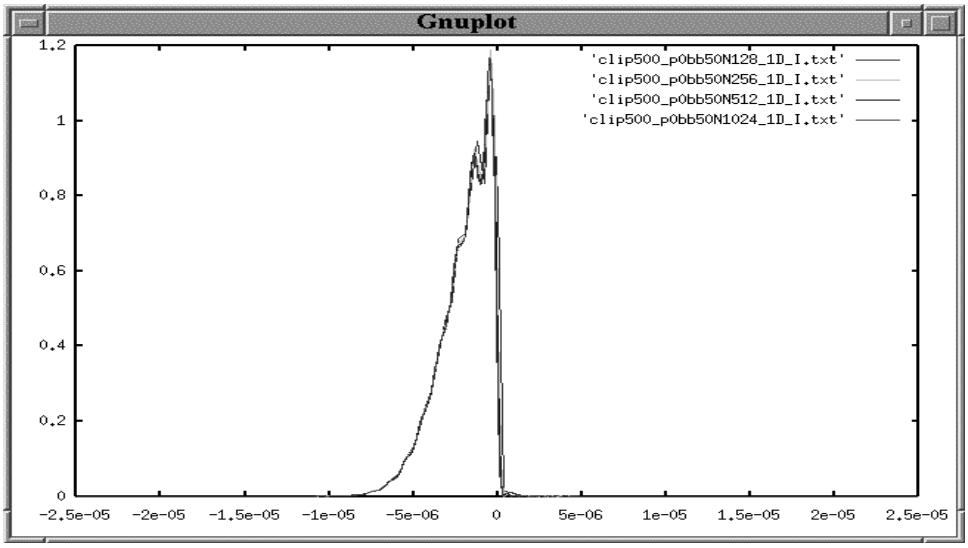

Figure 40 Observation Spatial Domain with N=128, 256, 512, and 1024

can be expected, since the higher order frequencies are being folded over into the lower orders. From our theoretical error analysis, the spatial frequencies in these tails have the order of error, 1/N, where the spatial frequencies in the middle are on the order of $1/N^2$. The recovered spatial output from this frequency domain is seen in Figure (c). Notice the errors in the spatial domain, as shown by the jagged wavefront, a sign of the Gibbs effect.

We next increase the frequency domain window, by increasing the size of N and keeping the spatial domain the original size to determine if this will help the recovery of the signal. Recall from the Fourier transform reciprocity relations, this is achieved by decreasing Δx. However, as we increase the number of sample points in our simulations, the same jagged Gibbs effect result remains. This can be seen in Figure 40, which shows the same spatial response as above with N=128, 256, 512, and 1024.

Recall that in the angular spectrum method, the evanescent waves are removed in the frequency domain with spatial frequencies defined in the range:

$$\frac{1}{\lambda^2} - v_x^2 - v_y^2 > 0$$

Since we remove the evanescent waves in the angular spectrum technique, many of the frequencies are being removed which are required to recover the initial signal, resulting in the Gibbs effect. Therefore, we expect not to recover the exact signal from the aperture spatial domain, as stated before. In Figure 39(b), the evanescent waves are shown, in the tail of the frequency waveform. Figure 39(b) actually shows two frequency functions, superimposed on top of each other. The first is the frequency domain with the evanescent waves, and the second has them removed. We use this second frequency waveform to recover the function in the angular spectrum method.

With this explanation, the results in Figure 40 are expected. For each simulation, the evanescent waves are always removed, the non-zero frequency domain is the same size for each simulation, and the same Gibbs effect is seen in all the cases. Therefore, in the case with no propagation between aperture and observation plane, increasing N does not help.

To determine if the Gibbs effect can be reduced with more granularity in the frequency domain, we half the sampling width, $\Delta\omega$, by doubling both the spatial window and the number of mesh points. In Figure 41, the observation spatial window is shown for three simulations. The first is the original simulation, with N=128 and A=50 μm (Δx=0.39 μm), which results in a sampling in the frequency domain of $\Delta\omega$=20000. The second simulation has N=256 and A=100 μm (Δx=0.39 μm), which results in a sampling in the frequency domain of $\Delta\omega$=10000. In the last simulation, N=512 and A=200 μm (Δx=0.39 μm), which results in a sampling in the frequency domain of $\Delta\omega$=5000. Examining the output in Figure 41, we see that all 3 curves overlap each other exactly. This infers a couple of interesting facts. First, increased sampling in the frequency domain does not help the Gibbs effect. That is because our initially (0.39 μm) sampling was

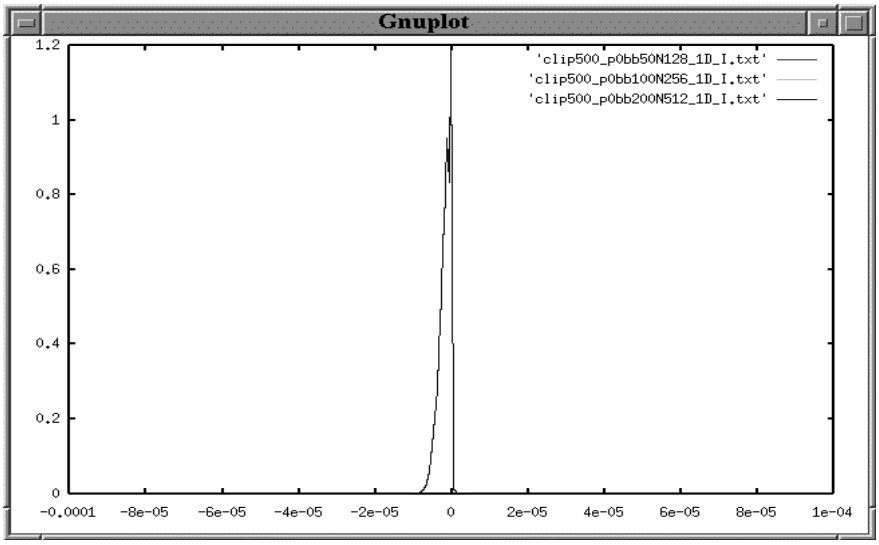

Figure 41 Observation Spatial Domain for 3 cases: 1) N=128, A=50 μm 2) N=256, A=100 μm 3) N=512, A=200 μm

already below our rule-of-thumb λ/2 sampling (0.5 μm). Therefore, the effect that we are seeing with the Gibbs effect is the limitation of the Rayleigh-Sommerfeld formulation, which shows the technique is not valid for propagation distances less than the wavelength of light. However, as we propagate the signal, the Rayleigh-Sommerfeld formulation becomes valid, and we can get accurate results. This has been seen previously, as we have presented accurate results of clipped optical wavefronts propagating past square apertures in Figure 18.

We next simulate the wavefront propagating past the screen. The observation spatial domain is shown for 4 different examples, when the light has propagated 20, 40, 60, and 80 μm past the screen, in Figure 42. For each simulation, we ensured that the general rule-of-thumb sampling requirement ($\Delta x \leq \lambda/2$) was met, and that there was no truncation. Therefore, for 20 μm of propagation, A=100 and N=256. For 40, 60, and 80 μm of propagation, N was 512, and A was 150, 200, and 250 μm, respectively. As can be seen in the diagram, the Rayleigh-Sommerfeld formulation becomes valid with propagation between the aperture and observation plane. Notice how the beam return to a Gaussian-like shape, with a new position for the maximum intensity.

In summary, when an aperture clips a beam, discontinuities occur in the wavefront. These discontinuities are difficult for the discrete Fourier transform to model, therefore, the original optical wavefront can not always be reconstructed, as we saw in Figure 39. The Rayleigh-Sommerfeld is not valid for distances of propagation less than the wavelength of light. Therefore, inaccurate results are expected when looking at waveforms without any propagation. However, we can still retain accurate results using the angular spectrum technique to solve the Rayleigh-Sommerfeld formulation when we propagate the wavefront. The angular spectrum algorithm removes the evanescent waves, resulting in a bandlimited signal, which enables the propagating plane waves in the Fourier domain to reconstruct and give an accurate signal within the stated error bound of C/N.

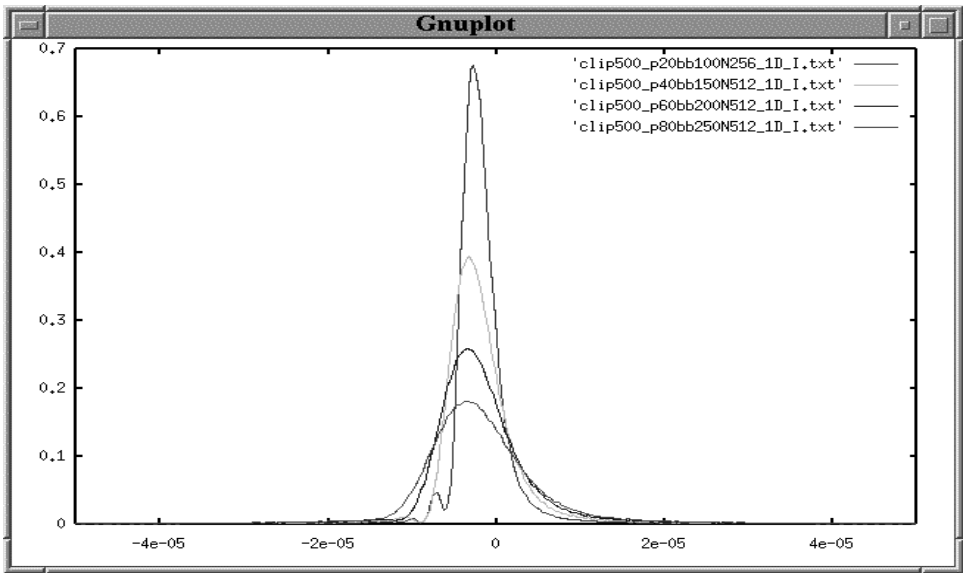

Figure 42 1D Cross-section of Observation Spatial Window for Propagation Past the Screen of 20, 40, 60 and 80 μm

4.6.3 General Example

In the case where we have a general function, the process of determining the error becomes more difficult. In this case, the number of continuous derivatives or smoothness (denoted as *p* in our error discussion) of the function needs to be determined, and this value will correspond to the order of the error bound of the Fourier transform. As previously mentioned, the determination of the functions continuous derivatives could be determined with a standard numerical algorithm performed on the function. However, this comes at the cost of the simulation time.

In Figure 43, we present a flow chart of the technique that we take to estimate the errors in performing the angular spectrum technique to solve the Rayleigh-Sommerfeld approximation. At

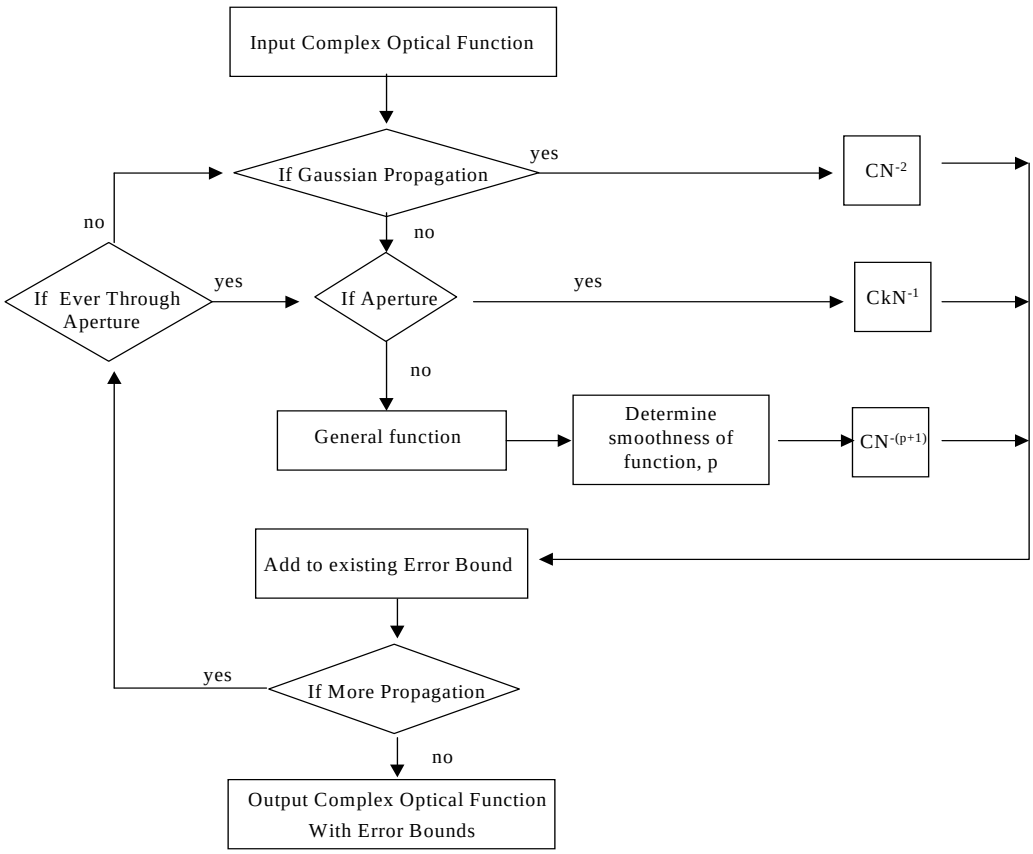

Figure 43 Error Calculation Algorithm for a General Function

the top of the flow chart, we start with the input optical wavefront. Since we have characterized the errors of two of the most common optical wavefronts, a Gaussian beam propagation and a piece-wise continuous wavefront, we first check to see if the optical wavefront is either of these cases. If it is, the proper error calculation for the case is applied, and we add appropriate error estimate to the existing error bound of the system. If this is the first propagation, and there is no established error bound, one is created. We add the error from the current propagation gap to the error bound, since the total system error gets worse as the error propagates through the system. If the function does not fall into one of the two cases, the function is a general complex wavefront. In this case, the smoothness of the complex wavefront is determined though calculating the derivative of the function. The proper error value is then determined, and added to the error bound of the system.

The algorithm continues by determining if there are more free-space propagation gaps in which the wavefront needs to propagate. If this is true, we return towards the top of the algorithm, however, we first determine if the function has ever been clipped through an aperture. If this is the case, it can no longer propagate as a Gaussian beam, and we do not have to perform the Gaussian check. The error of the next propagation is calculated by one of the standard error conditions or the general function and is added to the existing system error bound. This continues until the simulation through the system is complete, and we are left with the output complex optical function, and system error bounds of the result.

It is interesting to note, that if the optical wave ever propagates through an aperture, this will extend the error bounds to C/N, the largest error bound that we have encountered. Therefore, if this is the case in the system, then the error margin is known, before the simulation is even performed. Since this error bound is a high error value, it is important to note that the error could be

(and often is, as seen in the previous error calculations) much less than the maximum error bound.

We next show how we have implemented our angular spectrum technique into our mixed-signal, multi-domain CAD tool, Chatoyant. We illustrate system-level simulations of a optical MEM switch and an digital display device using the grating light valve.

5.0 IMPLEMENTATION INTO A SYSTEM-LEVEL CAD TOOL

In this chapter, we describe the implementation of our efficient optical propagation technique into a mixed-signal, multi-domain, system-level CAD tool. We first introduce our system-level CAD tool, Chatoyant, which supports systems containing the optical, electrical, and mechanical domains. We describe the current modeling methodologies for the creation of such a tool. A discussion of the implementation of the new optical technique into the tool follows. This is followed by a brief description of the other optical modeling techniques, along with the electrical and mechanical models, found in Chatoyant. This chapter concludes with two system-level simulation examples. The first is a simulation of a 2x2 optical MEM switch, with the use of a mirror fabricated on a cantilever beam which is electro-statically actuated to switch light from one path to another. The second example is a digital display projection system. This is enabled by the use of a diffractive GLV device. Careful examination of light diffracting off of the bending ribbons is presented. However, before we present the simulations, we introduce the simulation environment.

5.1 Our Mixed-Signal Multi-Domain CAD Tool: Chatoyant

At the University of Pittsburgh, we have developed a multi-domain, mixed-signal CAD tool, *Chatoyant*, to support the system-level modeling and simulating of micro-opto-electro-mechanical systems [18][53][54][55]. Chatoyant has been successfully used to design and simulate free space optoelectronic interconnect systems performing static and dynamic simulations. Static simulations analyze such system-performance measures as mechanical tolerancing, power loss, insertion

loss, and crosstalk, while dynamic simulations are used to analyze data streams with techniques such as noise analysis and bit error rate (BER) estimation. Chatoyant is built upon the object-oriented simulation engine Ptolemy, a CAD tool from the University of Berkeley, originally created for signal processing CAD under the DARPA funded RASP program [56].

As a example of the framework, a Chatoyant schematic of a free-space 1x2 optical MEM cross-connect is shown in Figure 44. In Chatoyant, each icon represents a component, or behavioral, model. Each of the component models are written in C++ with sets of user defined parameters for the characteristics of each module instance. Each line, or "wire" represents a signal path (either optical, mechanical, or electrical) connecting the outputs of one component to the inputs of the next. This system shows an optical fiber emitting light into a free space medium. The light then travels through a collimating lens and is reflected off of a switching mirror, into the path of one of the outgoing fibers. Each optical path contains a second collimating lens, which focuses the light into the corresponding outgoing fiber. The mirror is assembled on an anchored cantilever beam, which bends into and out of the optical path by electrostatic attraction between the beam and the substrate. Three electrostatic forces are placed on the beam/mirror icon; on the x

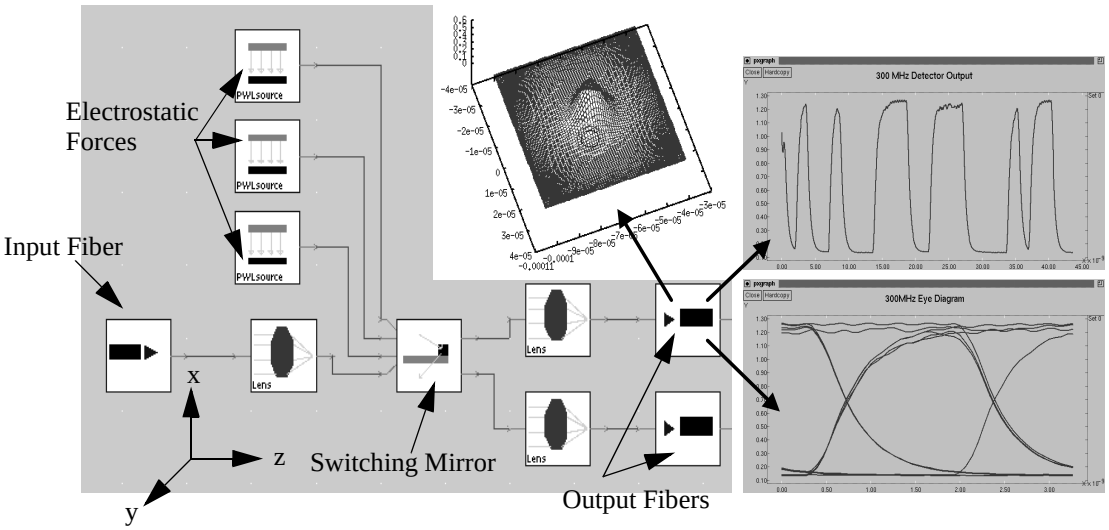

Figure 44 Example Chatoyant Simulations

and z positions and a torque around the z axis. Above the schematic, we show an optical intensity distribution as light strikes one of the outgoing fibers, while, on the right of the figure, we show a dynamic waveform and eye-diagram from a data signal being passed through the switch. Details of this system are given during a full analysis of the system later in this chapter.

The actual approach for our modeling of mixed signal multi-domain systems is a discrete event driven simulation model, which operates over the global system. We choose the "Dynamic Data Flow" (DDF) Ptolemy simulation method as our discrete event engine. Timing information is added to support multiple and run-time-rate variable streams of data flowing through the system. In this model of computation, the simulation scheduler creates a dynamic schedule based on the flow of data between the modules. In other words, the order of execution of modules is set during run time. This allows modeling of multi-dynamic systems where every component can alter the rate of consumed/produced data at any time during simulation. The scheduler also provides the system with buffering capability. This allows the system to keep track of all the particles arriving at one module when multiple input streams of data are involved [57].

The information flow is handled using a "message class". The parameters that characterize the signals are encapsulated in the message class to be sent and received throughout the system. As previously mentioned, the message class carries time information for each message in the stream of data. This allows for the dynamic insertion and deletion of samples at any time in the system by any component. Modules that operate on multiple data streams of different rates use this time information to maintain the order in the stream of incoming data. To maximize our modeling flexibility, our signals are composite types, representing the attributes of force, displacement, velocity, and acceleration for mechanical signals, voltages and impedances for electronic signals, and wavefront, phase, orientation, and intensity for optical signals. The composite type is

extensible, allowing us to add new signal characteristics as needed.

Recall that Chatoyant is a system-level CAD tool, analyzing systems through such system-performance measures as bit-error-rate, insertion loss, and tolerancing. Although, in a system-level CAD tool, accurate and interactive results are both primary goals. This allows a designer to get feedback in a "reasonable" amount of time, therefore, an interactive system level tool, such as Chatoyant, occasionally might sacrifice a degree of accuracy to support faster simulation time. These user-defined trade-offs between speed and accuracy can be useful to the designers using our tool.

Component models are based on three modeling techniques. The first is a "derived model" technique. That is, analytic models based on an underlying physical model of the device. These can be very abstract "0^{th}-order" models, or more complex models involving time varying functions, internal state, or memory. The second class of models is based on empirical measurements from fabricated devices. These models use measured data and interpolation techniques to directly map input signal values to output values. The third technique is reduced order or response surface models. For these models, we use the results of low level simulations, such as finite element solvers or Spice, and generate a reduced order model, which covers the range of operating points for the component by producing a polynomial curve fit, or simple interpolation over the range of operation.

We have successfully used all three of these methods in the creation of four component libraries. The Optoelectronic Library includes vertical cavity surface emitting lasers (VCSELs), multiple quantum well (MQW) modulators, and p-i-n detectors. The Optical Library contains components such as refractive and diffractive lenses, lenslets, mirrors, and apertures. The Electrical Library includes CMOS drivers and transimpedance amplifiers, and the Mechanical Library

contains scratch drive actuators and other electro-static devices.

We now briefly introduce the signal (optical, electrical, and mechanical) modelling techniques that are used in Chatoyant. We first show the implementation of the Rayleigh-Sommerfeld formulation into Chatoyant.

5.2 Implementation of Rayleigh-Sommerfeld Optical Propagation into Chatoyant

As been stated, the author's main research has been concentrated on the optical devices and propagation models. Throughout this thesis, we have shown that the Rayleigh-Sommerfeld formulation is an accurate optical propagation technique that is appropriate for the simulation of optical microsystems. This technique has been computationally improved with the use of the angular spectrum method, which is an exact solution to the Rayleigh-Sommerfeld formulation.

For the implementation of this technique into Chatoyant, additions were made to the message class. Support for a complex wavefront is added to the message class. This is a NxN 2D array, in which each cells holds a complex value of the optical wavefront. The complex optical wavefront is meshed into discrete values, and placed into the array, as it is passed from component to component. Also in the message class is the actual code of the Rayleigh-Sommerfeld optical propagation algorithm. Since each optical component uses the same optical propagation algorithm, it was advantageous to put the code in the message class, instead of repeating the code in each component.

As seen through the description of the angular spectrum method, the computational load is dominated by the FFT. Like the direct integration technique, the FFT technique requires the aperture and observation planes to be discretized into a NxN meshes, where N is the number of mesh

points on the side of the plane. Equal spacing meshing is required, and for ease of the FFT algorithm, a power of 2 is required for the number of mesh points in the algorithm that we are using from Numerical Recipes in C [42]. In our discussions and simulations, the aperture and observation planes are meshed with the same N, however.

The angular spectrum algorithm was described in Chapter 3, with a graphical description in Figure 13. We summarize our algorithm for the implementation of this technique here. First the forward FFT is applied to the aperture surface. This is then multiplied by the propagation phase term. If tilts are present, the aperture plane's spatial frequencies are mapped into the observation plane's spatial frequencies. If offsets between the planes occur, then the shifting theorem is applied. Finally, the inverse FFT is applied, and the complex wavefront on the surface of the observation plane is obtained.

Supporting the algorithm and the complex array of values representing the optical wavefront, the angular method has been successfully integrated into Chatoyant. We now briefly introduce other optical modeling techniques, along with modeling techniques for the electrical and mechanical domain.

5.3 Modeling Techniques for Signals in Chatoyant

In this section, we describe the signal modeling for the other domains found in Chatoyant. We first describe other optical propagation techniques that are found in Chatoyant, besides that new angular spectrum solution to the Rayleigh-Sommerfeld formulation. We next briefly introduce the electrical and mechanical modeling techniques that are found in Chatoyant. The electrical and mechanical work is not the authors work and details can be found in [57].

5.3.1 Additional Optical Propagation Modeling

Besides the Rayleigh-Sommerfeld optical propagation technique, Chatoyant has continued support for other optical propagation techniques. These techniques were developed when Chatoyant was used for optical macro-system modeling. For macro-systems, a mixture of ray and Gaussian optics can be ideal for system-level modelling. We calculate the position and direction of the center of the Gaussian beam using ray propagation methods. The Gaussian beam is "super-imposed" over the ray-traced beam to model the intensity, waist, and phase of the light beam [18]. The advantage of using Gaussian beam analysis is the fast computational speed in which light is modeled and propagated, allowing for interactive system-level design. This method has worked well for macro-scale systems, defined as systems without strong diffractive effects. This work has been the basis of Coventor's optical system level modeling, where the author has converted our Chatoyant models into Saber's MAST, an AHDL (analog hardware description language) based programming language [39].

As we have explained in the thesis, for many micro-systems, diffractive effects can dominate, and the Gaussian propagation will not always be accurate. For these systems, the scalar methods, using both brute force integration and the angular spectrum optical methods must be used. As mentioned in the above section, the angular spectrum technique has been implemented into Chatoyant [58]. We also include the brute-force Rayleigh-Sommerfeld integration which has been implemented in Chatoyant, as seen in [3]. The direct integration approach is performed with a Gaussian Quadrature numerical method [59]. We have extended the brute force direct integration technique solving the Rayleigh-Sommerfeld propagation formulation to support optical surfaces which are slightly curved [60]. Although this extension uses the computationally slower Rayleigh-

Sommerfeld algorithm, it does allow some flexibility in the systems that can be modeled. We now give a description of the extension.

The Rayleigh-Sommerfeld formulation for scalar optical propagation assumes no curvatures in either the observation or the aperture plane. This is due to the general formulation not recalculating the distance of propagation for a curved surface. By again examining the Rayleigh-Sommerfeld equation, and Figure 6, we can easily see this:

$$U2(x,y) = \frac{z}{j\lambda}\iint_{\Sigma} U1(\xi,\eta)\frac{e^{jkr}}{r}d\xi d\eta \qquad r = \sqrt{z^2 + (x-\xi)^2 + (y-\eta)^2}$$

Through the equation and the diagram, it is seen that the aperture and observation planes are flat, with the value of z being constant. However, in our use of the Gaussian Quadrature method to calculate the Rayleigh-Sommerfeld integration, we are easily able to determine the (x, y, z) center position for each mesh. This enables us to expand the Rayleigh-Sommerfeld formulation to support slight curvatures. Therefore, we are able to exactly calculate the distance that each wavefront travels (r) to get from aperture to observation plane. This allows us to model curved surfaces using an extension of the Rayleigh-Sommerfeld formulation, now using and solving three position values, with the following equation:

$$U2(x,y) = \frac{z}{j\lambda}\iint_{\Sigma} U1(\xi,\eta)\frac{e^{jkr}}{r}d\xi d\eta \qquad r = \sqrt{(z-\zeta)^2 + (x-\xi)^2 + (y-\eta)^2}$$

Examples of curvature will be seen later in this chapter with simulating an optical MEM switch.

5.3.2 Electrical and Mechanical Modeling

As mentioned, Chatoyant is a multi-domain CAD tool, supporting optics, electronics, and mechanics and the interactions between these domains. The electrical modeling is based on piece-wise linear modeling and modified nodal analysis (MNA) matrices, as described in Martinez's Masters of Science thesis [61] and in the journal [57]. The approach for modeling mechanical elements is to reduce a mechanical ODE representation for a component into a form matching the solver used for the electrical domain. This enables the use of our same piece-wise linear solver for the mechanical models as for simulating the dynamic behavior of electrical systems.

These techniques, along with the optical modeling methods simulate together in a single framework to give the designer and complete CAD tool for mixed-signal, multi-domain modeling of optical micro-systems.

5.4 System-Level Examples

In this section we provide some system-level examples of modeling multi-domain micro-systems with our CAD tool Chatoyant. In the first example, we simulate a 2x2 optical MEM switch. In particular, we analyze the switching speed of the switch, and how this effects the optical efficiency of the complete system. In the second example, we simulate and analyze a digital display using a GLV device. Many different simulations are performed with this GLV systems, resulting in design information of the fabrication of the mechanical ribbons, the optical input, and the distance that the ribbons must be electro-statically attracted to the substrate, and their resulting shape. These examples show how we model all three domains, optical, electrical, and mechani-

cal, and the interactions between the domains. Since the author's research and focus of the thesis is regarding accurate and efficient optical propagation, this will be the focus of the simulation and analysis of the example systems.

5.4.1 2x2 Optical MEM Switch

In this first simulation, we perform both static and dynamic simulations of a 2x2 optical MEM switch. The simulated system is similar to those being researched by such companies and institutions as Bell-Labs [62], UCLA [63], and University of Neuchael, Switzerland [64]. This architecture consists of a set of four optical fibers in the shape of a "+" sign, with the input and output fibers facing each other through a free-space gap, as seen in Figure 45. The switch is in the "cross" state when light is passed straight across the gap. To achieve the "bar" state, a mirror is inserted between the fibers at a 45 degree angle and, the light is reflected to the alternate output. The mirror fabrication and positioning can be achieved in a variety of ways. For example, Bell-labs [62] inserts a "see-saw" pivoting mirror into the optical path, which is also seen in Figure 45, with the mirror in position to achieve the bar state. UCLA and AT&T use scratch drive actuators

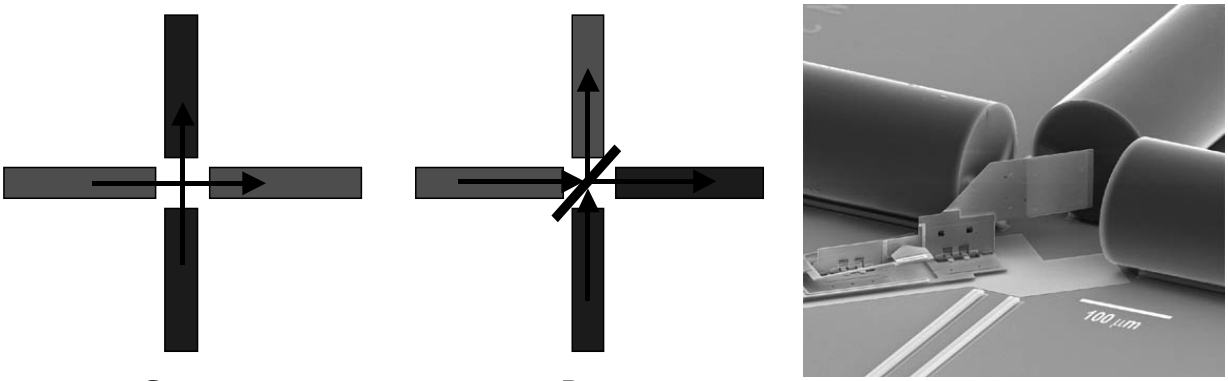

Cross Bar

Figure 45 2x2 Optical MEM Switch (from Bell-Labs)

to assemble and position the mirror between the fibers, and the University of Neuchael, Switzerland uses a combdrive actuator to slide the mirror into place.

In the following simulations, the input and output fibers are both 10 μm core, single mode fibers with an index difference of 0.006 between the core and cladding, length of 1000 μm, and support 1550 nm wavelength light. A 1550 nm Gaussian beam with a 10 μm (almost the ideal "mode" of the fiber) waist is used as a source to the first fiber.

The system, as seen in the Chatoyant GUI, can be seen in Figure 46. RSoft's BeamPROP [11] is used to simulate the light through the fiber. We have developed an interface between the fiber propagation (BeamPROP) and free-space (Chatoyant) through a data file.

The optical MEM switching system that we simulate is based on a fabricated device from UCLA [65]. This 2x2 switch is based on four fibers coming to a 4-way free-space intersection. In the UCLA design, a hinged micro-mirror is fabricated at the end of an anchored mechanical beam. In the steady state, the beam is resting in the optical switching path, and the system is in the bar state. Through electrostatic attraction between the beam and the substrate of the surface, the mechanical beam can be bent towards the substrate, moving the mirror out of the optical path completing the cross state of the system.

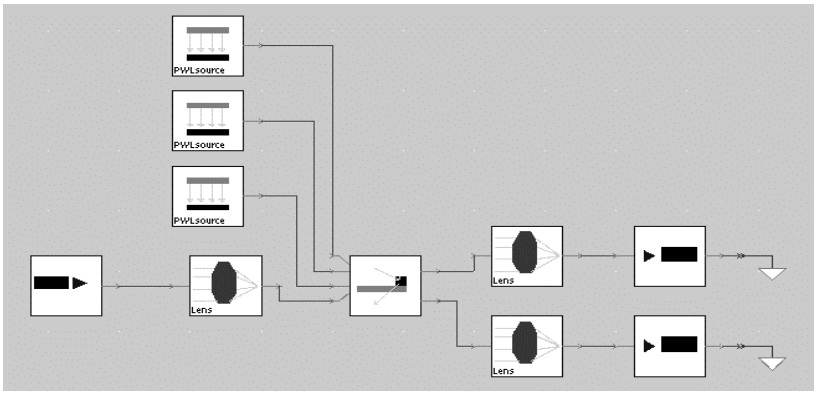

Figure 46 2x2 Optical MEM Switch as seen in Chatoyant

For simplicity, we simulate only a single input switching to either the cross or bar state throughout this example. The mirror is 100 x 100 μm, and is positioned at the end of a 700 μm cantilever beam. Both beam and mirror are fabricated with polysilicon, with the mirror having an ideal reflectivity of 100%. The beam is 2 μm thick and 100 μm wide, while the mirror is 4 μm thick, to counteract the induced residual stress that otherwise would curve the mirror. Collimating lenses (f = 50 μm) are placed 50 μm from the fiber ends, and there is a free-space gap of 100 μm between the lenses. The mirror, when placed in the optical path, is positioned in the center of the free-space gap, 50 μm from each lens.

5.4.1.1 Static Simulations We first examine a static simulation of the switch working in both the bar and cross states. The system set-up and simulation results for both switching states are seen in Figure 47. Chatoyant presents intensity outputs at each component throughout the system, and the intensity profiles of the light propagating through the fibers is from BeamPROP. If no mirror is present, the light propagates straight through and achieves a cross connection, as shown

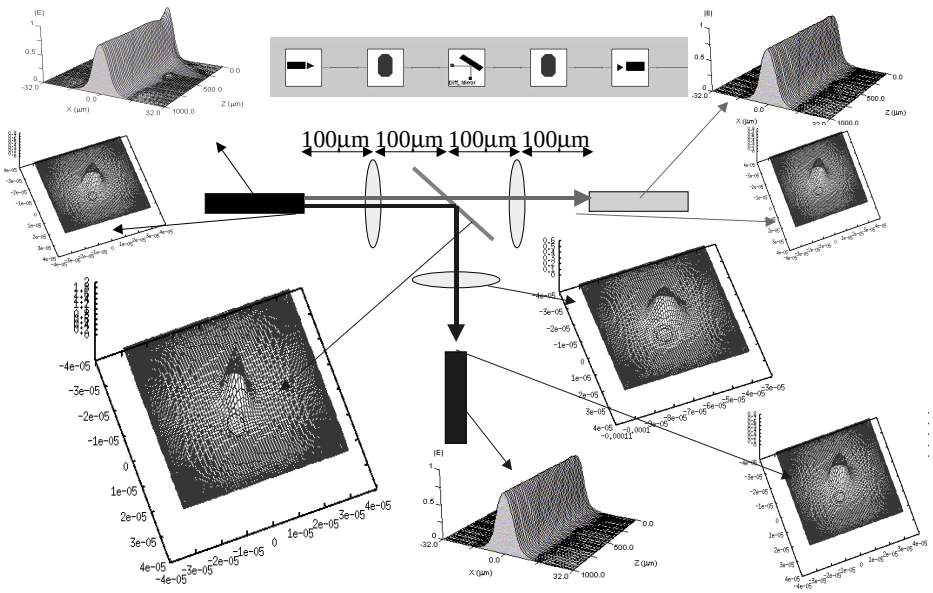

Figure 47 Static Switch Simulation

by the top “light” arrow. However, with the addition of the mirror, the optical path is reflected 90 degrees, as shown by the “dark” arrow, and the bar state is connected. In these simulations, the mirror model is assumed to be ideal, with a 100% reflectivity. The additional arrows in the figure show at which point in the system each of the intensity distributions is from. As the light propagates through free-space, notice how the beam waist expands. Also notice, how the beam waist appears oval on the tilted 45 degree mirror. Both the cross and the bar states have less than 1dB of loss through the free-space switching system, and fit well back into the output fiber.

When fabricating micro-mirror MEM devices for an optical MEM switch, the flatness of the mirror is essential, since curvature and deformities can result in errors in the system. However, curved surfaces are common in optical MEM systems, since many thin components experience an inherent curvature due to factors including the fabrication material, the fabrication processes, and internal residual stress. Gold is commonly used as the top material of the mirror, increasing the reflectivity, however, this metal can still suffer from curvature problems [5]. As the size of the mirror increases, usually so does the curvature. Many techniques are commonly practiced in attempting to keep the mirror flat, including smaller sizes (widths and lengths) of the mechanical pieces. Another mirror-flatting fabrication technique is to create a sandwich of polysilicon-phosphosilicon-polysilicon, resulting in a mirror thickness of approximately 4 μm. This structure causes the mirror to remain rigid, even when a metal layer (Au) is added to increase the reflectivity of the mirror. However, even with these precautions, micro-mirrors can still have serious curvature, and we need to be able to model its effects in our CAD system.

We next present simulations that show the effect of using curved optical components in a micro-optical system. In these simulations, we again model reflection off of a 10x10 mm mirror, however, we now simulate a curvature (R=1mm) in the mirror. For these examples, we assume a

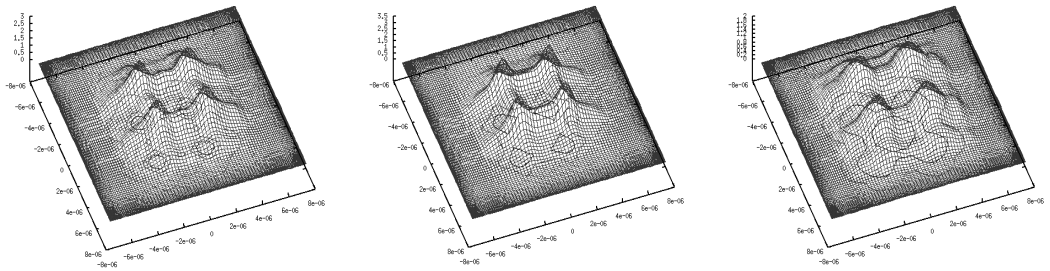

A) Flat B) Concave C) Convex

Figure 48 Intensity Distributions of Propagation off a Curved Mirror

surface roughness of zero. In Figure 48, we show intensity surface and contour distributions of light reflecting from the mirror and being detected on a 15x15 μm observation plane. The simulation result at the left of the Figure 48, (A), shows the result of reflection from an ideally flat mirror, as a basis for comparison. In the intensity distribution in the center, (B), the curvature is concave (-R), so the beam starts to converge towards the focus point of the mirror (f=R/2). In the third distribution, (C), the light strikes a convex mirror (+R), with the same degree of curvature, resulting in the divergence or spreading of the light. The simulated power detected on each of these observation planes is essentially the same, although the shape and focus (i.e., convergent or divergent) of the reflected beam is different. These effects can cause insertion loss as the beam propagates further down the optical path.

5.4.1.2 Dynamic Simulations Returning to our simulation of the 1x2 switch, we next use Chatoyant to analyze the dynamic mechanical movement of the cantilever beam on which the mirror is fabricated. The more significant mode frequencies of the beam, including the mirror mass, are determined to be 3.7 kHz and 27.1 kHz. These results are within 5% of the solution given from the mechanical finite element CAD tool, ANSYS [(66)]. For a switching speed of 400 μsec, the response of the beam, in terms of the center position of the mirror from the original

steady-state value, is shown in Figure 49 (b). The switching electro-static force applied to the cantilever beam is also included in Figure 49 (b), represented by the dashed line.

We next examine the optical power that is detected on a 100 μm square observation plane at the bar fiber. Optical intensity distributions at the observation plane are included for three points on the response curve, labeled *A*, *B*, and *C*. *A* is when the mirror is completely inserted in the optical path, achieving the bar state in the system. *B* is at the point where the mirror is totally out of the optical path, achieving the cross state. As seen in the intensity distribution, no substantial power reaches the bar fiber observation plane. As the mirror bounces, *C* is measured as the mirror partially moves back into the optical path, causing some light to be reflected off the mirror and be detected at the bar fiber. However, at this time, the switch is set in the cross state, causing the possibility of crosstalk or the detection of a false "1" on the bar fiber. This problem is further exemplified in Figure 50 (a). This shows a graph of the power detected on the bar fiber end (10 μm diameter) in terms of dB lost. As expected, the power detected corresponds to the mirror position movement seen in Figure 49 (b). With the mirror response, point *C* has a power loss of only 3 dB at the bar fiber end, resulting in 50% of the power still being detected at the bar fiber.

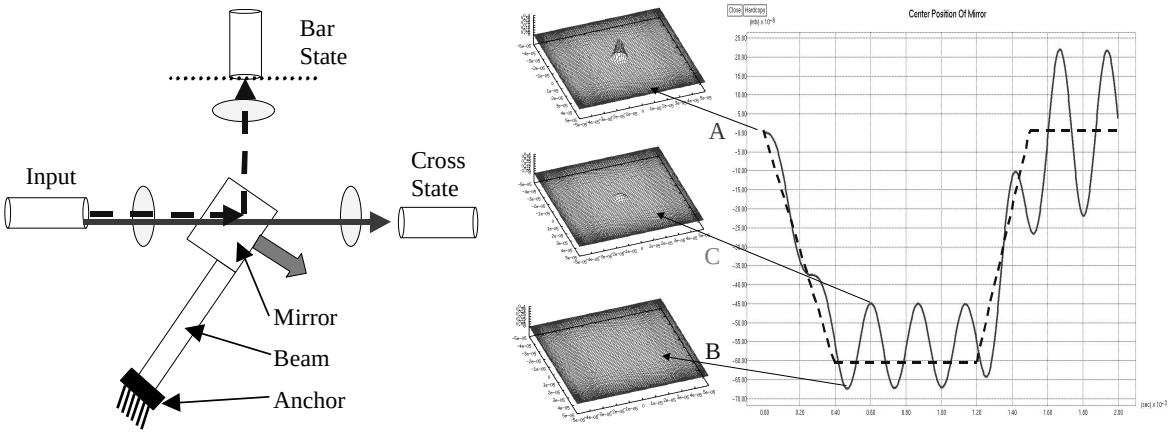

Figure 49 (a) Switching System(b) Mirror Response and Intensity Distributions (Switching Time = 400 μsec)

The three intensity contours for each of the points are seen in Figure 50 (b), along with a circle drawn to represent the fiber end. For case *A*, the light strikes the mirror in the center and reflects directly into the bar fiber. As seen through Figure 50 (a) and (b), the contour for *A* is directly on the fiber, and we consider this full detected power (0 dB loss). For case *B*, the mirror is moved totally out of the optical path, resulting in virtually no power being detected on the fiber (61 dB of loss). However, it is interesting to note that even though almost no power is received at the fiber end, there is still a diffractive effect, with very low power, striking the observation plane, approximately 28 μm away from the fiber center. In this system, this diffractive effect is not destructive, however, an effect like this could introduce crosstalk in larger scaled systems. For case *C*, when half the optical beams reflects off the mirror, the power is still concentrated, however, it is centered 3 μm from the fiber center, resulting in a 3 dB loss of power at the bar fiber end.

With the switching speed of 400 μsec, it has been seen that the ringing of the cantilever beam can deteriorate the effectiveness of the entire system. To show the switch work without the possibilities of significant crosstalk between the cross and bar states, the switching time is reduced to 600 μsec. The bounce of the cantilever is no longer significant, and the system experiences close

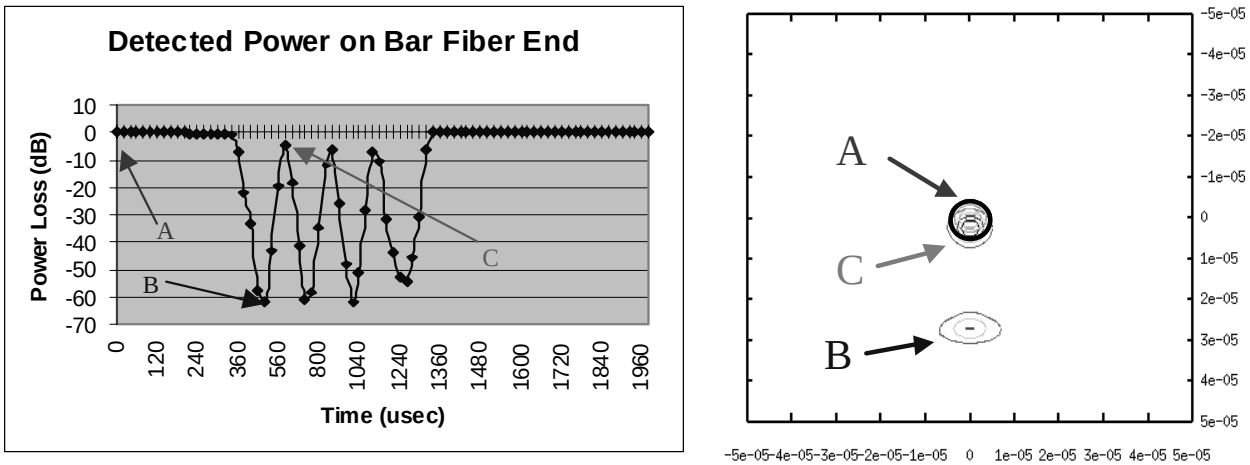

Figure 50 (a) Power Received on End of Bar Fiber (b) Contour Distributions

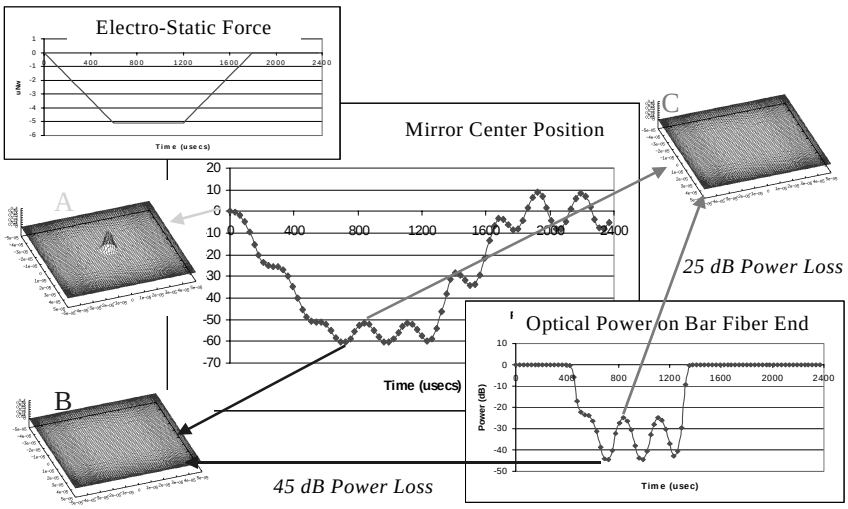

Figure 51 Mirror Response and Intensity Distributions (Switching Time = 600 μsec)

to zero crosstalk, as can be seen in Figure 51. In this figure, we show the input electrical force, seen in the upper left hand corner, and how this effects the movement of the center of the mirror. The mirror movement is seen in the center of the figure. In the lower right hand corner, is the optical power that is detected at the bar fiber. The ringing in the cantilever, with the slower switching speed, no longer bounces the mirror into the optical path, and the power detected in the bar state, even though the power should be in the cross state, is minimal (less than -25 dB).

5.4.2 Projection Display Systems Using the Grating Light Valve (GLV)

In the second example, we simulate a projection system based on the GLV component, that was described previously in Chapter 2. Although this example clearly shows the benefit of using a mixed-signal, multi-domain CAD tool, it also shows the advantages of using the angular spectrum method to solve the Rayleigh-Sommerfeld formulation. We first simulate the system with an ideal GLV device, that is, a GLV device that ribbons move without any bending or curvature. This is followed by a simulation of the realistic bending of the GLV ribbons, how light diffracts

off of these ribbons, and the effect that this has on the entire system performance.

In the simulations of the GLV system, we examine one optical pixel. A projected pixel is diffracted from a GLV composed of 4 ribbons, two stationary and two that are movable [8]. Each ribbon has a length of 20 μm and a width of 5 μm. Ideally, there is no gap between the ribbons, however, in reality, a gap is present and is a function of the feature size of the fabrication. This gap can be modeled in our simulations and an example of gap size versus power efficiency will be presented later.

The GLV is modeled as a phase grating, where the light that strikes the down ribbons propagates a half of a wavelength more than the light that strikes the up ribbons. In our model, the light reflecting from the down ribbons are multiplied by a phase term. The phase term is similar to a propagation term through a medium:

$U_{\text{down\_ribbon}} = U\exp(j2kd)$, where, d is the distance that the ribbon is moved down.

Through far-field diffraction grating theory, the diffracted angle reflected from the square-well grating is [23]:

$$\theta = q\frac{\lambda}{a},$$

where, q is the diffraction order (0, ±1, ±2, ±3,…), a is the period of the diffractive grating, and θ is in radians. In most diffractive gratings, all the modes are filled. However, in the case when light is diffracted by a grating with a displacement of λ/4, resulting in a λ/2 optical path difference after the reflection, the diffractive interference removes all the power from the even modes, and places the power into the odd modes [67].

5.4.2.1 Standard GLV Operation In the first simulation, the standard operation of the GLV is presented. We assume an incident plane wave of green light (λ=520 nm) striking the grating, with

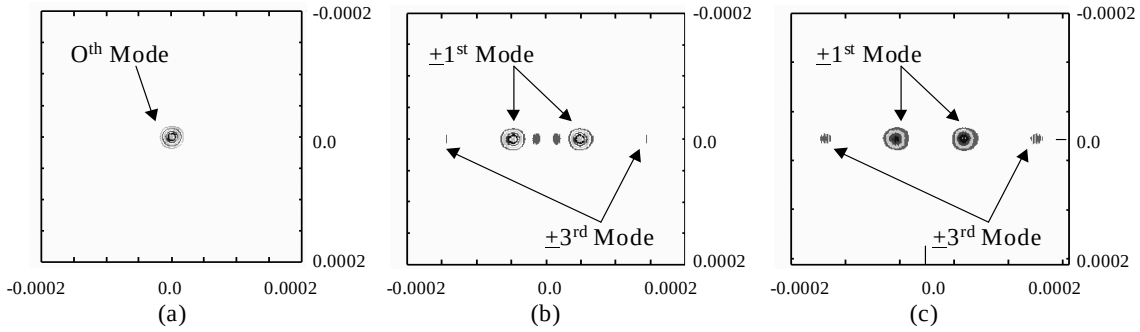

Figure 52 GLV Operation (a) All Ribbons Up (b) Alternating Ribbons Down (c) Fraunhofer Approximation

the square-well period defined by the ribbon width, and no gap. We simulate the GLV in both cases, that is, when all the ribbons are on the same plane and when the alternating ribbons are moved towards the substrate a distance of $\lambda/4$. In this example, the light is reflected off of the grating and propagated 1000 μm to an observation plane. A computation window of 400x400 μm is used, with N equal to 2048. Intensity contours of the observation plane are presented in Figure 52(a) for when the ribbons are all on the same plane, and in Figure 52(b), for when alternating ribbons are pulled down a quarter of the wavelength of the incident light.

Notice when the grating is in the down position, all of the power is not transferred into the ±1st diffractive modes, as other optical power is scattered between the first modes. These are near field effects, and demonstrate that in this system, light propagated 1000 μm is not in the far-field. LightPipes [31], a CAD tool using the Fraunhofer approximations, is also used to simulate this example for comparison, as seen in Figure 52(c). Using the Fraunhofer technique, the near field diffraction is incorrectly modeled, as only the far field effect of light moving into the ±1st and ±3rd modes in seen.

5.4.2.2 Simulation of the Gaps between GLV Ribbons To show system-level multi-domain modeling and the ability to trade-off different technologies, we next examine realistic gaps between the GLV ribbons. The gap between the ribbons is usually the feature size of the lithographic tools used to fabricate the MEMS device [68]. In this simulation, we use the same setup as before. However, this time, we simulate the normalized power efficiency captured in the 1st diffraction mode for different gap sizes. We detect the power in a circle with a radius of 12.5 μm centered on the positive 1st mode. For propagation of 1000 μm, the power meter is centered approximately 52 μm (2.98 degrees) away from the origin. Simulations are performed for common fabrication technologies (1.2, 1, 0.8, 0.6, 0.5, 0.35 μm), defining the size of the gap between the GLV ribbons. These results are compared with geometrical calculations of the estimate power efficiency for ribbon gaps [68], as seen in Figure 53. The geometrical calculations were based on the fill factor of a 25 μm pixel. The diffractive effects of simulating the wavefront into the near field account for the slight differences. As seen in the previous example, all the light does not end up in the 1st diffractive modes, and is diffracted elsewhere.

5.4.2.3 Transient Sweep of the Ribbon Movement In the next simulation, we perform a transient sweep of the ribbon movement, from 0 to 150 nm. The rest of the system setup is exactly the

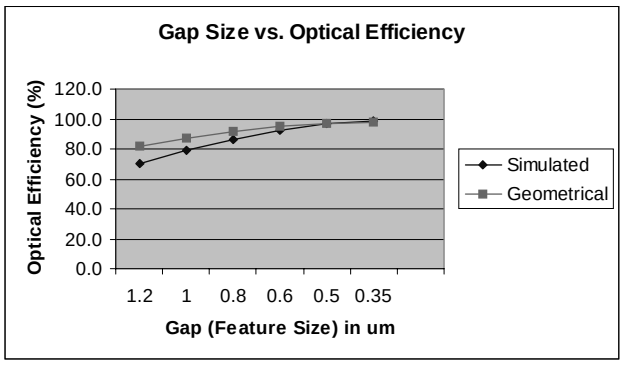

Figure 53 Gap Size vs. Optical Efficiency

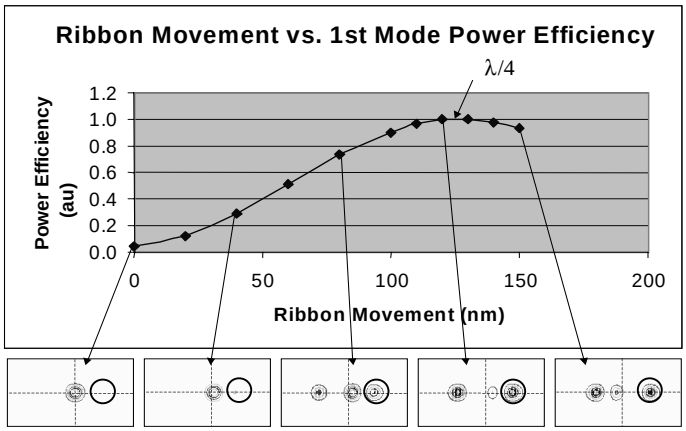

Figure 54 Transient Analysis of Ribbon Movement and Intensity Contours

same as before, with no gap between the ribbons. Again, we determine the normalized power efficiency in the 1st mode, using the same technique as in the previous example. Figure 54 is a graph that shows the simulated normalized power efficiency in the first mode. As the ribbons are moved downward, more optical power is diffracted into the non-zero modes. As the ribbons reach the λ/4 point, almost all the diffractive power is in the +1st mode. Figure 54 also includes intensity contours of selective wavefronts during the transient simulation, on which the detector position is marked with a circle and hashmarks denote the center of the system. From these wave-fronts, interesting diffractive effects can be noted. As expected, when there is little or no ribbon movement, the all the light is in the 0th mode. With a little ribbon movement, it is interesting to note that the 0th mode can be steered at an angle. This beam steering effect is used in systems using similar grating technology created with multiple quantum well (MWQ) devices [(69)]. As the ribbons move downward about λ/8, the energy in the +1st modes are clearly defined. As the grat-ings move closer to the λ/4 point, the power is shifted from the 0th mode into the +1st modes, until there is a complete switch. As the ribbons move past the λ/4 point, optical power shifts back into the 0th mode.

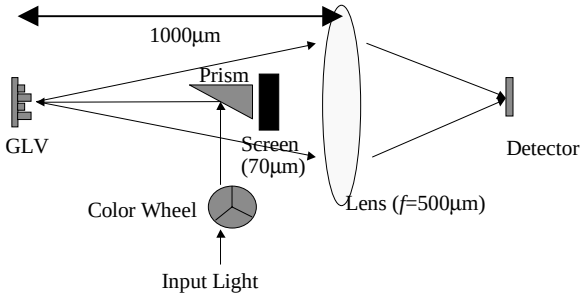

Figure 55 End-to-end GLV Display Link

5.4.2.4 System-level Simulation In the next simulation, we present a full system-level example as we expand the system to show a complete end-to-end link used in a configuration of a color projection system. The system is shown in Figure 55. In this system, we model light, passing through a color wheel, striking a prism, reflecting off the GLV device, past a screen, focused by a lens, and striking a detector [(69)]. In this system, when the GLV ribbons are all up, the screen blocks the light's 0th mode and the pixel is not displayed. When the alternating ribbons are pulled down, the lens focuses the light found in the +1st modes and converges them to the center of the system, displaying the pixel. Using a spinning color wheel to change the wavelength of the incident light, a frame-sequential GLV projection system uses red (680 nm), green (530 nm), and blue (470 nm) light on the same grating [(69)]. Since the same grating is used for all wavelengths of light, the grating movement is tuned for the middle frequency: 130 nm ($\lambda_{green}/4$). During this simulation, we use a hybrid approach for the optical modeling. For the propagation through the color wheel and the prism, we use Gaussian propagation. Since propagating through these components does not diffract the beam, this Gaussian technique is not only efficient, but valid. However, as soon as the light propagates past the prism component, we switch the optical propagation technique to our full scalar method to accurately model the diffraction off of the GLV device. The

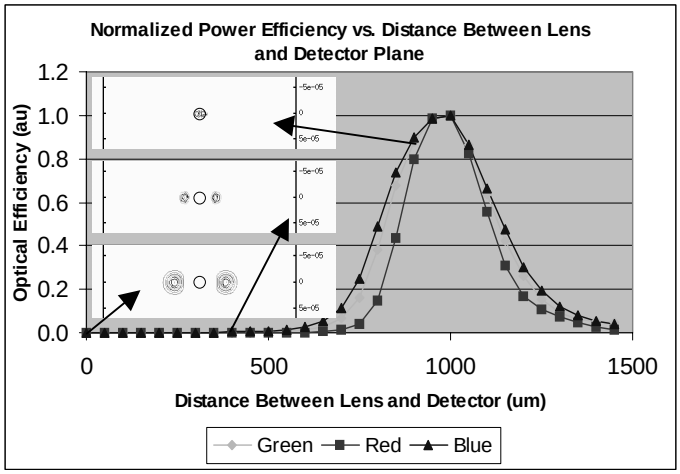

Figure 56 Wavelength Power vs. Distance Propagated

remainder of the simulation is propagated with the scalar technique.

We analyze the system by looking at the amount of optical power that is being received on a centered circular detector (radius 10μm) for the different wavelengths of light, since we are using the same GLV that is tuned for the green wavelength for all wavelengths. A sweep of the distance between the focusing lens and the detector plane is simulated for 0 to 1500 μm, when the GLV ribbons are pulled down. The graph in Figure 56 shows the normalized power received on the circular detector for each wavelength along with selected intensity contours of the green wavefront as the beam propagates past the lens. For clarity, the detector's size and position is added onto the intensity contours. For distances under 600 μm, the light remains in its two positive and negative 1st modes, as the convergence of the beams has not occurred, resulting in zero power being received on the center detector. As expected, each of the wavelengths focuses at a different rate, as shown by each the wavelength's specific curve in Figure 56. However, it is seen that all wavelengths focus and achieve detected maximum power at a distance past the lens of 1000 μm, or twice the lens' focal length. At this point, all three colors project on top of each other, creating a color pixel in the focal plane. With additional optics, this focal plane can be projected to a screen

outside the projector. This simulation has shown that the grating, although tuned for the green wavelength, can be used for all three wavelengths.

5.4.2.5 Electro-Static Ribbon Movement and Bending We now simulate the GLV using the mechanical modeling support found in Chatoyant. Again, we only examine one optical pixel. In these simulations, each ribbon now has a length of 60 μm, a width of 5 μm, and a thickness of 1.5 μm, for a total GLV pixel size of 60x20 μm. The ribbons are made of silicon nitrite (density 3950 Kgm^3, Young's modulus $290x10^9$ Nm^3), and coated with aluminum for smoothness and reflectivity. In these simulations, we assume there is no gap between the ribbons.

The model of the GLV is two fold: an electro-mechanical model simulating the movement of the ribbons towards the substrate, and the optical model, simulating the reflection of the optical wavefront off of the ribbons. Each ribbon is modeled as a thin cantilever beam anchored on each end. The beam is modeled in PWL segments, and is electro-statically attracted to the silicon substrate, which is covered with 500 nm of oxide. The air gap between the ribbons and the substrate is 0.65 μm. This electro-static model is connected to the optical GLV model through a "wire" containing the displacement of each node that comprise the model of the ribbon. A linear interpolation between the nodes is required for the optical mesh points that do not fall on the ribbon's nodes. The effect of the ribbon movement is optically modeled as a phase grating, as described earlier in the section.

In the first simulation, the standard operation of the GLV is verified, as performed before. Again ideal alternating flat, non-anchored ribbons move toward the substrate, however this time, the ribbons are longer, 60 μm. We simulate the GLV in both cases, that is, when all the ribbons are on the same plane and when the alternating ribbons are moved downward a distance of 130

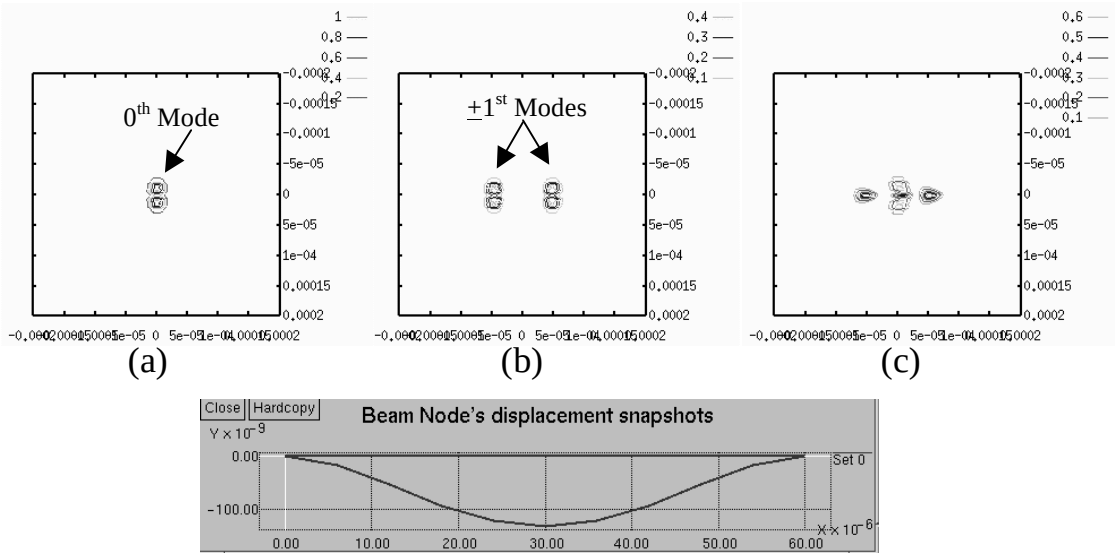

Figure 57 GLV Operation (a) Ribbons all up (b) Ideal Ribbon Displacement (c) Curved Ribbon Displacement

nm, or λ/4. A optical window of 400x400 μm is used, with an optical meshing equal to 256x256. Intensity contours of the optical waveform at the observation plane are presented in Figure 57, for when the ribbons are all aligned, (a), and when alternating ribbons are pulled down, (b). As expected, the output optical waveform's height and widths are not equal. This is due to the total size of the GLV pixel being 60x20 μm. Notice that the optical waveform appears to be in two lobes. This is a near-field optical effect of light propagating through a square aperture and demonstrates that in this system, light propagating 1000 μm is not in the far-field.

However, in real systems, the ribbon ends are anchored, the alternating ribbons are not flat as they are electro-statically attracted to the substrate. The example is now re-simulated with realistic anchored ribbons, which bend as the ribbons are electro-statically attracted to the substrate, as can be seen in the intensity contour of Figure 57(c). The shape of the curved beam is seen below the intensity contours in the Figure 57. Since the beam is curved from the anchors, a square well diffraction pattern is no longer achieved, and the optical intensity contour appears to be a mix of

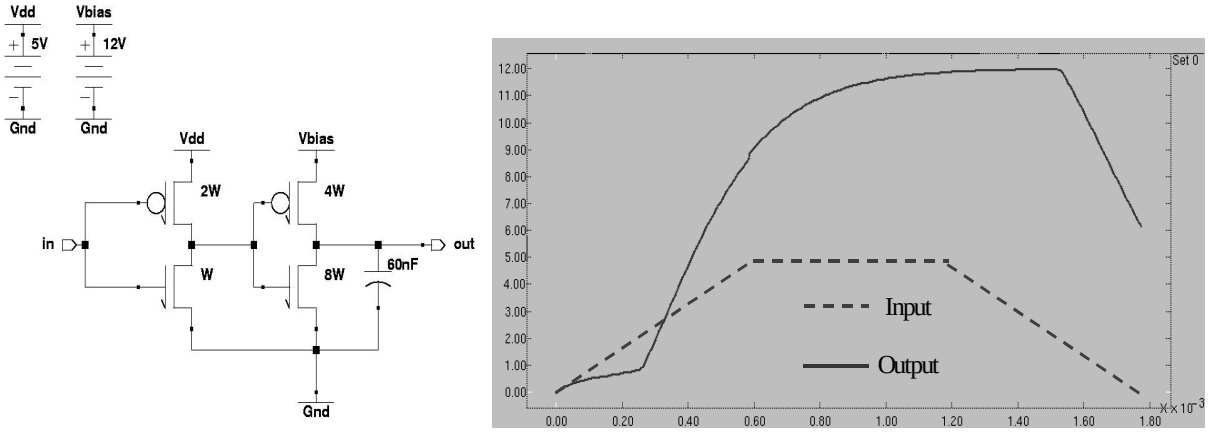

Figure 58 2-Stage CMOS Driver used as the GLV Input and Electrical Response to Ramped Input

the ideal cases seen in (a) and (b). The light reflecting from the center of the ribbon, which is pulled down approximately λ/4 (130 nm), creates the $\pm 1^{st}$ modes. These modes are now circular, since approximately a 20x20 μm square well is effectively created in the center of the GLV device. The remainder of the light reflecting off the ribbons reflects straight off the GLV and creates the light found in the 0^{th} mode.

We now simulate the dynamic nature of the GLV system. The input signal to the system is conditioned by a 2-stage CMOS amplifier seen in Figure 58. The input voltage is ramped between 0 and 5 volts with a switching time of 600 μsec, resulting in the output voltage applied between the ribbons and the substrate being ramped between 0 and 12 volts. Since the ribbon ends are anchored, the alternating ribbons are not flat as they are electro-statically attracted to the substrate. In the simulations, the ribbon is represented by 10 equal sized segments, totaling 11 nodes. Simulation output data show the shape of the curved beams as the voltage ramped between 0 and 12 volts. In the first graph of Figure 59, individual node deflection versus applied voltage is shown. The node displacement is symmetric around the center of the beam, therefore,

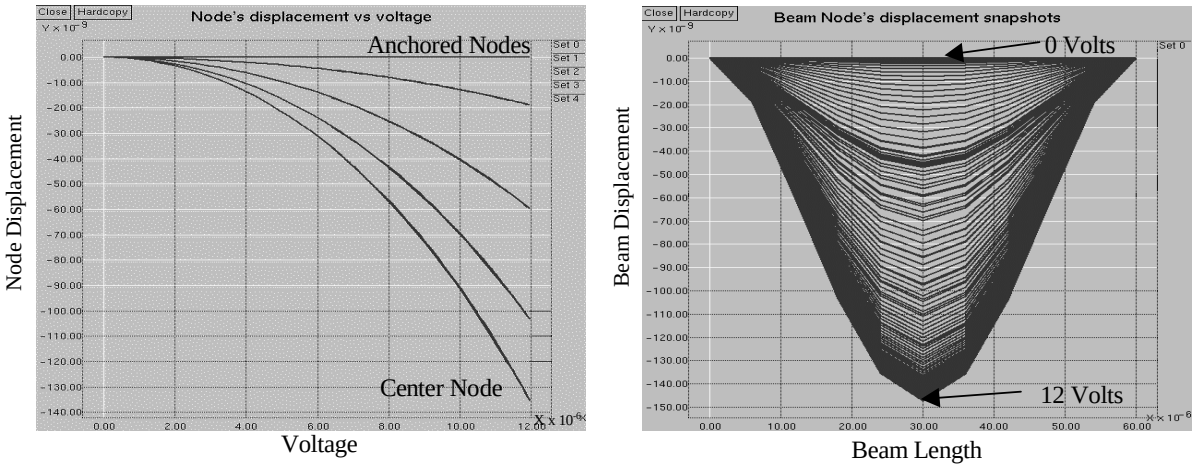

Figure 59 Beam Displacement and Node Displacement vs. Voltage

only nodes on half of the beam are shown. The second graph presents the bending of the entire beam versus input applied voltage. Note that in both graphs, the y-axis is in nanometers and the x-axis is in microns.

Figure 60 presents three graphs presenting multi-domain simulation of the system. The first graph shows the displacement of the center ribbon node and the input voltage with respect to time. As expected, the driver and response of the ribbon movement causes the center node to lag behind the electrical input due to the capacitive load and frequency response of the ribbons.

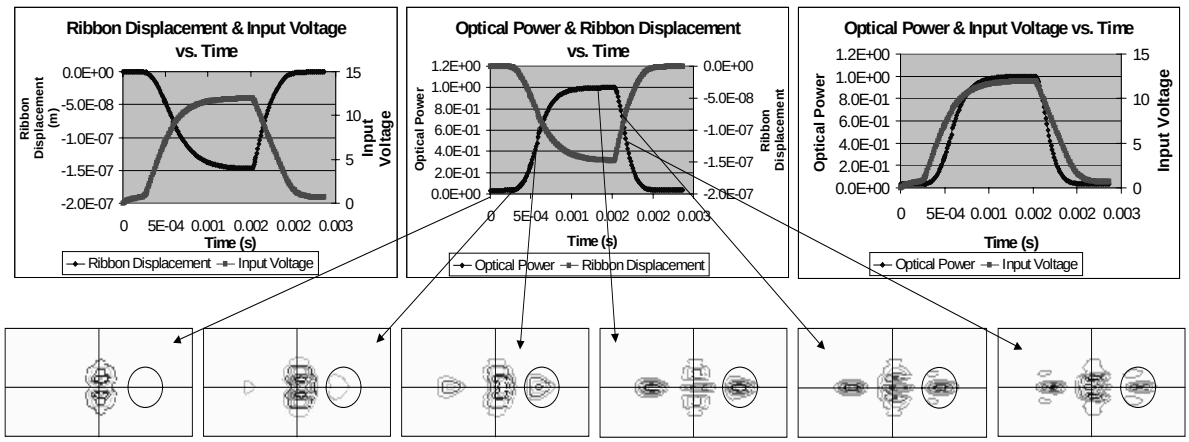

Figure 60 GLV Simulation Graphs and Intensity Contours

From this result, we present the second graph in Figure 60, in which we show the ribbon movement of the center node affecting the normalized optical power captured on a circular detector (radius=10 μm) placed at the location of the positive 1st diffractive mode. As the ribbons are attracted to the substrate, more optical power is diffracted into the non-zero modes. As the center of the ribbons reach the λ/4 point (130 nm), the diffractive power peaks in the +1st mode. Beneath this graph are intensity contours of selected wavefronts during the transient simulation, along with markings of the center of the 0^{th} mode and circular detector position. As can be seen, the diffractive optical output is not ideal, since the beams are curved from the anchors and a complete square well diffraction pattern is not achieved, as previously seen in Figure 57. From these wavefronts, interesting diffractive effects can be noted. As expected, when there is little voltage applied, all the light is in the 0^{th} mode. As the ribbons move downward about λ/8 (65 nm), the energy in the $\pm 1^{st}$ modes is clearly defined. As the gratings move closer to the λ/4 point, more power is shifted from the 0^{th} mode into the $\pm 1^{st}$ modes. As the ribbons start to return to their original position, the optical power shifts back into the 0^{th} mode.

In the third graph of Figure 60, we show the applied voltage and the normalized encircled power verses time. We show in this graph that the switching of power from the 0^{th} diffractive mode to the 1^{st} mode occurs at around 12 volts applied between the ribbon and the substrate. In summary, we have been able to simulate and analyze a complete optical MEM system where a dynamic electrical input modulates a mechanical device, diffracting optical power in a single simulation.

6.0 SUMMARY, CONCLUSIONS, AND FUTURE WORK

6.1 Summary

In this thesis, we have determined an appropriate optical propagation technique suitable for system-level optical micro-system simulation. The Rayleigh-Sommerfeld formulation was chosen as the optical propagation modeling technique by satisfying the requirements of a system-level CAD tool and supporting accurate modeling at small propagation distances and through small component sizes. This technique is valid as long as both the propagation distance and the aperture size are greater than the wavelength of the propagating light. Using a brute force direct integration technique, the Rayleigh-Sommerfeld formulation has a computation order of $O(N^4)$. In this thesis, we have shown how this computational order can be decreased to $O(N^2 \log N)$ using the angular spectrum method, which uses the fast Fourier transform to decompose the complex optical wavefront into plane waves, propagating from the aperture to the observation plane. Each plane wave has a different magnitude or weight, based on its angular frequency components.

In continuous theory, the angular spectrum approach is an exact solution to the Rayleigh-Sommerfeld technique. However, when solving for the Fourier transform using a digital computer, errors can arise. The most common errors are aliasing and truncation, and as a general rule, these errors can be greatly reduced, if not eliminated, by increasing the number of mesh points used in discretizing the complex optical wavefront, or by “padding” the wavefront with zeros. Throughout the discussion of the errors bounds in using the angular spectrum method, we presented several examples, and showed how to reduce the errors. We also presented techniques on the estimation of the errors that do occur in the angular spectrum technique.

The angular spectrum technique has been implemented in our mixed-signal, multi-domain CAD tool Chatoyant. In this thesis, we have included simulations and analyses of two typical optical MEM systems. The first was an optical MEM switch, where the results showed the switching speed, and diffractive effects of using a static-electric MEMS switching mirror. We also presented simulations that used the promising grating light valve MEMS component for display applications. We showed system-level results of using this device for a digital display projector, along with a thorough analysis of the light reflecting from curved GLV ribbons.

6.2 Conclusions

From the research in this thesis, we have filled the void in the lack of a system-level modeling tool for optical micro-systems. The key to success was determining the appropriate optical propagation technique that enabled accurate yet efficient simulation of optical micro-systems. With efficient optical propagation techniques, large mixed-signal systems can be simulated in a fraction of the time that previous single-domain simulators took, and give the accurate results that is suitable for optical micro-systems. Using a tool, like the one presented in this thesis, system designers can reduce the cost of designing, prototyping, and testing multi-domain systems.

The major contributions in this thesis have been the following:

- *Determined an optical propagation technique that is valid for the system-level simulation of optical micro-systems.* It has been determined for a system-level optical micro-system CAD tool that the Rayleigh-Sommerfeld formulation is the most appropriate modeling technique for optical propagation. This technique is accurate for optical micro-systems, as its validity is limited by the requirement that the propagation distance and aperture size must be larger than the wavelength of light. Using a brute

force integration technique, the computationally order of this technique is $O(N^4)$. This limits the interactive nature of the CAD tool.

- *Determined a computationally efficient algorithm for the optical propagation method.* With the angular spectrum technique, the Rayleigh-Sommerfeld formulation can be solved exactly by using continuous Fourier transformation theory. Using the Fourier transform reduces the complex wavefront into plane waves propagating from the aperture to the observation plane. The inverse Fourier transform sums all the propagating plane waves and produces the propagated complex optical wavefunction. With the use of a Fast Fourier transform, the Rayleigh-Sommerfeld formulation can be solved efficiently. The computational order of the technique is reduced to $O(N^2 \log N)$, enabling interactive design between the system designer and the CAD tool.

- *Determined the error of using the optical propagation technique and how it can be minimized.* We have shown in implementing the angular spectrum technique that errors exist due to discrete sampling sizes of the functions (i.e., aliasing and truncation) and using a discrete Fourier transform to approximate a continuous Fourier transform. However, we have presented techniques for calculating these errors, along with techniques for reducing the common aliasing and truncation errors. We have showed that to remove aliasing errors in most micro-optical systems, that the spatial domain needs to be sampled by at least $\frac{\lambda}{2}$. We have also present a point-wise error analysis of a Gaussian beam ($|c_k - F_k| \leq \frac{C}{N^2}$), a optical wavefront propagating through an aperture ($|c_k - F_k| \leq \frac{Ck}{N}$), and a general optical wavefront propagating through a optical micro-system ($|c_k - F_k| \leq \frac{C}{N^{p+1}}$). In our simulations, we have normalized our input waveforms, therefore we determined the maximum error bounds by restricting $0 \leq C \leq 1$.

- *Implemented this research into a system-level CAD tool.* We have demonstrated how we implemented our efficient optical propagation into our mixed-signal, multi-domain

CAD tool, Chatoyant. We presented two system-level examples. The first simulation was an optical MEM switch. In this example, the resonance of the cantilever beam caused light to be reflected into the wrong path. This was rectified by slowing the switching speed of the system. The second simulation presented a system-level simulation of a digital display projector using a grating light valve MEMS component. From this, we showed the effect that realistic curved ribbons have on the performance of the system when compared to idealistically flat ribbons.

6.3 Future Work

In this section, we discuss future work and expansions that can be built on from the work presented in this thesis. To present the future work more clearly, we break this section into multiple sub-sections.

6.3.1 Simulation of Large Systems

The expansion of this work starts simply enough with the modeling and simulation of larger, more complex systems. For example, wavelength division multiplexing (WDM) systems are a common technique to achieve high data rates on fiber-based systems. In these types of systems, an optical signal, containing multiple wavelengths, strikes a grating in free-space and separates into the specific wavelengths [70], each propagating with its own complex wavefront. Each different wavelength carries a separate signal. Not only will a diffractive wavelength grating component have to be modeled, a optical model supporting multiple wavelengths will have to be used. If each wavelength could be modeled separately, the angular spectrum solution of the Rayleigh-

Sommerfeld formulation would be valid. However, the support of a multi-wavelength signal would need to modeled by a different technique.

The support for systems with arrays of sources, such is common in micro-optical systems with a VCSEL array input, is being added to our CAD tool. We have two approaches for accomplishing support for optical arrays. The first method models each beam of the array individually, which we can currently support with our angular spectrum technique. A drawback of this method is that the model does not support the interference between the beams as they strike the observation plane. An additional disadvantage is that a separate complex wave will have to propagated for each beam, causing the computation order of the system to increase to $O(BN^2 \log N)$, where B is the number of sources in the array. The second approach uses a computation window that is large enough to fit all the beams of the optical array. Our angular spectrum technique can be used to model this case, as support for the beam interference is inherent to this model. However, this technique has the drawback that the computation window size increases to capture all the beams in the array. Since the angular spectrum method requires even meshing across the computational window, as the computation window size grows, so does that computation time. For the case of VCSEL arrays, typical spot size are less than 10 μm and the beams are spaced on the array by 250 μm. Therefore, to retain the sampling accuracy for each optical beam, the entire computational window needs to be sampled at that rate. This problem could be solved with uneven meshing in the computation window, which is not supported by the angular spectrum method.

6.3.2 Limitations of the Rayleigh-Sommerfeld Technique

Future work is required to determine exactly under what circumstances the Rayleigh-Sommerfeld formulation becomes invalid. Recall the Rayleigh-Sommerfeld technique is limited by the propagation distance and the aperture sizes must be “much larger than” the wavelength of light. There has been some early results determining exactly what propagation distances and component sizes constitute “much larger than” the wavelength of light. Component sizes and propagation lengths that are too small for valid Rayleigh-Sommerfeld propagation through diffractive optical elements (DOE) have been reported in [71]. This research is important to determine where our optical propagation technique will become invalid in free-space systems, and when full vector solutions will be required.

As optical micro-systems continue to shrink and transition into nano-systems, propagation distances and the component sizes become smaller than the wavelength of light. It is our belief that supporting systems on the nano-scale is the future trend that system-level CAD tools, like Chatoyant, will take. Therefore, with the systems shrinking is size towards the nano-scale, the process to find an appropriate optical modeling technique will begin again. Our initial thought is that vector solutions will be required. This is typically computationally intensive, since we are meshing not only the x-y plane, but also the third dimension. However, since the propagation gap is on the scale of nano-meters, the meshing in the third propagation dimension will be less prohibitive as it was for micro-systems.

6.3.3 Continued Error Analysis

In future efforts, we would like accomplish two major additions to strengthen the error bounds presented in this thesis. The first is to better define the constant *C* in our error analysis. With the normalization of the functions and the goal to find the maximum value of the error bound, we have avoided explicitly calculating the value of *C*. To more clearly define *C*, further investigation into the convergence of the Fourier series is required. A second way to strengthen the error bounds is to have a sense of the error that occurs by propagating plane waves from the aperture to the observation plane. This error will be dependant on the distance the plane waves propagate to the observation plane and the angle in which they strike the observation plane.

In other future error analysis efforts, we would like to add a completely automated error reduction and computation within our system-level CAD tool. Currently, the user needs to minimize aliasing and truncation by simulating the system and inspecting both the spatial and the frequency domains. We would like to include in our error analysis algorithm an automated aliasing check, implemented by comparing the ends of the function in the frequency domain to ensure an essentially bandlimited function. Also, the algorithm would approximate the Nyquist frequency and determine the appropriate sampling size to reduce aliasing. From these determinations in the frequency domain, corresponding corrections in the window size and sampling points can be implemented, and the system would be re-simulated, checking again for aliasing. An automatic truncation test could be implemented by checking the ends of the function as it is returned to the spatial domain by the inverse Fourier transform. If the ends are both approaching zero, within some established tolerance, the signal can be considered untruncated. However, if this is not the case, changes to the original sampling and window sizes would be performed, and the system

would be re-simulated. The only negative aspect to this automatic error checking is that it would add to the simulation time of the system evaluation. However, if efficiency is not a concern, an error algorithm with the proposed suggestions would benefit the user.

6.3.4 Angular Spectrum Support for Curved Surfaces and Surface Roughness

In the thesis, we showed our extensions to the direct integration technique of the Rayleigh-Sommerfeld formulation to support slightly curved surfaces. We would also like to implement this support in the angular spectrum method, since if we currently want to simulate these effects, we have to use the slower direct integration method. We believe that if the aperture surface and the observation surface are both curved with the same radius, the angular spectrum technique, as is, could work. It is currently not clear how the angular spectrum technique would support optical propagation from a planar surface to one that is curved.

To support surface roughness in the angular spectrum technique, one can consider running simulations without a surface roughness analysis, as shown in this thesis, and approximate the power that is lost through surface roughness after the simulation. The power loss would be determined by a complete and detailed study of light scattering off of rough surfaces using full EM vector solutions. From this a statistical value of the amount of optical power that is lost with a specific surface roughness could be calculated [72]. Therefore, probability distributions for the amount of power lost due to scattering are pre-calculated, and added at the end of the simulation. This allows a typical simulation to proceed, for example, with an ideal flat mirror, and at the end of the simulation, the insertion loss analysis uses the pre-determined surface roughness loss value. However, while the technique would work well for simple calculations of insertion loss, it would

not be good for calculations of crosstalk or back scattering. For those analyses, propagating a complex wavefront of the scattered light thought the system is necessary.

6.3.5 Verification

One of the greatest challenges of the work presented here is experimentally validating our results and calculating the error margin throughout the system-level simulation. As is the case with many new technologies, experimental results for optical micro-systems are difficult to obtain. For example, there are no established “benchmarks” for optical MEM switches. There are two factors limiting the amount of experimental results. The first is that results from system level fabrication and testing is not overly abundant, as the cost and time to accurately design, fabricate, and test is very high. This illustrates the motives behind creating a system-level modeling tool such as Chatoyant. The second factor is that if the system is fabricated and tested, commonly in industry, much of the information is not available to the general public due to the company’s desire to market the product and not share their trade-secrets with possible competitors. Verifying our models is an important part of the CAD design process and where we have the least information.

Therefore, our remaining future work is to verify this work though experimental data. Data could be obtained from different sources. We could design and fabricate some simple optical MEM devices, and characterize light reflecting and diffracting from these components. We are also part of a DARPA consortium [73], in which we hope to get experimental data from military optical micro-system applications that we can compare with our simulations.

6.3.6 Future Work Summary

The future of optical micro-systems is bright. More universities and companies are designing mixed-signal, multi-domain micro-systems to perform a variety of applications. The need for a CAD tool to support system-level simulation is a must for these optical micro-systems to advance and grow as quickly as integrated circuits did in the previous 30 years. As the constant desire to make systems faster, cheaper, and smaller drive the industry, CAD tools are required to adapt to new technologies. A concern for an optical modeler is that as systems continue to shrink to the nano-scale, new optical models in terms of propagation and components will need to be supported. In that case, the search for an appropriate optical modeling technique to support these systems will begin again.

BIBLIOGRAPHY

BIBLIOGRAPHY

1. Zaman, M.H., Bart, S.F., Gilbert, J.R., Swart, N.R., Mariappan M., "An Environment for Design and Modeling of Electro-Mechanical Micro-Systems," *Journal of Modeling and Simulation of Microsystems*, Vol. 1, No. 1, 1999, pp. 65-76.

2. MEMSCAP, http://www.memscap.com/

3. Kurzweg, T.P., Levitan, S.P., Martinez, J.A., Marchand, P.J., Chiarulli, D.M., "Diffractive Optical Propagation Techniques for a Mixed-Signal CAD Tool," *Optics in Computing (OC2000)*, Quebec City, CA, June 18-23, 2000.

4. Lin, L.Y., Goldstein, E.L., Tkach, R.W., "Free-Space Micromachined Optical Switches with Submillisecond Switching Time for Large-Scale Optical Crossconnects," *IEEE Phot. Technology Letters*, Vol. 10, No.4, April 1998, pp. 525-527.

5. Wu, M.C., "Micromachining for optical and Optoelectronic Systems," *Proceedings of the IEEE*, Vol. 85, No. 11, (November 1997), pp. 1833-1856.

6. Optical Micro-Machines Inc., http://www.omminc.com/

7. Akiyama, T., Collard, D., Fujita, H., "Scratch drive actuator with mechanical links for self-assembly of three-dimensional MEMS," *Journal of Microelectromechanical Systems*, Vol. 6, No. 1., March 1997, pp. 10-17.

8. Bloom, D.M., "The Grating Light Valve: Revolutionizing Display Technology," Photonics West, Projection Displays III, 1997.

9. Romanowicz, B., Methodology for the Modeling and Simulation of Microsystems, (Kluwer Academic Publishers, 1998).

10. Hornbeck, L.J., "Digital Light Processing™: A New MEMS-Based Display Technology," http://www.ti.com/

11. Research Software, Inc., http://www.rsoftinc.com/

12. Optiwave Corp., http://www.optiwave.com/

13. Saleh, B.E.A., Teich, M.C., Fundamentals of Photonics, (New York: Wiley-Interscience,

1991).

14. Optical Research Associates, http://www.opticalres.com/

15. Focus Software, Inc., http://www.focus-software.com/

16. Lambda Research Corporation, http://www.lambdares.com/

17. Delen, N. and Hooker, B., "Free-space beam propagation between arbitrarily oriented planes based on full diffraction theory: a fast Fourier transform approach," *Journal Optical Society of America A*, Vol. 15, No. 4, April 1998, pp. 857-867.

18. Levitan, S.P., Kurzweg, T.P., Marchand, P.J., Rempel, M.A., Chiarulli, D.M., Martinez, J.A, Bridgen, J.M., Fan, C., McCormick, F.B., "Chatoyant: a computer-aided design tool for free-space optoelectronic systems," *Applied Optics*, Vol. 37, No. 26, September, 1998, pp. 6078-6092.

19. McCormick, F.B., Tooley, F.A.P., Cloonan, T.J., Sasian, J.M., Hinton, H.S., "Microbeam optical Interconnections Using Mircolens Arrays", *OSA Proceedings on Photonic Switching*, Vol 8., 1991, pp. 90-96.

20. Goodman, J.W., Introduction to Fourier Optics, Second Edition (The McGraw-Hill Companies, Inc., 1996).

21. Louri, A. and Major, M.C., "Generalized methodology for modeling and simulating optical interconnection networks using diffraction analysis," *Applied Optics*, Vol. 34, No. 20, July, 1995, pp. 4052-4064.

22. Born, M., Wolf, E., Principles of Optics, 7th Edition, (Cambridge University Press, 1999).

23. Hecht, E., Optics, Second Edition (Addison-Wesley Publishing Company, 1987).

24. Huang, W.P., Xu, C.L., Chu, S.T., Chaudhuri, S.K., "A Vector Beam Propagation Method for Guided-Wave Optics," *IEEE Photonics Technology Letters*, Vol. 3, No. 10, October 1991, pp. 910-913.

25. Scarmozzino, R., Osgood, R.M.,Jr., "Comparison of finite-difference and Fourier-transform solutions of the parabolic wave equation with emphasis on integrated-optics applications," *Journal Optical Society of America A*, Vol. 8, No. 5, May 1991, pp. 725-731.

26. Mirotznik M., Prather D.W., et. al, "Three-Dimensional Analysis of Subwavelength Diffractive Optical Elements with the Finite-Difference Time-Domain Method," Applied Optics, Vol. 39, No. 17, June 2000, pp. 2871-2880.

27. Tzolov, V., Feng, D., Tanev, S., Jakubczyk, Z.J., "Modeling tools for integrated and fiber optical devices", *Integrated Optics Devices III, Photonics West '99*, Jan. 23-29, 1999, San

Jose, CA.

28. For clarification in this text, we mean the Rayleigh-Sommerfeld formulation of the first kind [20] when we say Rayleigh-Sommerfeld.

29. Breault Research Organization, Inc., http://www.breault.com/

30. Fan, J., Catanzaro, B., Kiamilev, F., Esener, S.C., Lee, S.H., "Architecture of an Integrated Computer-Aided Design System for Optoelectronics," *Optical Engineering*, Vol. 33, No. 5, (May 1994), pp.1571-1580.

31. Vdovin, G., LightPipes Manual, Electronic Instrumentations Laboratory of TU Delft, 1993-1996.

32. Morikuni, J.J, Kang, S., Computer-Aided Design of Optoelectronic Integrated Circuits and Systems, (Prentice Hall), 1997.

33. Whitlock, B.K., "iFrost: A CAD Tool for Modeling and Simulation of Optical Interconnects" (unpublished Ph.D. Dissertation, School of Engineering, University of Illinois at Urbana-Champaign, 1996).

34. Deng, J., Shur, M.S., Fjeldly, Baier, S., Ytterdal, T., "SPICE Modeling for Mixed Electronic/Photonic VLSI," *VLSI Phontonics PI Review Meeting DARPA/MTO*, Santa Fe, NM, February 17-18, 2000.

35. Morikuni, J.J., Mena, P.V., Harton, A.V., Wyatt, K.W., "The Mixed-Technology Modeling and Simulation of Opto-Electronic Microsystems," *Journal of Modeling and Simulation of Microsystems*, Vol. 1, No. 1, 1999, pp. 9-18.

36. Xu, J.M., Ellis, D.S., "OE^{UT}-Spice: A CAD tool for design and simulation of OEIC", *SPIE Vol. 3006*, 1997.

37. Jacquemod, G., Vuorinen, K., Gaffiot, F., Spisser, A., Leclercq, J-L., Rojo-Romeo, P., Viktorovitch, "MOEMS Modeling for Opto-Electro-Mechanical Co-Simulation," *Journal of Modeling and Simulation of Microsystems*, Vol. 1, No. 1, 1999, pp. 39-48.

38. Kazi, K., Donkor, E., "VHDL as a modeling and simulation platform for optical communication systems and devices," *Optical Engineering*, Vol. 34, No. 5, May 1995, pp. 1450-1455.

39. Kurzweg, T.P. and Morris, A.S., "Macro-Modeling of Systems Including Free-Space Optical MEMS," *Third International Conference on Modeling and Simulation of Microsystems, Semiconductors, Sensors and Actuators (MSM00)*, San Diego, CA, March 27-29, 2000.

40. Kowarz, M.W., "Diffraction Effects in the Near Field," Ph.D. Thesis, University of Roch-

ester, Institute of Optics, 1995.

41. Tommasi, T., Bianco, B., “Frequency Analysis of Light Diffraction Between Rotated Planes,” Optics Letters, Vol. 17, No. 8, April 1992, pp.556-558.

42. Numerical Recipes in C: The Art of Scientific Computing, (Cambridge University Press, 1988-1992).

43. Prather, D.W., University of Delaware, private communication.

44. Goodman, J.W., Introduction to Fourier Optics, Second Edition (The McGraw-Hill Companies, Inc., 1996), Chapter 4, p.86, Figure 4.15.

45. Briggs, W.L. and Henson, V.E., The DFT: An Owner’s Manual for the Discrete Fourier Transform, (Society for Industrial and Applied Mathematics, Philadelphia, 1995).

46. Shannon, C., “Communication in the Presence of Noise,” Proceedings IRE, 37:10, 1949.

47. Weaver, H.J., Applications of Discrete and Continuous Fourier Analysis, (John Wiley & Sons, Inc., 1983).

48. Wilhelm, R., “Comparing Geometrical and Wave Optical Algorithms of a Novel Propagation Code Applied to the VLTI,” Wave-Optical System Engineering, Prod. SPIE, Vol. 4436, 2001.

49. http://mathworld.wolfram.com/FourierTransformGaussian.html

50. Walker, J.S., Fourier Analysis, (Oxford University Press, Inc., 1988).

51. Carslaw, H.S., Introduction to the Theory of Fourier’s Series and Integrals, Third Editions, (Dover Publications, Inc., 1930).

52. http://www.wikipedia.com/wiki/supremum

53. Kurzweg, T.P., Levitan, S.P., Marchand, P.J., Martinez, J.A., Prough, K.R., Chiarulli, D.M., “CAD for Optical MEMS,” *Proceedings of the 1999 Design Automation Conference*, New Orleans, LA, June 20-25, 1999, pp.879-884.

54. Kurzweg, T.P., Martinez, J.A., Levitan, S.P., Marchand, P.J., Shomsky, M.T., Chiarulli, D.M., “Modeling Optical MEM Systems,” *Journal of Modeling and Simulation of Micro-Systems*, Vol. 2, No. 1, pp. 21-34, 2001.

55. Levitan, S.P., Marchand, P.J., Kurzweg, T.P., Rempel, M.A., Chiarulli, D.M., Fan C., McCormick, F.B., “Computer-Aided Design of Free-Space Opto-Electronic Systems,” *Proceedings of the 1997 Design Automation Conference*, Anaheim, CA, June 1997, Best Paper Award, pp. 768-773.

56. Buck, J., Ha, S., Lee, E.A., Messerschmitt, D., “Ptolemy: a framework for simulating and prototyping heterogeneous systems,” *Int. J. Computer Simulation*, Vol. 4, 1994, pp. 155-182.

57. Martinez, J.A., Kurzweg, T.P., Levitan, S.P., Marchand, P.J., Chiarulli, D.M., “Mixed-Technology System-Level Simulation”, Analog Integrated Circuits and Signal Processing (ALOG), Vol. 29, pp. 127-149, October/November 2001.

58. Kurzweg, T.P., Levitan, S.P., Martinez, J.A., Kahrs, M., Chiarulli, D.M., “A Fast Optical Propagation Technique for Modeling Micro-Optical Systems,” *Proceedings of the 2002 Design Automation Conference*, New Orleans, LA, June 10-14, 2002.

59. Abramowitz, M. and Stegun, I. A., editors, Handbook of Mathematical Functions with Formulas, Graphs, and Mathematical Tables, (Dover Publications, Inc., New York, 1972).

60. Kurzweg, T.P., Martinez, J.A., Levitan, S.P., Marchand, P.J., Chiarulli, D.M., “Dynamic Simulation of Optical MEM Switches,” *Design, Test, Integration, and Packaging of MEMS/ MOEMS (DTIP2001)*, Cote d'Azur, France, April 25-27, 2001.

61. Martinez, J.A., “Piecewise Linear Simulation of Optoelectronic Devices with Applications to MEMS”, MS Thesis, University of Pittsburgh, Department of Electrical Engineering, 2000.

62. “‘Seesaw’ Switch is First Practical Micro-Electro-Mechanical Optical Switch,” http://www.bell-labs.com/news/1999/february/23/1.html.

63. Lee, S.S., Motamedi, E., Wu, M.C., “Surface-micromachined free-space fiber optic switches with integrated microactuators for optical fiber communication systems,” in *Proceedings of the 1997 International Conference of Solid-State Sensors and Actuators (TRANSDUCERS 97)*, 1997, paper 1A4.07P.

64. Marxer, C., de Rooij, N.F., “Micro-Opto-Mechanical 2x2 Switch for Single-Model Fibers Based on Plasma-Etched Silicon Mirror and Electrostatic Actuation,” *Journal of Lightwave Technology*, Vol. 17, No. 1, January 1999, pp. 2-6.

65. Chen, R.T., Nguyen, H., Wu, M.C., “A High-Speed Low-Voltage Stress-Induced Micromachined 2x2 Optical Switch,” IEEE Photonics Technology Letters, Vol.11, No. 11, Nov. 1999, pp.1396-1398.

66. ANSYS Inc., http://www.ansys.com

67. Solgaard, O., “Integrated Semiconductor Light Modulators for Fiber-Optic and Display Applications,” Ph.D. Thesis, Stanford University, 1992.

68. Amm, D.T., Corrigan, R.W., “Optical Performance of the Grating Light Valve Technology,” Photonics West-Electronic Imaging, Projection Displays V, 1999.

69. Ahearn, J.S., et. al, “Multiple Quantum Well (MQW) Spatial Light Modulators (SLM) for Optical Data Processing and Beam Steering,” BAE Systems, Advance Copy.

70. Ford, J.E., Aksyuk, V.A., Bishop, D.J., Walker, J.A., “Wavelength Add-Drop Switching Using Tilting Micromirrrors,” *Journal of Lightwave Technology*, Vol. 17, No. 5, May 1999, pp. 904-911.

71. Mellin, S.D., Nordin, G.P., “Limits of Scalar Diffraction Theory and an Iterative Angular Spectrum Algorithm for Finite Aperture Diffractive Optical Element Design,” *Optics Express*, Vol. 8, No. 13, June 18, 2001, pp.705-722.

72. Marxer, C., Gretillat, M.-A., de Rooij, N.F., Battig, R., Anthamatten, O., Valk, B., Vogel, P., “Vertical Mirrors Fabricated by Reactive Ion Etching for Fiber Optical Switching Applications,” *MEMS 1997*, 1997, pp. 49-54.

73. DARPA grant AFOSR F499620-01-1-0536.